uOttawa

L'Université canadienne
Canada's university

FACULTÉ DES ÉTUDES SUPÉRIEURES ET POSTOCTORALES

uOttawa

L'Université canadienne
Canada's university

FACULTY OF GRADUATE AND POSDOCTORAL STUDIES

Fabien Ravet

AUTEUR DE LA THÈSE / AUTHOR OF THESIS

Ph.D. (Physics)

GRADE / DEGREE

Department of Physics

FACULTÉ, ÉCOLE, DÉPARTEMENT / FACULTY, SCHOOL, DEPARTMENT

Performance of the Distributed Brillouin Sensor: Benefits and Penalties Due to Pump Depletion

TITRE DE LA THÈSE / TITLE OF THESIS

Xiaoyi Bao

DIRECTEUR (DIRECTRICE) DE LA THÈSE / THESIS SUPERVISOR

Liang Chen

CO-DIRECTEUR (CO-DIRECTRICE) DE LA THÈSE / THESIS CO-SUPERVISOR

EXAMINATEURS (EXAMINATRICES) DE LA THÈSE / THESIS EXAMINERS

S. Fafard

T. Xu

É. Fortin

D. Thomson

Gary W. Slater

Le Doyen de la Faculté des études supérieures et postdoctorales / Dean of the Faculty of Graduate and Postdoctoral Studies

Performance of the Distributed Brillouin Sensor: Benefits and Penalties Due to Pump Depletion

by
Fabien Ravet

Thesis submitted to
The Faculty of Graduate and Postdoctoral Studies
In partial fulfillment of the requirements for the Degree of
Doctor of Philosophy
Ottawa-Carleton Institute for Physics
University of Ottawa

Your file Votre référence
ISBN: 978-0-494-34143-8
Our file Notre référence
ISBN: 978-0-494-34143-8

To Ngalula Mabudi, whose love, dedication and support helped me to turn this dream into reality.

Abstract

Disaster prevention in civil infrastructures requires the use of techniques that allow temperature and strain measurements in real time over lengths of a few meters to tens of kilometres. The distributed Brillouin sensor (DBS) technique has the advantage to combine all these characteristics.

The sensing mechanism of the DBS involves the interaction of two counter-propagating lightwaves, the Stokes and the pump, in an optical fibre. Spatial information is obtained through time domain analysis. The sensing data are recorded from the measurement of the pump depletion. We explore the benefits and the drawbacks of this approach and show that there is a power range for which the sensing performances are optima. To achieve that goal, Brillouin fibre generator (BFG) and amplifier (BFA) were studied leading to the derivation of a threshold definition for the BFA, which is the configuration of the DBS. Within that context, numerical and analytical models describing the stimulated Brillouin scattering (SBS) interaction are introduced and validated experimentally.

Even if pump depletion is carefully controlled, the Brillouin spectrum shape, and hence the sensor performance, still depend on the sensing parameters such as power, pulse and fibre characteristics. We use a signal processing method grounded in the physics of Brillouin scattering. An analytical approximation, valid for the optimum sensing region, reconstructs the Brillouin spectrum distribution from input sensing parameters and measured data. These data are obtained with a spectrum analysis methodology, based on three original tools: the Rayleigh equivalent criterion, the length-stress diagram, and the spectrum form factors. This methodology has been successfully used on experimental spectra.

The DBS and the signal processing approach were then used to monitor the structural changes in steel pipes and in a composite column, all subjected to heavy loads. The DBS measured the strain distribution of those structures while they were stressed. The DBS provided detailed information on the structure's health at local and global level, associated with deformations, cracks and buckling. This work demonstrates that the DBS is capable of extracting critical information useful to engineers: engineer's experience and judgement in conjunction with appropriate data processing methods make possible to anticipate structural failures.

Keywords: Brillouin scattering, optical fibres, SBS threshold, Brillouin generator, Brillouin amplifier, gain saturation, pump depletion, sensor performance, spatial resolution, frequency resolution, signal processing, structural health monitoring, distributed Brillouin sensor, strain measurement.

Résumé

La prévention de désastres dans les infrastructures de génie civil et de transmission d'énergie nécessite l'utilisation de techniques qui permettent de mesurer la température et les contraintes de manière distribuée, en temps réel, sur des longueurs variant de quelques mètres à plusieurs dizaines de kilomètres. Le capteur distribué Brillouin (CDB) possède la caractéristique de combiner tous ces avantages.

Le mécanisme de la mesure se base sur l'interaction de deux ondes optiques, l'onde de Stokes et l'onde de pompe, se propageant en directions opposées. L'information spatiale est obtenue par une technique d'analyse dans le domaine temporel. Température ou/et contrainte sont extraites de la mesure de l'atténuation du signal de pompe en fonction du temps. La présente recherche explore les avantages et les inconvénients de cette technique et montre qu'il existe une gamme de puissance pour laquelle le mode d'opération du capteur est optimum. Afin de mener à bien cette tâche, le miroir et l'amplificateur Brillouin à fibres sont étudiés menant à la dérivation d'une définition du seuil Brillouin applicable à l'amplificateur à fibres, configuration de notre capteur. Dans ce cadre, des modèles numériques et analytiques décrivant la diffusion Brillouin stimulée sont introduits et validés expérimentalement.

Même si l'atténuation de la pompe est contrôlée, la forme du spectre Brillouin, et donc la performance du capteur, dépend toujours de paramètres de mesure tels que la puissance, les caractéristiques de l'impulsion, le type de fibre ainsi que sa longueur. Pour tenir compte de ces influences, nous proposons d'utiliser une méthode de traitement des données enracinée dans la physique de la diffusion Brillouin. Une approximation analytique, valide pour le mode d'opération optimum du capteur, permet de reconstruire la distribution du spectre Brillouin à partir des paramètres de la mesure et du résultat de la déconvolution des données. Cette est renforcée par une méthode d'analyse de la forme des spectres basée sur trois outils originaux: le critère de Rayleigh équivalent, le diagramme longueur-contrainte et les facteurs de forme des spectres Brillouin. Cette méthode a été utilisée avec succès sur des spectres expérimentaux.

Le CDB et notre technique de traitement du signal ont été utilisés pour surveiller les changements de l'état de structure d'un pipeline en acier et d'une colonne composite soumis tous deux à des charges élevées. Le CDB a mesuré le profil des contraintes le long de la colonne et du pipeline pour différentes conditions expérimentales. Ensuite, les données mesurées avec le CDB ont permis d'évaluer l'état de la structure a un niveau tant local que global, état caractérisé par l'apparition de déformations, de fissures et de flambement avant qu'ils ne soient visibles. Cette recherche montre que le CDB est capable de fournir des informations critiques pour les ingénieurs: l'utilisation de méthodes de traitement des données appropriées éclairées par l'expérience et le jugement de l'ingénieur rend possible l'anticipation de défaillances structurelles.

Mots Clés: diffusion Brillouin, fibres optiques, seuil Brillouin, miroir Brillouin, amplificateur Brillouin, saturation du gain, atténuation de la pompe, performance du capteur, résolution spatiale, résolution fréquentielle, traitement du signal, surveillance de l'état des structures, capteur Brillouin distribué, mesure de contrainte.

Acknowledgement

When I moved to Canada, seven years ago, I really did not expect to return back to the academic world. On the contrary, I buried any hope of being immerged in education and fundamental research. Life as a journey always reserves us all kind of surprises that sometimes lead us in the path of thoughtful and interesting people. Among those, I will never forget Dr Xiaoyi Bao who invited me, four years ago, to join her team as a graduate student. First and foremost, I am grateful because she offered me a chance to materialise an old and forgotten dream. I am also grateful for the constant interest she showed in my progress and for the guidance she gave me. I will never forget.

Working four years towards this degree made me appreciate the help of Dr Liang Chen. His rigorous mind was a real support in keeping me on track and in finding the weaknesses of some of my theoretical and numerical developments.

I also want to mention Dr Lufan Zou, who was my field test partner. We spent interesting moments while trying to implement the distributed Brillouin sensor on real world structures.

I do not want to miss this opportunity to thank all my past and present colleagues from the Fibre Optics Group for the help and the good times: Dr Pingyu Zhu, Yun Li, Ziyi Zhang, Line Bouchard, Suad Mohamed Abuzaniba, Dr Saeed Hadjifaradji, Dr Shahraam Afshar Vahid, Dr Zhongxi Zhang, Dr Qinrong Yu, Dr Wenhai Li, Dr Chunshu Zhang, Dr Shiquan Yang, Dr John Cameron, Dr Vladimir Kalosha, Dr Evgueni Ponomarev, Jeff Snoddy, Alexandre Yale, Ou Chen, Yidun Wan, Graham Ferrier, David Waddy, Robert Walker, Ryan Bolen... I would like to apologise for the persons I missed...

Those acknowledgements would not be complete if I do not thank our industry and fellow civil engineer partners whose collaborations were highly appreciated. Chapter VI of the present thesis would not have been possible without their involvement. I want to thank sincerely Dr Togay Ozbakkaloglu, Dr Murat Saatcioglu, Dr Henk-Aik Khoo, Dr Joe Zhou, Dr Tom Zimmerman, Dr Louis Lamarche and Rong Feng Huang.

I also want to acknowledge the financial support of Natural Science and Engineering Research Council Canada, the Canadian Foundation for Innovation, and Agile All-Photonic Networks. Intelligent Sensing for Innovative Structures Canada, whose funding was of course very appreciated, gave me much more: this network helped me to open my physicist mind to the real world. I want to say that I integrated much of the spirit of the network into my personality.

I am also grateful to the member of the jury, Dr Simon Fafard, Dr Emery Fortin Dr Douglas Thomson and Dr Tong Xu, for the time they took to review my text. Their comments were valuable and helped me to improve the manuscript. I sincerely do appreciate it.

Je ne terminerai pas ces remerciements sans évoquer le Prof. Michel Blondel qui me communiqua son enthousiasme pour les fibres optiques. En le remerciant, je songe aussi à tous mes anciens collègues et amis de la «Polytech» et de Multitel (en devenir). Quelle aventure!

Ses remerciements seraient honteusement incomplets si j'oubliais ma famille dont l'intérêt et le soutien permanent contribuèrent à cet achèvement: mes parents, si présents, qui m'ont toujours encouragé, Géraldine et Hugues, si proches malgré la Mer Océane, Olivia dont la naissance alors que je débutais la rédaction de ma thèse, fut un printemps pour nous tous, Madina et Hubert, petits frères et néanmoins condisciples à l'université d'Ottawa. Comment pourrais-je remercier Ngalula Mabudi, mon épouse, dont la présence, l'amour, la patience, le soutien furent une bénédiction de tous les instants. C'est à cette famille que je dédie cette thèse...

Statement of originality

This work does not contain material which has been accepted for the award of any other degree or diploma in any University or other tertiary institution and, to the best of my knowledge and belief, contains no material previously published or written by another person, except where due reference has been made in the text or in the present section.

My contribution to the field of distributed sensing and Brillouin scattering is twofold and original. It covers practical and fundamental aspects of Brillouin scattering. On the practical side, I have been actively working on the application of the distributed Brillouin sensor to the monitoring of power line, distribution and transmission pipelines, steel beam and as well as concrete columns reinforced with polymer fibres. These implementations include the fibre lay out, the taking of the measurement as well as the data analysis. In the case of the pipeline tests, these various tasks were completed with the help and the involvement of Dr Lufan Zou. The outcomes of those tests are original as they demonstrated that the Brillouin sensor s a unique tool to anticipate structure failures (Ravet 2005b, Ravet 2006, Ravet 2006b, Ravet 2007). To analyse the data, I have developed specific and original signal-processing tools, which are the length-stress diagram, the Rayleigh equivalent criterion, the form factors as well as a spectrum reconstruction technique based on the physics of Brillouin scattering. That rationalised methodology differs from approaches used by my predecessors where blind guess were the basics of signal analysis (Ravet 2005, Ravet 2005a, Ravet 2006, Ravet 2006c). The development of these data analysis tools led me to investigate the fundamentals of Brillouin scattering, which is the fundamental aspect of my work. Within that context, I carried out experimental and theoretical investigations to understand the physics of Brillouin scattering using my own set-ups and numerical algorithms. More specifically, I studied the effect of pump depletion on gain and pulse delay on the performance of the distributed Brillouin sensor, which is an aspect of the sensor field that was never addressed (Ravet 2006a). From these studies, I derived an original expression for the maximum input power that guarantees optimum sensing operation. Such expression is unique, as it was never proposed before while needed to quantify the limit to the power

that can be fed into a BFA type configuration for optimum operation. These various contributions are materialised by the publication of eighteen articles or letters in peer-reviewed journals and the discussion of twenty-one communications in international conferences (please refer to the list in Appendix D).

Thoe achievements would not have been possible without the involvement of my peers or external contributors. That is the reason why credits must be given to:

- Ms Yun Li, a Master degree candidate, who helped me to obtain the experimental data shown in Figure IV.18.
- Dr Qinrong Yu, who provided me with the experimental spectra shown in Figures V.6, V.10, V.18, V.19 and V.20.
- Dr Henk-Aik Khoo who provided me with the electrical strain gauge readings that are presented in section VI.B.
- Dr Tom Zimmerman who provided me with the electrical strain gauge readings that were compared with the distributed Brillouin sensor measurements in section VI.C.
- Dr Togay Ozbakkaloglu who provided me with the electrical strain gauge readings that are presented in section VI.D.

"Knowledge is like a bird in the forest, it is impossible for a single person to catch it"

African oral tradition

"On ne peut pas peindre du blanc sur du blanc, du noir sur du noir. Chacun a besoin de l'autre pour se révéler"

Manu Dibango

Table of Content

List of Figures

List of Tables

List of Abbreviations and Symbols

ABBREVIATIONS

ABSE:	Amplified Brillouin Spontaneous Emission
BFA:	Brillouin Fibre Amplifier
BFG:	Brillouin Fibre Generator
BOFDA:	Brillouin Optical Frequency Domain Analyser
BOSA:	Brillouin Optical Spectrum Analyser
BOTDA:	Brillouin Optical Time Domain Analyser
BOTDR:	Brillouin Optical Time Domain Reflectometer
BPF:	Band Pass Filter
C-FER:	Centre for Frontier Engineering Research
cw:	Continuous Wave
DBS:	Distributed Brillouin Sensor
DCF:	Dispersion Compensating Fibre
ECL:	External Cavity Laser
EDFA:	Erbium Doped Fibre Amplifier
EOM:	Electro-Optic Modulator
ESA:	Electrical Spectrum Analyser
FBG:	Fibre Bragg Grating
FOS:	Fibre Optic Sensor
FP:	Fabry Perot
FRP:	Fibre Reinforced Polymer

FUT:	Fibre Under Test
FWHM:	Full Width at Half Maximum
ISIS:	Intelligent Sensing for Innovative Structures
ITU:	International Telecommunication Union
LEAF:	Large Effective Area Fibre
LG:	Long Gauge
LS:	Length-Stress
LSM:	Laser Side Mode
NTT:	Nippon Telegraph and Telephone
ORC:	Optoelectronic Research Centre
OTDR:	Optical Time Domain Reflectometer
PCF:	Photonics Crystal Fibre
PD:	Photo-Diode
PMA:	Power Meter Approach
PMF:	Polarisation Maintaining Fibre
NCE:	Network of Centre of Excellences
REC:	Rayleigh Equivalent Criterion
RPP:	Relative Peak Power
RSS:	Rayleigh Scattering of the Stokes wave
SBS:	Stimulated Brillouin Scattering
SHM:	Structural Health Monitoring
SI:	Step Index
SOS:	Second Order Stokes wave
SNR:	Signal-to-Noise Ratio

TCPL: TransCanada PipeLine

TLS: Tuneable Laser Source

TP: Transmitted Pump

LATIN SYMBOLS

A: Electric field complex amplitude

A_{eff}: Effective area

c_o: Velocity of light in vacuum

C_ε: Tensile strain coefficient

C_T Temperature coefficient

$\vec{D}$: Displacement vector

$\vec{E}$: Electric field

ER: Extinction Ratio

F_A: Asymmetric factor

F_B: Broadening factor

g: Brillouin gain coefficient

g_B: Centreline Brillouin gain coefficient

G: Intensity coefficient (for Brillouin interaction induced gain and loss)

h: Planck's constant

I: Optical intensity

$\vec{k}$: Optical wavenumber

k_B: Bolzmann's constant

K: Young modulus

L: Fibre length

L_{eff}:	Effective length
n:	Refractive index
N_{pk}:	Number of peaks
N_{ph}:	Number of acoustic phonons
NEP:	Noise-equivalent power
p:	Pressure
p_e:	Electrostrictive pressure
p_{ij}:	Photoelastic tensor coefficients
P:	Optical power
P_{th}:	SBS power threshold
$\vec{q}$:	Acoustic wave number
Q:	Acoustic field complex amplitude
Q_o:	Acoustic field amplitude
R	Correlation coefficient
rms:	Root-mean-square
s:	Entropy
S:	Measured spectrum
SNR_e:	Electrical signal-to-noise ratio
t:	Time
T:	Temperature
v_g:	Group velocity
V:	Voltage
V_A:	Acoustic Velocity
w:	Spatial resolution

z: Position

GREEK SYMBOLS

α: Natural loss of the fibre

α_{comp}: Component loss

χ: Medium susceptibility

χ_{SBS}: Depolarisation factor

δl: Stressed section length

δn: Refractive index variation

Δ: Relative Refractive index difference

Δf: Receiver bandwidth

Δp: Pressure fluctuation

Δs: Entropy fluctuation

$\Delta \varepsilon$: Dielectric constant fluctuation

$\Delta \nu$: Detuning frequency

$\Delta \nu_B$: Natural linewidth of the Brillouin gain coefficient (FWHM of a Lorentzian distribution) as well as spontaneous or small signal gain linewidth

$\Delta \nu_{SBS}$: SBS linewidth (FWHM of the Brillouin specyrum in stimulated regime)

$\Delta \nu_s$: Brillouin frequency difference between stressed and unstressed components

$\Delta \rho$: Density fluctuation

$\Delta \tau$: Pulsewidth

ε: Dielectric constant

ε':	Tensile strain
ε_o:	Vacuum dielectric constant
ϕ:	Optical phase change induced by propagation in an EOM arm
Φ:	Phase change induced by Brillouin frequency
γ:	Relative peak height
γ_e:	Electrostrictive constant
Γ:	Brillouin spectrum linewidth (FWHM)
Γ':	Acoustic wave damping parameter
Γ_B:	Acoustic wave decay rate
Γ_n:	Brillouin spectrum linewidth (FWHM) normalized by the small signal gain linewidth
φ:	Brillouin phase coefficient
κ:	Complex Brillouin gain coefficient
κ_p:	Poisson ratio
λ:	Optical wavelength
μ_o:	Magnetic permeability
$\vec{\Pi}$:	Medium polarisation vector
θ:	Scattering angle
ρ:	Density
ρ_o:	Average material density
σ_s:	Shot noise
σ_T:	Thermal noise
τ:	Group delay

τ_B:	Phonon lifetime
ϖ:	Acoustic wave frequency
$\omega=2\pi\nu$:	Difference between Stokes and pump frequencies
$\omega_{as}=2\pi\nu_{as}$:	Stokes wave frequency
$\omega_B=2\pi\nu_B$:	Brillouin frequency
$\omega_p=2\pi\nu_p$:	Pump wave frequency
$\omega_s=2\pi\nu_s$:	Stokes wave frequency
Ω_{Bs}:	Normalised Brillouin frequency difference between stressed and unstressed components (normalised by Γ)
Ω_{obs}:	Observed Brillouin frequency difference between stressed and unstressed components (normalised by Γ)
Ω_{res}:	Resolved Brillouin frequency difference between stressed and unstressed components (normalised by Γ)

Chapter I: Introduction

I.A. Historical Perspective

In 1920, when Leon Brillouin presented his thesis "*Diffusion de la lumière et des rayons X par un corps transparent et homogène – Influence de l'agitation thermique*"[1], he probably did not suspect that his discovery would still generate passionate interest in the twenty first century. His research led him to the conclusion that density fluctuations in the medium can be associated with thermally generated sound waves. That thermal agitation is capable of scattering inelastically any incident lightwave i.e. the scattering products are shifted in frequency[2]. About fifteen years were necessary to gain a comprehensive understanding of the phenomenon. In fact, in 1930, Gross's experiments have shown that the scattered spectra are constituted by the two Brillouin components and one unshifted peak. The Brillouin peaks are the Stokes and the anti-Stokes lines, which are down- and up-shifted in frequency, respectively. These frequency shifts are proportional to the acoustic mode velocity. The broadening of the peaks is due to the attenuation of the sound waves. Eventually Landau and Placzek (1934) explained that the central line is due to non-propagating temperature fluctuations. The field then did not really progress due to the lack of intense monochromatic sources and sensitive spectrometers. We then have to wait until 1964, and the advent of the lasers era, to record new advances on the topic (Chiao 1964). With the development of high-resolution spectrum analysers, accurate measurements of the frequencies, intensities and

[1] The thesis can be translated as "*Light and x-rays scattering by a transparent homogeneous body – Effect of thermal agitation*". The work has been published as an article in 1922 (Brillouin 1922)

[2] The same effect was studied independently by Mandel'stham and published in 1926 (Schroeder 1977).

linewidths of the various lines are possible giving access to the characterisation of acoustic and thermodynamic properties of materials, e.g. sound velocity, sound attenuation coefficients, elastic constants, isothermal compressibility. These properties are still studied with the help of Brillouin scattering (Levelut 2006). The seventies see the introduction of optical fibres and the first observations of spontaneous and stimulated Brillouin scattering in silica waveguides (Ippen 1972, Rich 1974). Here the interest was triggered by the impairment that stimulated Brillouin scattering would cause to transmission links (Smith 1972). Since then, the interest never ceased, as many potential applications of Brillouin scattering in optical fibres are investigated. We can mention optical amplifiers (Olsson 1986), fibre lasers (Bayvel 1989), narrowband and tuneable filtering (Tkach 1989a). More recently, researches have shown that the propagation time of pulses in optical fibres can be controlled thanks to the Brillouin resonance (Okawachi 2005, Song 2005). Among all these applications, we retain the works of Horiguchi and Culverhouse, both in 1989, where the authors demonstrated that Brillouin scattering can be used to measure strain and temperature respectively, initiating a prolific research in fibre optic sensors (Horiguchi 1989, Culverhouse 1989).

I.B. Structural Health Monitoring

The sensing capabilities of Brillouin scattering are certainly of interest for civil engineering applications where a new field, known as Structural Health Monitoring (SHM), is currently developing. According to Bisby, "....*structural health monitoring can be defined as a non-destructive in-situ structural evaluation method that uses any of several types of sensors which are attached to, or embedded in, a structure. These sensors obtain various types of data (either continuously or periodically), which are*

then collected, analyzed and stored for future analysis and reference. The data can be used to assess the safety, integrity, strength, or performance of the structure, and to identify damage at its onset." (Bisby 2004). Various factors have driven the emergence of SHM. First, public infrastructures of industrialised countries are subjected to a strong "pressure". They are overused, leading to accelerated ageing. Moreover, the infrastructures are often old not to say obsolete e.g. 40% of the bridges in Canada are 50 years old (Bisby 2004). In many cases, replacement is not immediately possible due to a lack of public funding. Instead, strengthening and rehabilitation are considered as an option that would increase the lifetime of the current infrastructure. Determining when the structure needs to be repaired is then critical. That is only possible if an inspection strategy is in place. SHM can then be implemented to identify early signs of potential problems, allowing for prevention of disasters and repair of the damage. Second, SHM is also a tool that can help to improve the construction processes for new building materials and structures. These innovative structures response to stress can be studied thanks to a systematic layout of sensors and to the monitoring of their outputs.

I.C. Fibre Optic Sensors

Among the various sensing technologies that are considered for SHM, fibre optic sensors (FOS) are the most promising candidates (Kersey 1996, Tennyson 2000; Culshaw 2004, Thévenaz 2006a). Their advantages are inherent to the optical fibre properties. Being made of silica, the sensing medium is made of dielectric materials, which are immune to electromagnetic interferences. The sensors can be installed in remote locations as the fibre is a low loss transmission medium. Fibre optic sensors are small, light and non-corrosive, implying that they can be embedded without impacting

significantly the structure design. Finally, optical fibre technology is now a field mature enough so that the sensors can be laid on any structure shape and size i.e. a broad variety of optical components allows the multiplexing and the cascading of sensors. In addition, that capability is enhanced by the sensor type. In fact, FOS can be divided into two categories: point and distributed sensors. For point sensor, the sensing length (or gauge length) varies from centimetres to tens of meters. The sensing part is connected to the light source and the detection system by an optical fibre communication cable. In the case of distributed FOS, the fibre itself is the sensing medium, at any location, and the gauge length can be as small as tenths of metres over distances as long as tens of kilometres.

I.C.1. Point Sensors

Fibre Bragg gratings (FBG) and Fabry-Perot (FP) sensors are point gauges giving localised strain or temperature information. Long gauge (LG) sensors, which are based on a Michelson interferometer design, measure average strain over the gauge length, which can be as large as 200 m. Recently, application of LG sensors to pipeline integrity monitoring has been studied extensively (Tennyson 2006). All these sensors give only partial information on the stresses that affect the monitored structure as they measure local (FBG, FP) or average (LG) strains. Unless these sensors are in the proximity of local defects (e.g. cracks or buckling) they fail to detect such events. Moreover, these sensors only provide readings without correlation to structure status when the structure is under extreme environmental stresses. SHM capability is certainly enhanced if distributed strain information can be accessed. A large number of point FOS can be mounted on the structure to be monitored using multiplexing devices such

as those currently available on the market. It is then possible to achieve quasi-distributed sensing by assembling discrete fibre optic sensors into uni- or bidimensional arrays (Tennyson 2000, Culshaw 2005). There again, these configurations are efficient if the sensors are deployed in the vicinity of structurally critical zones.

I.C.2. Distributed Sensors

From what precedes, there is clearly a need for techniques that detect faults and assess the severity of the damage of the whole structure. Such sensor must perform distributed temperature or/and strain measurements over a few meters to tens of kilometres in real time, which is a clear advantage for structures such as pipelines, bridges, dams or river levees.

Three physical effects are identified as mechanisms for distributed sensing: Rayleigh, Raman and Brillouin scattering. The simplest distributed sensor is based on Rayleigh scattering and is widely used in optical communications to qualify optical links (Derickson 1999). It is known as the optical time domain reflectometer (OTDR). As the Rayleigh peak temperature dependence in normal fibres is weak, its implementation as a sensor requires the development of non-standard fibres[3]. These fibres have a liquid core (Hartog 1983), or, special core dopants that makes the Rayleigh peak more sensitive to temperature changes (Farries 1986). Special cables can also be used that convert the physical quantity (temperature, strain, pressure) variation into excess loss (Maclean 2003). Raman scattering is another effect that can be exploited to measure temperature over 10 kilometres to the maximum (Dakin 1985). Here, the sensing function is achieved by computing the ratio of the measured Stokes to anti-Stokes intensities, as it is

[3] "Standard" adjective used in the present thesis refers to optical fibres that are used in optical communications and whose nominal characteristics are determined by standardization bodies such as the International Telecommunication Union or the International Electrotechnical Committee.

an exponential function of temperature. Commercial Raman sensing systems are available on the market and are commonly used as fire detection systems in tunnels. At last but not least is the Brillouin sensor technique, which is capable of measuring both temperature (Culverhouse 1989) and strain (Horiguchi 1989) up to 50 km kilometres without signal regeneration (Bao 1995). In the Brillouin sensor, the sensing mechanism takes advantage of the linear relationship between the Brillouin frequency and temperature/tensile strain variations.

Brillouin sensor classification can be refined further by considering the configuration of the sensor. Two layouts can be distinguished which are Brillouin backscattering and stimulated Brillouin scattering configurations.

I.C.3. Brillouin backscattering configuration

The Brillouin backscattering configuration requires access to only one fibre end. The launched lightwave is spontaneously scattered by the acoustic waves everywhere along the fibre length. The scattered light is then collected and analysed at the input end. This configuration is also met in the OTDR and the Raman sensor. Spatial information, and, hence, events location is given by measuring the round trip of a pulse propagating in the fibre. This configuration has been implemented by various research teams.

The first Brillouin backscattering based sensor was developed by a research laboratory of NTT (Nippon Telephon and Telegraphs, Tokyo, Japan) and is known as the Brillouin optical time domain reflectometer (BOTDR) (Kurashima 1993). Their set-up uses coherent detection of the backscattered signal (Nazarathy, 1989). That is to say that the input light and the signal carrying the sensing information are optically

combined before reaching the photodetector. The beat product is recorded by a spectrum analyser and the Brillouin frequency can then be extracted. This set-up has led to the development of an instrument commercialised by Ando (AQ 8603 is the latest model).

The backscattering layout was also implemented by a group from the optoelectronic research centre (ORC, Southampton, United Kingdom) (Wait 1996). The main difference with NTT approach resides in the ability of the sensor to measure simultaneously strain and temperature. Temperature is calculated from the Landau-Placzeck ratio, which is the ratio of the Rayleigh peak to the sum of the Brillouin peaks intensities, while strain is measured from the Brillouin frequency shift.

A third group, from King's College (London, United Kingdom) has developed a sensor that computes strain and temperature from simultaneous measurement of the Brillouin frequency and power respectively (Parker 1998). Their solution is currently commercialised by Sensornet, an England based company.

I.C.4. Stimulated Brillouin scattering configuration

In this case, two lightwaves, the pump and the probe signals, are launched into the fibre in a counter-propagating configuration. The simultaneous presence of the Stokes and the pump waves generate a beat signal that reinforces the acoustic wave in the fibre when the beams frequency difference is equal to the Brillouin frequency. The coupling mechanism between the two lightwaves is electrostriction. The scattering of the pump is then enhanced, leading to its depletion and the input probe beam is amplified. The probe is also called Stokes as it corresponds to the frequency downshifted peak. The Brillouin spectrum can be recorded by tuning the frequency

difference between pump and Stokes waves. Two modulation schemes can be implemented to access to the distributed information. One of the two lightwaves is either pulsed (Horiguchi 1989a) or its amplitude sinusoidally modulated (Garus 1996). In the last case, the frequency of the modulation is time swept. When spatial information is obtained by pulsing one of the two light sources, the sensor is called Brillouin optical time domain analyser (BOTDA). In the other modulation format, the sensor name is Brillouin optical frequency domain analyser (BOFDA). The pulsewidth or the frequency sweeping range determines the spatial resolution of the sensor and then its gauge length. For both schemes, the signal detection is performed at the fibre end in which the modulated lightwave is launched. If the pump is modulated, the input Stokes is a continuous wave (*cw*) and the amplified probe is detected. The sensing mechanism is based on Brillouin gain and has been used by various research groups (Horiguchi 1989a, Bao 1993, Niklès 1996, Garus 1996, Hotate, 2000). Note that Niklès (1996) has proposed an advantageous design where only one laser is needed. They generate the Stokes wave by diverting a part of the pump signal and then apply a sinusoidal modulation at the Brillouin frequency. The lower side-band generated is the probe signal of their configuration. Since 2002, a BOTDA based on Niklès's design is proposed as a product by Omnisens (Lausanne, Switzerland). In the alternative of modulating the Stokes wave, the sensor records the pump output intensity variation. The pump is attenuated at the profit of the Stokes signal. The sensor is said to be a Brillouin loss system (Horiguchi 1989a, Bao 1993a). Two companies, Neubrex (Japan) and OZ Optics (Ottawa, Canada), work on a Brillouin loss BOTDA product inspired by the most recent developments of Bao's Brillouin loss configuration made at the University of Ottawa (see section I.*C*.6 for more details about the sensor specifics).

I.C.5. Brillouin sensor systems comparison and improvements

Various parameters need to be considered when comparing the Brillouin sensor systems. First, one has to keep in mind that the sensor must be implemented on the field. It must then be simple to install and complete the sensing operation as quickly as possible. Second, some of the sensor performances are critical. Those are the spatial resolution, which indicates the smallest detectable event size, the frequency resolution, which is the smallest Brillouin frequency shift that can be measured, and the measurement range, which is the longest length overwhich the sensor can make an accurate data acquisition.

The backscattering has obvious advantages over the stimulated approach. First, it only requires access to one fibre end. Second, if the fibre breaks, which is common in the field when the fibre is heavily stressed, measurements can still be done along the remaining section. On the drawbacks side, the backscattering approach relies on the emitted spontaneous intensity. These levels are usually low, necessitating long averaging time to achieve a satisfactory signal-to-noise ratio (SNR). That is not the case with the stimulated configuration where the intensity at the detector is significantly larger, reducing the overall measurement time.

The choice of the modulation format also has an impact on the sensor performance. For instance, small bandwidth receivers are needed in the BOFDA, reducing the electrical noise generated at the detection and in the amplifier stages. This gain in SNR decreases then the number of averages needed. Unfortunately, high spatial resolution and long distance range can only be achieved by increasing the frequency sweeping range and step size, respectively. Measurement time then rises significantly.

Measurement range of Brillouin sensor systems can be further extended by the aid optical amplification. A sensing length of 150 km with BOTDR based configuration from ORC has been achieved using optical Raman and Erbium doped fibre amplifier (EDFA) (Alahbabi 2006). In the case of BOTDA configuration, Omnisens proposes an all optical regeneration solution that increases the measurement range up to 250 km (Niklès 2005).

Spatial resolution can be improved by reducing the pulsewidth, in the case of time domain modulation, or broadening the frequency sweeping range, in the case of the BOFDA. Unfortunately, a better spatial resolution is obtained at the expense of frequency resolution. Hotate and co-workers have adapted the BOFDA configuration in such a manner that centimetre spatial resolution can be reached without penalising the frequency resolution (Hotate 2000, Hotate 2002). They proposed to modulate sinusoidally the amplitudes of both Stokes and pump waves with the same frequency generator. Both signals are emitted similarly to the set-up of Niklès (1996). When the phase of the two beams is the same, they interfere constructively creating a series of beat peaks along the fibre. By changing the modulation frequency, the distance between peaks is modified and spatial information can then be accessed. The drawbacks here are the measurement range, not greater than a few meters, and the measurement time, usually over hours.

I.C.6. The distributed Brillouin sensor

The sensor configuration used at the university of Ottawa is based on the Brillouin loss type BOTDA (Bao 1993a, Bao 1994). In the rest of this text, we will refer to it as the distributed Brillouin sensor (DBS). In a Brillouin loss set-up, measurement

range can be significantly improved without affecting the spatial resolution or increasing the measurement time. In fact, in the Brillouin gain case, the pulsed pump is attenuated while it propagates down the fibre, leaving little energy to amplify the Stokes signal in the last kilometres. To the contrary, in the Brillouin loss case, the Stokes signal is pulsed and the *cw* pump output is monitored. The probe pulse being amplified along the whole fibre, there is no location where the power is not enough to have Brillouin interaction and then sensing operation.

Spatial resolution can be improved without affecting frequency resolution by taking advantage of the DC component that is present in the optical pulse due to the leakage of the electro-optic modulator (Zou 2005, Kalosha 2006). A spatial resolution of 10 cm was achieved by using this approach.

The limitation to these performance improvements comes from the depletion of the pump, whose influence is felt at a larger distance than in the Brillouin Gain configuration. Due to the pulse amplification, the Stokes can become very large leading to an increase of pump depletion. This effect has two consequences. First, events that are distributed along the fibres can influence the measurement at any location, contributing to a contamination of the local spectrum and to the degradation of the measurement accuracy. We talk here about non-local effects (Bao 1995, Geinitz 1999). Second, a very large depletion would leave the last fibre sections without enough pump intensity to allow Brillouin interaction. The effect of pump depletion, and hence these two consequences, are enhanced by the presence of the pulse base.

I.D. The Present Thesis

How pump depletion affects the DBS performance and what remedies can be brought are the questions we will answer in the present thesis. To do so, we need to ground our investigation in the physics of Brillouin scattering. That is the reason why we first review carefully previous experimental and theoretical works. We introduce two models that we would use to carry out our research. Those models are analytical, based on weak depletion approximation, and numerical solutions of the coupled intensity equations for SBS (Chapter II). To validate the models, we studied experimentally and numerically Brillouin fibre generators and amplifiers (respectively BFG and BFA). We paid particular attention to the definition of the SBS threshold, giving an original interpretation of the experimental criterion used to measure it, and, generalising the threshold definition to the BFA configuration, which is a novel contribution to the field as well (Chapter III).

The background knowledge being settled, we enter into a detailed analysis of the DBS configuration. We take advantage of this step to discuss performance parameter definitions such as spatial resolution, frequency resolution and dynamic range. The BFA being the configuration used in the BOTDA type sensors, we see how the derived threshold definition can be considered as an upper limit of the input powers into the fibre to avoid degraded performance. We also show that small amount of depletion is necessary to achieve good operation of the sensor. We also determine the limit of applicability of the analytical model introduced in Chapter II. Using these results and taking care of the optimum power settings, we propose to adapt the analytical model to transient case. The time dependant effects are added phenomenologically so that the

model describes the sensor operation in function of the system parameters which are power (Stokes and pump), pulsewidth and extinction ratio as well as fibre length. This model can then handle transient effects and the influence of weak depletion (Chapter IV).

We use that phenomenological model to develop a unique signal processing method accounting for the physical mechanism on which Brillouin sensors are based. Until now, no such approach was ever developed for pulses shorter than 10 ns. This signal processing method is used in conjunction with original spectrum analysis tools specifically designed within the context of this research. These tools are the Length-Stress diagram (LS), the Rayleigh Equivalent Criterion (REC) and the form factors. They are introduced not only because experimental data can be contaminated with noise, but also because the measured spectra present complex structures. These complicated profiles contain useful informations as they reflect the complexity of the stresses distributions. Strain, or temperature, are rarely uniform over the gauge length leading either to multiple peaks spectral profiles, or to blurred spectra. When multiple peaks characterise the Brillouin spectrum, the data analysis is facilitated by the REC, which is a peak discrimination tool. We show that this criterion improves the spatial resolution by a factor of half while the error on the extracted Brillouin frequency shift remains lower than a few percent. When the REC is inoperant, i.e. the spectrum is blurred, we propose to use the form factors to first analyse the broadening and the asymmetry of the profile. When these form factors are reported on the LS diagram, the strain (temperature) information hidden in the measured profile can be estimated. The whole data analysis methodology is implemented in an iterative approach to reconstruct the

Brillouin spectrum distribution along the fibre length. The strength of this approach resides in its physics inspired components, the phenomenological model, the spectral analysis tools, that contribute to speed up the iterative process (Chapter V).

Eventually we take the DBS to civil engineer laboratories where we use it to monitor structures as different as steel pipes and concrete/FRP[4] columns. We demonstrate, for the first time to the best of our knowledge, that the DBS, in combination with the developed data analysis methodology, leads to the detection of localised defects such as buckling, concrete crushing as well as FRP debonding and rupturing (Chapter VI).

After summarising the whole work carried out and suggesting tracks for future developments in a conclusion chapter, we discuss, in Appendix C, the value of a multidisciplinary approach when high technology instruments have to make their way to the vast and remote world.

[4] Fibre reinforced polymers

Chapter II: Physics of Brillouin scattering

II.A. Introduction

Working at the improvement of the distributed Brillouin sensor requires learning the physics of Brillouin scattering. The present chapter is then dedicated to the study of the principles lying behind the system, and, to the building of the foundations of our research. We first remind the concept of spontaneous scattering and emphasize the role played by acoustic waves in the Brillouin interaction. As the non-linear nature of the interaction is a key element of the DBS operation, we discuss how electrostriction can lead to the stimulation of the scattering. We then derive the coupled equations that describe mathematically the behaviour of the amplitudes and phases of the lightwaves contributing to the interaction. We discuss more specifically these equations, their numerical solutions as well as the approximations that we will use in the rest of the thesis. This discussion is supported by numerical and experimental characterisation of spontaneous and stimulated Brillouin scattering.

II.B. Light scattering

II.B.1. General concepts

A monochromatic light beam propagating in a gaseous medium interacts with the molecules (the wavelength is assumed to be large compared to the particles size). Near a resonance of the molecules, the beam can be absorbed. If the wavelength of the probe beam is far from a medium resonance, the electric field induces a time dependent polarisation of the atoms or the molecules. The induced dipole generates in turn a

secondary wave, which is said to be scattered. Light scattering is then the emission of a secondary wave by a medium subjected to an electromagnetic stimulus whose frequency is off-resonance. In low-pressure gases, the distance between particles is larger than the probing light wavelength. In that situation, the particles are not influencing each others, producing uncorrelated scattering, and, then an incoherent resulting beam. Consequently, the intensity scattered by the whole medium and observed in a given direction is the sum of the intensities scattered by each individual scattering centre.

In condensed matter or in a high-pressure gas, the distances between scattering centres are smaller than the wavelength of light so that the secondary lightwaves are coherent. The estimation of the resulting intensity must be done by adding the scattered fields. When the medium is perfectly homogeneous, the phase relationship of the emitted waves is such that only the forward scattered beam can be detected while destructive interferences dominate in other directions of observation. The medium can then be considered as continuous and an optical beam propagation is determined by its refractive index (resulting from coherent scattering). Small inhomogeneties in a medium can be associated to a local change of the refractive index and can generate observable scattering... and scattering is everywhere. The nicest and most known example is certainly the Tyndal effect for which the explanation is known as "Lord Rayleigh's theory of the blue of the sky" (Kociński 1978). In 1871, Lord Rayleigh proposed that at atmospheric pressure, the air can be considered as a homogeneous medium contaminated with impurities smaller than the wavelength of light. Those impurities provoke incoherent scattering of the sunlight that leads to the coloration of the sky. Another spectacular phenomenon, famous among physicists, is critical opalescence

where the light scattered by a fluid is very intense at the liquid-vapour transition (Chu 1974, Kociński 1978). Von Smoluchowski (1908) and Einstein (1910) attributed the excess of the scattering to a dramatic increase in the fluctuations[5] of the local density of the fluid at the critical temperature (e.g. at the vapour-liquid phase transition temperature). These local density fluctuations alter locally the dielectric constant and hence the refractive index.

A long path has been covered since the beginning of the last century, both theoretically and experimentally. Light scattering has been studied extensively and used to study the properties of materials. Various light scattering mechanisms have been discovered and are shown in the schematic of Figure II.1 under the most general conditions (Boyd 2003). The centre line is the Rayleigh scattering that occurs without frequency change. Such scattering is said to be *elastic*. It is attributed to non-propagating density fluctuations. The two lines appearing on both sides of the Rayleigh peak, known as the Brillouin lines, are due to the scattering of the incident beam by a sound wave, which is a propagating density variation. Alternatively, it can be said that the lightwave is scattered by acoustic phonons. The left peak, corresponding to a frequency downshift, is called the Stokes peak while the right peak, frequency upshifted, is called the anti-Stokes line. Raman lines come from the interaction of the lightwave with molecular vibrations in the medium (or optical phonons). Both Brillouin and Raman scattering are *inelastic* scattering processes because they are associated with a frequency shift. The last mechanism that can be observed is the Rayleigh wing scattering attributed to fluctuations in the orientation of anisotropic molecules.

[5] According to Landau and Lifschitz (1967, 1969), the fluctuation of a physical quantity is a small temporal and/or spatial deviation from its average value.

Molecules with isotropic polarisability tensor do not experience Rayleigh Wing scattering. This is clearly the case for glass and optical fibres as the silica molecule is *centro-symmetric.*

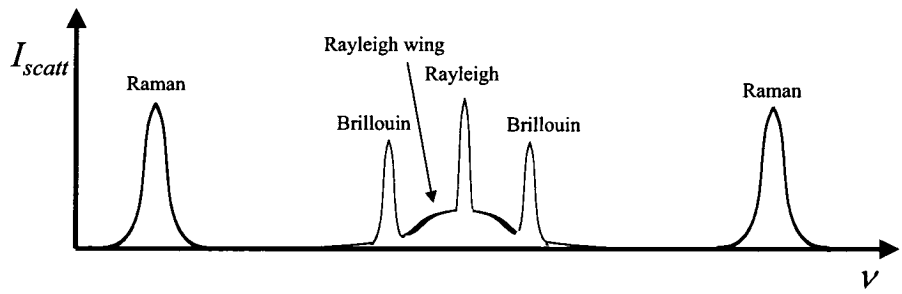

Figure II.1: Schematic of the observed scattered light intensity. Frequency and intensity axis are not scaled to reproduce accurately the peaks heights and frequencies (Boyd 2003).

As long as the input light is scattered without strongly altering the properties of the medium, we will say that the scattering is *spontaneous.* When the light intensity increases enough to modify the optical properties of the medium and then modify the scattering, the regime becomes *stimulated.* In other words, the evolution from spontaneous to stimulated scattering corresponds to the transition of the medium behaviour from linear to non-linear regime.

II.B.2. Optical properties fluctuations and light scattering

In a homogeneous and isotropic dielectric medium such as glass, the response of the medium to an electric field ($\vec{E}$) is described by the polarisation vector ($\vec{\Pi}$) defined as

$$\vec{\Pi} = \varepsilon_0 \chi \vec{E}, \qquad \text{(II.1)}$$

where ε_0 is the vacuum dielectric constant and χ the medium susceptibility. We have seen that scattering is provoked by fluctuations $\Delta\varepsilon$ of the medium dielectric constant ε.

These fluctuations can then induce a small polarisation $\vec{\Pi}_s$ such that the displacement vector $\vec{D}_s$ of the scattered field can be expressed as a linear combination of scattered ($\vec{E}_s$) and input fields ($\vec{E}_p$) (Landau 1969)

$$\vec{D}_s = \varepsilon_0 \varepsilon \vec{E}_s + \Delta\varepsilon \vec{E}_p = \varepsilon_0 \varepsilon \vec{E}_s + \vec{\Pi}_s . \tag{II.2}$$

The spatial (x, y, z) and temporal (t) dependence of the scattered wave must then be described by the perturbed wave equation

$$\nabla^2 \vec{E}_s - \left(\frac{n}{c_0}\right)^2 \frac{\partial^2 \vec{E}_s}{\partial t^2} = \mu_0 \frac{\partial^2 \vec{\Pi}_s}{\partial t^2} \tag{II.3}$$

where μ_o is the magnetic permeability of vacuum, c_o is the velocity of light in vacuum and n is the refractive index of the medium.

Rigorously, $\Delta\varepsilon$ is a tensor even for an isotropic medium, which can be separated into three components: a scalar scattering, a symmetric scattering and an anti-symmetric scattering (Landau 1969, Boyd 2003). Fluctuations of pressure, temperature, entropy and density, i.e. all thermodynamic fluctuations, are at the origin of scalar scattering, and hence, at the origin of Brillouin and Rayleigh scattering. Mathematically, scalar scattering is given by the trace of the fluctuation tensor and we will keep the default notation to be $\Delta\varepsilon$. Symmetric and anti-symmetric scattering are associated with the reorientation (Rayleigh –wing scattering) and optical polarisability change of molecules (Raman scattering) in the presence of an electric field, respectively.

II.C. Spontaneous Brillouin scattering in a single-mode optical fibre

II.C.1. Single-mode optical fibre specifics

In the present work, we consider the simplest optical fibre model, based on Agrawal's descriptions (Agrawal 1995, Agrawal 1997), which is a cylindrical optical waveguide composed of a core and a cladding. Radially, the fibre has a step index profile (SI: Step Index). The material for both core and cladding is silica glass (SiO_2). The core refractive index is increased by adjunction of dopants, such a GeO_2, while the cladding refractive index can be reduced by adding B_2O_5, for example. At a given wavelength, the fibre can carry many modes depending on its opto-geometrical properties, which are the core radius and the relative refractive index difference between core and cladding (Δ). When the core radius and Δ are reduced, there is a wavelength for which the fibre will allow only one mode. Typically, a fibre becomes single-mode at telecommunication wavelengths (starting at 1.3 μm) when the core radius is 5μm and $\Delta \approx 10^{-3}$. $\Delta << 1$ has other consequences. In fact, the fibre is said to be weakly guiding and the mode is linearly polarised. For a perfectly symmetric waveguide, the fibre actually supports two but degenerated modes. In the whole monograph, we will assume that the degenerateness is holding and any variation due to deviations in the radial symmetry will be discussed when needed. Within the same weakly guiding approximation, for step-index fibres and in the wavelength range of interest (1.3 to 1.6 μm), the radial intensity follows closely a Gaussian distribution characterised by the spot size r_o defined as the 1/e intensity width. The electric field propagating in the fibre is then considered as a plane wave with a Gaussian radial distribution. The direction of the propagation is the *z*-

axis. Typical optical and mechanical properties for such type of fibre can be found in ITU-T G.652 recommendations (ITU G.652).

At this stage, we want to introduce the relationship between the optical power in the fibre, P, and the total intensity distributed in the fibre. Assuming Gaussian radial distribution the power can be expressed as

$$Power = I_0 \pi r_0^2 = I_0 A_{eff}. \tag{II.4}$$

As it appears in this relation, when the intensity has a Gaussian distribution, the power is the product of the peak intensity I_o with the effective area of fibre A_{eff}. The effective area can be interpreted as the area of the fibre cross section over which the peak of the intensity distribution is constant (Agrawal 1995).

II.C.2. Density fluctuations and acoustic waves

As we are interested in $\Delta\varepsilon$ variations induced by thermodynamic quantities, we first consider ρ and T as independent thermodynamic variables and write the dielectric constant as (Chu 1974, Boyd 2003)

$$\Delta\varepsilon = \left(\frac{\partial\varepsilon}{\partial\rho}\right)_T \Delta\rho + \left(\frac{\partial\varepsilon}{\partial T}\right)_\rho \Delta T. \tag{II.5}$$

According to Fabelinskii (Fabelinskii 1968), the second term can be neglected because density fluctuations affect the dielectric constant significantly more than temperature fluctuations (the error of not taking that term into account is 2%). We now expand the density fluctuations in term of pressure (p) and entropy (s) fluctuations (Chu 1974, Boyd 2003)

$$\Delta\rho = \left(\frac{\partial\rho}{\partial p}\right)_s \Delta p + \left(\frac{\partial\rho}{\partial s}\right)_p \Delta s. \tag{II.6}$$

The first term corresponds to adiabatic density fluctuations and must be associated to pressure waves i.e. to acoustic waves. That term is at the origin of Brillouin scattering. The second term is an isobaric density fluctuation (which are entropy or temperature fluctuations) and leads to Rayleigh scattering. The model that describes the first term is a pressure wave while the second term is a diffusion equation (Chu 1974, Boyd 2003). We must then expect that both contributions can be easily distinguished on a scattering spectrum. Focusing on Brillouin scattering, the dielectric constant fluctuation density can be expressed as

$$\Delta\varepsilon = \left(\frac{\partial\varepsilon}{\partial\rho}\right)_T \left(\frac{\partial\rho}{\partial p}\right)_s \Delta p = \frac{\gamma_e}{\rho_0}\left(\frac{\partial\rho}{\partial p}\right)_s \Delta p, \tag{II.7}$$

where the electrostrictive constant γ_e, which will be discussed in section I.C., is defined (Chu 1974, Boyd 2003) as

$$\gamma_e = \rho_0 \left(\frac{\partial\varepsilon}{\partial\rho}\right)_T, \tag{II.8}$$

ρ_o being the average density of the material.

At thermal equilibrium, the pressure fluctuations in silica are attributed to thermally generated phonons[6]. In bulk silica, a longitudinal and a degenerated transverse modes coexist and can be observed (Rich 1972). Due to the geometry of the fibre, both cladding and core acoustic modes can propagate (Rich 1974, Rowell 1979,

[6] As early as 1914, Brillouin realised that density fluctuations could be associated with thermally excited sound waves, which were discovered by Debye in 1912 (Chu 1974).

Jen 1985). If the optical wave and the acoustic modes do not significantly overlap, as it is the case in the cladding of step-index fibres, the scattering is weak and can be barely detected. In the core, only forward and backward directions are of interest. Shear modes produce a scattering that can only be detected in direction normal to the fibre axis (Rich 1974, Rowell 1979, Thomas 1979). Remaining is the longitudinal mode which is obviously a pressure wave inducing periodic variations of the density, and, hence a density wave. That is the reason why we propose to write the dielectric constant fluctuation as a function of density fluctuations instead of pressure fluctuations

$$\Delta\varepsilon = \frac{\gamma_e}{\rho_0}\Delta\rho. \tag{II.9}$$

If we assume that the sound wave propagates along the fibre optical axis, then density fluctuation propagates according to (Boyd 2003)

$$\frac{\partial^2\Delta\rho}{\partial t^2} - \Gamma'\frac{\partial^2}{\partial z^2}\left(\frac{\partial\Delta\rho}{\partial t}\right) - V_A^2\frac{\partial^2\Delta\rho}{\partial z^2} = 0 \tag{II.10}$$

where Γ' is the damping parameter and V_A the velocity of the acoustic wave. Note that it is a good approximation to consider density waves instead of pressure waves as we deal with small pressure, and, therefore, small density variations (Feynman 1964).

II.C.3. Interaction of acoustic and optical waves

Although the propagation of the acoustic and the optical waves is constrained to the fibre axis, we consider the general expression for the incident optical wave (Chu 1974, Boyd 2003)

$$E_p = \frac{1}{2}A_p \exp\left[j\left(\omega_p t - \vec{k}_p.\vec{r}\right)\right] + c.c., \tag{II.11}$$

where ω_p and $\vec{k}_p$ are the incident optical wave frequency and wave number, respectively. The acoustic wave is expressed as

$$\Delta\rho = \frac{1}{2} Q \exp\left[j(\varpi t - \vec{q}.\vec{r})\right] + c.c., \tag{II.12}$$

where ϖ and $\vec{q}$ are the acoustic wave frequency and wave number, respectively. The scattered field can be derived by introducing equations (II.9), (II.11) and (II.12) in the perturbed wave equation (II.3) giving

$$\nabla^2 E_s - \left(\frac{n}{c_0}\right)^2 \frac{\partial^2 E_s}{\partial t^2} = \frac{\mu_0 \gamma_e}{4\rho_0} \left\{ (\omega_p + \varpi)^2 A_p Q \exp\left[j(\omega_p + \varpi)t - j(\vec{k}_p + \vec{q})\vec{r}\right] + (\omega_p - \varpi)^2 A_p Q^* \exp\left[j(\omega_p - \varpi)t - j(\vec{k}_p - \vec{q})\vec{r}\right] \right\} + c.c.. \tag{II.13}$$

It is clear from equation (II.13) that the presence of an acoustic wave in the medium contributes to the generation of two new spectral components that are the Stokes (second term) and the anti-Stokes waves.

II.C.4. Spectrum of spontaneous scattering

Let us now discuss these two terms in more details. The Stokes wave is characterised by a wave number

$$\vec{k}_s = \vec{k}_p - \vec{q}, \tag{II.14}$$

and a frequency

$$\omega_s = \omega_p - \varpi. \tag{II.15}$$

The Stokes emission is downshifted in frequency of an amount equals to the acoustic wave frequency. In a quantum physics picture, these two equations express the

conservation of momentum (II.14) and energy (II.15): an incident photon is absorbed leading to the emission of a Stokes photon and an acoustic phonon. The scattering process can be schematically represented by Figure II.2. For a scattering angle $\theta=\pi$, the representation clearly depicts that a co-propagating acoustic wave scatters the incident wave and generates a backward Stokes wave (backscattering case).

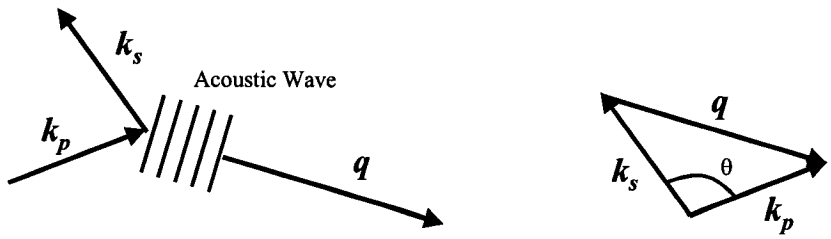

Figure II.2: Schematic of the generation of a Stokes wave by Brillouin scattering (Boyd 2003).

The various quantities in equations (II.14) and (II.15) are linked together by the dispersion relations

$$\omega_s = k_s c_0/n, \quad \omega_p = k_p c_0/n, \quad and, \quad \varpi = qV_A. \tag{II.16}$$

The acoustic wave involved in the process must simultaneously satisfy equations (II.14), (II.15) and (II.16) meaning that an acoustic wave of a given frequency scatters a lightwave in a definite direction, defined by the angle θ (Figure II.2). The frequency shift associated with the Stokes wave thus depends on the scattering direction. As the acoustic wave frequency is much smaller than the incident and scattered optical frequencies, we have that $k_p \approx k_s$ and then, according to Figure II.2, we can write

$$q = 2k_p \sin(\theta/2), \tag{II.17}$$

and using the dispersion relations (II.16) for the acoustic wave, we obtain the Brillouin frequency shift ν_B:

$$\nu_B = \frac{2nV_A}{\lambda_p}\sin(\theta/2), \tag{II.18}$$

where λ_p is the wavelength of the incident light. In an optical fibre, the scattering is observed along the optical axis. In the forward direction, the Brillouin frequency shift is zero as θ=0 while it is maximum in the backward direction (θ=π):

$$\nu_B = \frac{2nV_A}{\lambda_p}. \tag{II.19}$$

Typically, the Brillouin frequency shift is 11 GHz when measured at 1.55 μm and 13 GHz if the incident wavelength is 1.3 μm.

A similar approach can be applied to the anti-Stokes. The momentum and energy conservation relations would then be expressed as

$$\vec{k}_{as} = \vec{k}_p + \vec{q}, \tag{II.20}$$

$$\omega_{as} = \omega_p + \varpi. \tag{II.21}$$

The anti-Stokes emission is upshifted in frequency by an amount equals to the acoustic wave frequency. In a quantum physics representation, an incident photon is absorbed leading to the emission of a Stokes photon and the absorption of an acoustic phonon. A schematic shown in Figure II.3 pictures the anti-Stokes process. The backscattering case obviously shows that that a counter-propagating acoustic wave scatters the incident wave and generates an anti-Stokes wave. As in the Stokes process, the Brillouin frequency shift is the maximum when observed in the backward direction (equation II.19).

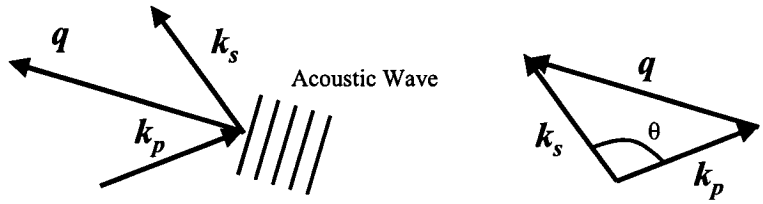

Figure II.3 Schematic of the generation of an anti- Stokes wave by Brillouin scattering (Boyd 2003).

An experimental spectrum showing the elastic and inelastic contribution to scalar scattering is presented in Figure II.4. Rayleigh scattering clearly dominates Brillouin scattering by three orders of magnitude.

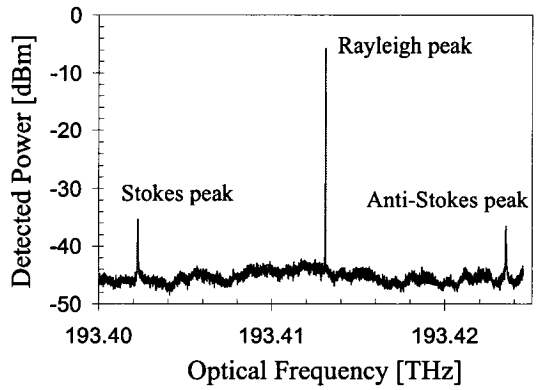

Figure II.4: Brillouin and Rayleigh lines obtained by the backscattering of an incident lightwave (λ_p = 1554 nm) in a 20 km long single-mode optical fibre (SI). The incident power is 412 μW. Details of the experimental set-up are provided in Chapter III. Measured Brillouin frequency shifts are 10.85 GHz.

We have not yet addressed the issues of the acoustic wave decay which can not be neglected as it determines the Brillouin spectrum linewidth. The acoustic wave equation (equation II.10) includes a damping term. In fact, a sound wave propagates in bulk silica (Vacher 1976, Heiman 1979, Vacher 1997, Levelut 2006) and in optical fibres (Rowell 1979, Thomas 1979) over a few microns only, their attenuation coefficient (~ 10^6 m^{-1}) being much larger than the optical attenuation coefficient in the telecommunication window (~ 10^{-4} m^{-1}). The actual origin of the decay is still an active

research topic as suggested by recent publications (Levelut 2006). At room temperature, the main cause of the decay currently evoked is acoustic wave scattering induced by material impurities. In the present work, we assume that the acoustic wave intensity decays exponentially (Chu 1974)

$$|\Delta\rho|^2 = |Q_0|^2 e^{-\Gamma_B |t|}, \tag{II.22}$$

where Q_o is the amplitude and Γ_B is the decay rate of the acoustic wave. By introducing the expression of the acoustic wave (relations (II.12) and (II.22)) in the density wave propagation equation (II.10), we find that the decay rate is (Boyd 2003)

$$\Gamma_B = q^2 \Gamma'. \tag{II.23}$$

It is commonly accepted in the literature that the decay rate is the inverse of the phonon lifetime τ_B (Agrawal 1995, Agrawal 1997). The exponential decay has the consequence that the Brillouin lines in the backscattered spectrum must have a Lorentzian shape whose full width at half maximum (FWHM) is defined as

$$\Delta\nu_B = 1/2\pi\tau_B = \Gamma_B/2\pi \tag{II.24}$$

Figure II.5 shows an example of Stokes spectrum measured in spontaneous regime on a SI single-mode optical fibre (thick hazed curve). The experimental spectrum is compared with a Lorentzian shape of identical FWHM. The root-mean-square relative difference between the two spectra is less than 2% suggesting that exponential decay conjecture is reasonable (the largest error contribution in the comparison of the two curves comes from the tails where the experimental spectrum is noisier). Using the data of Figure II.5, the phonon lifetime is estimated to be 10 ns as the experimental spectrum

linewidth is 31 MHz, which a value broadly quoted in the related literature (Agrawal 1995, Agrawal 1997).

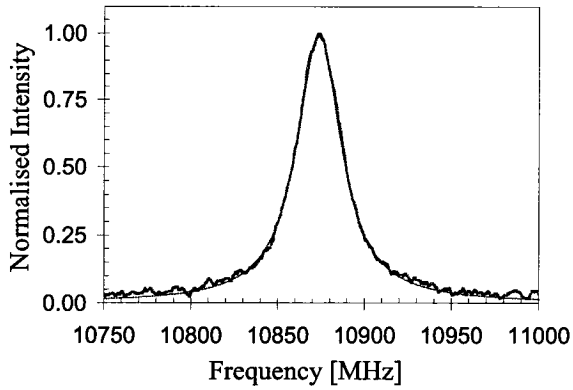

Figure II.5: Thick curve: Backscattered Stokes spectrum from an incident lightwave (λ_p = 1554 nm) in a 20 km long single-mode optical fibre (SI) obtained by a heterodyne method (Nazarathy 1989, Derickson 1998); the incident power is 310 μW; details of the experimental set-up are provided in Chapter III; Measured Brillouin frequency shift is 10873.6 MHz and linewidth is 31 MHz. Thin curve: Lorentzian distribution drawn with the measured Brillouin frequency and linewidth.

An estimate of the scattered power can be obtained by assuming that in spontaneous regime, the number of Stokes photons generated is proportional to the number of acoustic phonons (N_{ph}) present in the medium. At room temperature, $N_{ph} \approx k_B T / h \nu_B$ which is an approximation of Bose-Einstein distribution. The scattered power can then be evaluated by $P = N h \nu_S \Delta \nu_B$. For the typical values of Figure 5, the power is about 0.5 nW.

II.D. Stimulated Brillouin scattering in a single-mode optical fibre

As seen in the previous section, spontaneous scattering is attributed to the presence of inhomogeneities in the fibre. In the case of the Brillouin scattering, thermal agitation is the origin of these inhomogeneities, which is a process independent of the input light intensity. The scattered intensity would vary proportionally with the input

intensity. According to the description of Stokes scattering, a significant increase of input intensity would contribute to the rise of the number of co-propagating phonons in the fibre. We then can suspect that thermal agitation is no longer the only source of acoustic waves in the medium. Acoustic phonon generation becomes driven by the incident lightwave. The acoustic phonon number increase enhances the scattering, shifting the process from spontaneous to stimulated regime. Stimulated Brillouin scattering (SBS) were experimentally evidenced in crystals by Chiao (1964) and in an optical fibre by Ippen (1972). From a macroscopic point of view, there is a physical mechanism that accounts for material density change induced by an electric field in an isotropic body. This effect is known as electostriction (Chiao 1964, Shen 1976, Boyd 2003).

II.D.1. Electrostriction

Qualitatively, electrostriction can be understood as a tendency of a material to become compressed when subjected to an electrical field (Landau 1969, Boyd 2003). Such effect is commonly observed in centro-symmetric (quartz, saphire) crystals and glasses (Chiao 1964, Maldutis 1985). The pressure that strains the body can be derived from energy considerations.

The potential energy per unit volume stored in a dielectric subjected to a uniform electric field is

$$U = \frac{1}{2}\varepsilon_0 \varepsilon |E|^2, \qquad \text{(II.25)}$$

as it would be if the medium is inserted between the two plates of a condenser (Landau 1969, Feynman 1964, Boyd 2003). In a constant field, any change in the density $\Delta\rho$ would modify the dielectric constant according to

$$\Delta\varepsilon = \frac{\partial\varepsilon}{\partial\rho}\Delta\rho, \tag{II.26}$$

and affect the energy per unit volume as

$$\Delta u = \frac{1}{2}\varepsilon_0 |E|^2 \Delta\varepsilon. \tag{II.27}$$

In a non-dissipative process, the potential energy variation must be equal to the work done to compress the material (to increase its density). The work done per unit volume can then be written

$$\Delta w = -p_e \frac{\Delta\rho}{\rho_0}. \tag{II.28}$$

where p_e is the electrostrictive pressure, i.e. the pressure that must be applied to the medium to increase its density. Combining expressions (II.28), (II.26), (II.27) and (II.28), we obtain an expression for the electrostrictive pressure which is

$$p_e = -\frac{1}{2}\varepsilon_0\rho_0\frac{\partial\varepsilon}{\partial\rho}|E|^2 = -\frac{1}{2}\varepsilon_0\gamma_e|E|^2. \tag{II.29}$$

It appears that the electrostrictive constant γ_e is the proportionality coefficient between the induced pressure and the square of the applied electric field. The electrostrictive pressure is negative suggesting that the material tends to become compressed in the region of higher electric field. Consequently the material density is higher in regions of

larger electric field. An inhomogeneous field in the material would induce density variations that imply microscopic mass motions. In the present work, we do not deal with static fields but with fields oscillating at optical frequencies. At these frequencies, the material would appear transparent, unless two optical fields are present simultaneously. In that situation, the propagating fields can produce beat signals at frequencies at which matter can respond. In other words, there can be a resonant interaction between the beat electric field and pressure (density) waves of the material. In the case of optical fields, the electrostrictive pressure must be written as

$$p_e = -\frac{1}{2}\varepsilon_0 \gamma_e \left\langle \left|\vec{E}\right|^2 \right\rangle, \tag{II.30}$$

where $\vec{E}$ is the total electric field and the brackets denote a time average over an optical period.

II.D.2. Electrostriction and SBS

The electrostrictive pressure results from the propagation of at least two ligthwaves in the medium. Moreover the frequency difference between the two optical waves equals the induced acoustic wave frequency. We have seen that in spontaneous scattering the excited Stokes wave counter-propagates and has a frequency lowered by the phonon frequency[7]. Together, incident and Stokes waves will produce a beat signal at the Brillouin frequency. The beat signal then induces a density wave enhancing the acoustic wave. That has the effect to increase number of phonons and consequently the efficiency of the scattering, leading eventually to stimulated regime. When SBS is initiated from spontaneous scattering, the medium is said to be a *Brillouin generator.*

[7] We will focus here on the Stokes wave and discuss the anti-Stokes case in section IV.

The beat wave can also be produced by launching another beam at the opposite end of the material. It is important here to ensure that the new wave is at the Stokes frequency. By extension, the new wave will always be called the *Stokes* signal and the input will be the *pump* signal. The configuration involving two incident lightwaves is then a *Brillouin amplifier*. The process leading to SBS is illustrated in Figure II.6.

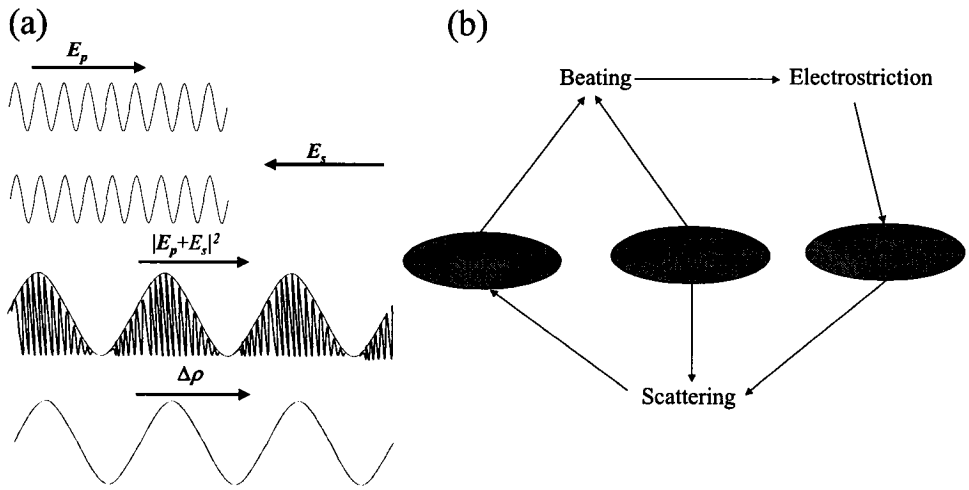

Figure II.6: (a) schematic and of the acoustic wave generation through electrostriction: Stokes and pump waves counter-propagate, produce a beat wave that in turn induces a density wave via electrostriction; (b) Schematic of SBS generation (Niklès 1997).

II.D.3. Formal description of SBS

From the preceding section, it is clear that the formal description of SBS involves the study of the interaction of three waves: pump, Stokes and acoustic wave. We can introduce some simplifications because our purpose is to treat SBS in single mode optical fibres. Due to the fibre symmetry and according to the phase matching condition introduced in the spontaneous section (equations (II.14) and (II.15)), only axial propagation (along the z axis) and backscattered Stokes wave need to be considered. We consider that the pump and the acoustic waves are propagating in the positive direction of the fibre (growing z) while the Stokes wave is counter-propagating.

Moreover, to obtain an efficient interaction between pump and Stokes waves, as it would be the case in a Brillouin amplifier, their frequency difference ($\omega = \omega_p - \omega_s$) needs to be close to the peak of the Brillouin spectrum (equation (II.19.)). Typically, the condition $|\omega - \omega_B| < \Gamma_B$ has to be respected.

The total optical field (E) involved in the interaction is $E=E_p+E_s$ where pump (E_p) and Stokes fields (E_s) are defined by (Boyd 2003)

$$E_p = \frac{1}{2} A_p(z,t)\exp[j(\omega_p t - k_p z)] + c.c., \tag{II.31.a}$$

$$E_p = \frac{1}{2} A_s(z,t)\exp[j(\omega_s t + k_s z)] + c.c.. \tag{II.31.b}$$

The acoustic wave is a density distribution expressed as follows (Boyd 2003)

$$\rho(z,t) = \rho_0 + \Delta\rho(z,t) = \rho_0 + \frac{1}{2}\{Q(z,t)\exp[j(\omega t - qz)] + c.c.\}. \tag{II.31.c}$$

Temporal and spatial evolutions of the optical fields is given by the two perturbed wave equations (Boyd 2003)

$$\nabla^2 E_p - \left(\frac{n}{c_0}\right)^2 \frac{\partial^2 E_p}{\partial t^2} = \mu_0 \frac{\partial^2 P_p}{\partial t^2}, \tag{II.32.a}$$

$$\nabla^2 E_s - \left(\frac{n}{c_0}\right)^2 \frac{\partial^2 E_s}{\partial t^2} = \mu_0 \frac{\partial^2 P_s}{\partial t^2}, \tag{II.32.b}$$

while the acoustic wave spatial and temporal dependence of the density are modelled by a forced acoustic wave equation (Boyd 2003)

$$\frac{\partial^2 \Delta\rho}{\partial t^2} - \Gamma' \frac{\partial^2}{\partial z^2}\left(\frac{\partial \Delta\rho}{\partial t}\right) - V_A^2 \frac{\partial^2 \Delta\rho}{\partial z^2} = \frac{\partial^2}{\partial z^2} p_e. \tag{II.32.c}$$

where the source term has been added to the right-hand side of equation (II.10) to account for the wave density induced by the optical fields through electrostriction.

We then calculate the source term by inserting the total field (sum of equations II.31.a and b) into the expression of the electrostrictive pressure (equation II.30), by keeping the terms oscillating at the acoustic frequency and making assumption that the amplitudes of the optical fields vary slowly in space and time (*slowly varying envelope approximation*). The result is

$$\frac{\partial^2 p_e}{\partial z^2} = -\varepsilon_0 \gamma_e q^2 A_s^* A_p \exp[j(\omega t - qz)] + c.c. \tag{II.33}$$

Introducing the expression of the density wave (equation II.31.c) in equation (II.32.c.) and making the assumption that the amplitudes of the acoustic wave vary slowly in space and time, we obtain the following expression for the acoustic amplitude

$$j\Omega \frac{\partial Q}{\partial t} + jqV_A^2 \frac{\partial Q}{\partial z} + \frac{1}{2}\left(\omega_B^2 - \omega^2 - j\omega\Gamma_B\right)Q = -\frac{1}{2} q^2 \varepsilon_0 \gamma_e A_s^* A_p \tag{II.34}$$

This equation can be further simplified by omitting the second term in the left-hand side. In fact, the acoustic waves are attenuated over very short distances (< 10 μm) such that the source term appears to be constant (right–hand side of equation (II.34)) (Niklès 1997a, Boyd 2003).

The wave equations also have a source contribution that affects the propagation of the optical fields. Here acoustic waves changing the dielectric constant are induced by the optical fields themselves. The general expression for the polarisation is derived from equations (II.26), (II.29) and (II.31.c) yielding

$$\Pi = \varepsilon_0 \Delta\varepsilon E = \varepsilon_0 \gamma_e \frac{\Delta\rho}{\rho_0} E \tag{II.35}$$

The only components of the polarisation that can influence the Stokes (pump) waves must oscillate at the Stokes (pump) wave frequency. We only keep the terms that satisfy, in equation (II.35), such phase matching condition. The derivation leads to two expressions for the polarisation that are

$$\Pi_p = \frac{1}{4}\frac{\varepsilon_0 \gamma_e}{\rho_0}\left\{Q A_s \exp\left[j(\omega_p t - k_p z)\right] + c.c.\right\}, \tag{II.36.a}$$

$$\Pi_s = \frac{1}{4}\frac{\varepsilon_0 \gamma_e}{\rho_0}\left\{Q^* A_p \exp\left[j(\omega_s t + k_s z)\right] + c.c.\right\}. \tag{II.36.b}$$

We can now combine these two equations with the optical wave equations (II.31.a and b) and the expressions of the optical fields (II.32.a and b). By making the approximation of the slowly varying envelopes, we neglect the second derivatives of the optical field amplitudes against space and time. We then obtain a set of three coupled differential equations

$$\left[\frac{\partial}{\partial z} + \frac{n}{c_0}\frac{\partial}{\partial t} + \frac{\alpha}{2}\right] A_p = -j\frac{k_p \gamma_e \varepsilon_0}{4\varepsilon\rho_0} Q A_s, \tag{II.37.a}$$

$$\left[\frac{\partial}{\partial z} - \frac{n}{c_0}\frac{\partial}{\partial t} + \frac{\alpha}{2}\right] A_s = j\frac{k_s \gamma_e \varepsilon_0}{4\varepsilon\rho_0} Q^* A_p, \tag{II.37.b}$$

$$j\omega\frac{\partial Q}{\partial t} + \frac{1}{2}\left(\omega_B^2 - \omega^2 - j\omega\Gamma_B\right) Q = -\frac{1}{2} q^2 \varepsilon_0 \gamma_e A_s^* A_p, \tag{II.37.c}$$

where we introduced $\varepsilon = \mu_o (n/\mu_o c_o)^2$ and the linear attenuation coefficient of the fibre α (Agrawal 1995). This set of equations describes completely the interaction between two

counter-propagating lightwaves and an acoustic wave. These equations do not have analytical solutions and require numerical analysis. Further in the text, we will refer to them as the *three waves equations*.

II.D.4. Solutions for steady state approximation

Analytical solutions can be derived from the three waves equations by considering the steady state approximation, which is valid for continuous wave light beams (*cw*) and long pulses (pulses whose width is much longer than the phonon lifetime). Once the time derivatives are dropped, we find an expression for the acoustic wave envelope

$$Q = -jq^2\gamma_e\varepsilon_0 \frac{A_s^* A_p}{\left(\Omega^2 - \Omega_B^2\right) + j\Omega_B\Gamma_B} \approx -j\frac{q^2\gamma_e\varepsilon_0}{\Omega_B\Gamma_B} \frac{A_s^* A_p}{1 - 2j\dfrac{\Omega_B - \Omega}{\Gamma_B}} \tag{II.38}$$

The second equality is valid when the frequency difference between the two optical waves is close to the Brillouin frequency and is comprised within the order of magnitude of the Brillouin linewidth i.e. we need to be close to the resonance. We then obtain the following set of two coupled differential equations for the pump and Stokes field

$$\frac{\partial A_p}{\partial z} = -\frac{1}{2} g_B \frac{I_s}{1 - j2\dfrac{\Omega_B - \Omega}{\Gamma_B}} A_p - \frac{\alpha}{2} A_p, \tag{II.39.a}$$

$$\frac{\partial A_s}{\partial z} = -\frac{1}{2} g_B \frac{I_p}{1 + j2\dfrac{\Omega_B - \Omega}{\Gamma_B}} A_s + \frac{\alpha}{2} E_s. \tag{II.39.b}$$

where the intensity is defined as $I=(n\varepsilon_o c_o/2)\,|A|^2$ and g_B is the centre line Brillouin gain coefficient (Agrawal 1995. Boyd 2003) which is expressed as

$$g_B = \frac{k\gamma_e^2 \varepsilon_0 q^2}{\varepsilon \rho_o \Omega_B \Gamma_B n c_0} \tag{II.40}$$

when we remember that in Brillouin scattering $k_p \approx k_s \equiv k$. For single-mode fibres, g_B varies from 1.12×10^{-11} to 5×10^{-11} m/W, depending on core doping and structure (Nikles 1997, Nikles 1997a). Equations (II.39) can be rewritten in a more compact form:

$$\frac{dA_s}{dz} = -\frac{\kappa^*}{2} I_p A_s + \frac{1}{2}\alpha A_s, \tag{II.41.a}$$

$$\frac{dA_p}{dz} = -\frac{\kappa}{2} I_s A_p - \frac{1}{2}\alpha A_p, \tag{II.41.b}$$

We introduced here the complex gain coefficient κ that can be written as

$$\kappa(\Delta\nu) = g(\Delta\nu) + j\varphi(\Delta\nu) = \frac{g_B}{1+(2\Delta\nu/\Delta\nu_B)^2} + j\frac{(2\Delta\nu/\Delta\nu_B)g_B}{1+(2\Delta\nu/\Delta\nu_B)^2}. \tag{II.42}$$

Here g_B is the centre line Brillouin gain coefficient and $\Delta\nu = (\omega_B - \omega)/2\pi$ is the detuning frequency. The first term is the well-known Brillouin gain coefficient. The second term is the Brillouin phase coefficient and is related to the refractive index of the gain medium. If the Stokes wave originates at $z=L$ and the pump at $z=0$, we assume that the solutions have the form

$$A_p(z,\Delta\nu) = A_p(0,\Delta\nu)\exp\left[\frac{1}{2}G_p(z,\Delta\nu) + j\Phi_p(z,\Delta\nu)\right], \tag{II.43.a}$$

$$A_s(z,\Delta\nu) = A_s(L,\Delta\nu)\exp\left[\frac{1}{2}G_s(z,\Delta\nu) + j\Phi_s(z,\Delta\nu)\right], \tag{II.43.b}$$

where G_s (G_p) is the Stokes (pump) intensity coefficients, which is gain in the case of the Stokes beam (loss in the case of the pump beam) and Φ_s (Φ_p) is the Stokes (pump) phase

coefficient (Ravet 2006). Substituting this ansatz in equations (II.41) and replacing κ by equation (II.42), we obtain the solutions for pump and Stokes phases as follows:

$$\Phi_s = -\int_L^z \frac{\varphi}{2} I_p(\xi, \Delta\nu) d\xi, \tag{II.44.a}$$

$$\Phi_p = -\int_0^z \frac{\varphi}{2} I_s(\xi, \Delta\nu) d\xi. \tag{II.44.b}$$

φ can be moved out of the integral when the Brillouin frequency distribution is constant over the whole fibre length (Ravet 2006).

The intensities, $I_s(z,\Delta\nu)$ and $I_p(z,\Delta\nu)$, can be calculated by solving the coupled intensity equations for SBS which are derived from equations (II.41) by multiplying the pump (Stokes) equation by the conjugate of the pump (Stokes) amplitude and using the expression that relates intensity and amplitude (Agrawal 1995, Chen 1998). Those coupled intensity equations are

$$\frac{d}{dz} I_p = -g I_s I_p - \alpha I_p, \tag{II.45.a}$$

$$\frac{d}{dz} I_s = -g I_p I_s + \alpha I_s. \tag{II.45.b}$$

An analytical solution was obtained by Chen and Bao (1998). We use the same notation by defining $\Sigma(z,\Delta\nu)=I_p(z,\Delta\nu)+I_s(z,\Delta\nu)$ and $\Delta(z,\Delta\nu)=I_p(z,\Delta\nu)-I_s(z,\Delta\nu)$. Then the solutions for pump and Stokes intensities can be written in the implicit form by the following:

$$\Sigma = \left\{\left(\Sigma_0^2 - \Delta_0^2\right)\exp\left[(g/\alpha)(\Delta - \Delta_0)\right] + \Delta^2\right\}^{1/2}, \tag{II.46.a}$$

$$\int_{\Delta_0}^{\Delta} \left\{\left(\Sigma_0^2 - \Delta_0^2\right)\exp\left[(g/\alpha)(u - \Delta_0)\right] + u^2\right\}^{-1/2} du = -\alpha z, \tag{II.46.b}$$

where $\Sigma_0=\Sigma(0,\Delta\nu)$ and $\Delta_0=\Delta(0,\Delta\nu)$. The initial conditions of the coupled intensity equations are $I_p(0,\Delta\nu)=I_{p0}$ and $I_s(L,\Delta\nu)=I_{sL}$, where I_{p0} is the input pump intensity, and, I_{sL} is the input Stokes intensity. G_s (G_p) at z is given by the logarithm of the ratio of $I_s(z,\Delta\nu)$ ($I_p(z,\Delta\nu)$) to I_{sL} (I_{p0}). Appendix 1 describes the implementation of the Newton-Raphson method to solve Equations II.46 to obtain output pump and Stokes intensities as a function of position, frequency and input powers. Curves in Figure II.7 illustrate pump and Stokes power dependence as a function of launched pump power and position at the Brillouin frequency ($\Delta\nu = 0$). Figure II.7 suggests first that the Stokes power grows exponentially as the beam propagates toward the pump input. Second, a higher input pump increases the output Stokes power but also enhance the pump attenuation (the pump decrease is steeper in the 30 mW than in the 18 mW case). Pump attenuation is also known as *depletion*.

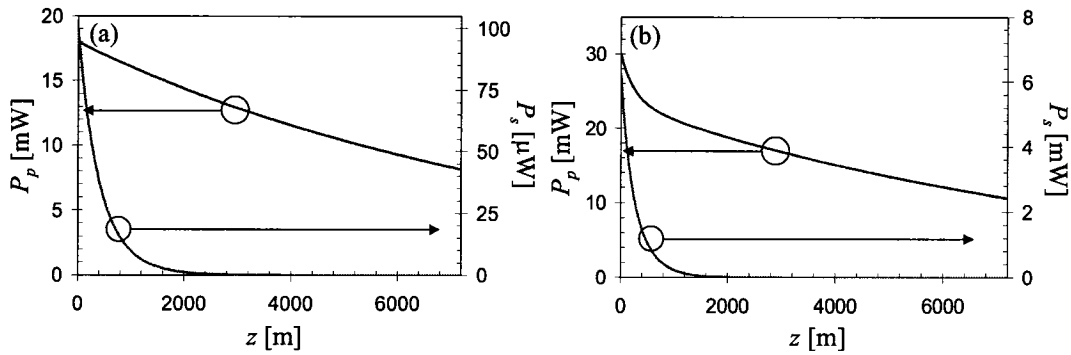

Figure II.7: Pump and Stokes power spatial dependence at the Brillouin frequency in a 7.2 km long single-mode optical fibre for (a) P_{p0} = 18mW and (b) P_{s0} = 30 mW; other simulation parameters are P_{sL} = 0.66 nW, α = 0.475 dB/km, g_B = 1.12 m/W, A_{eff}=78.6μm^2.

Once the phase of the Stokes wave is known, the group delay calculation is straightforward. Similarly, we can calculate the delay on a pump pulse. Stokes and pump group delay, noted as $\tau_s(z,\Delta\nu)$ and $\tau_p(z,\Delta\nu)$, respectively, are then expressed as

$$\tau_s = \frac{1}{2\pi}\frac{d\Phi_s}{d\Delta\nu} = -\frac{g_B}{2\pi\Delta\nu_B}\frac{1-(2\Delta\nu/\Delta\nu_B)^2}{\left[1+(2\Delta\nu/\Delta\nu_B)^2\right]^2}\int_0^z I_p d\xi - \frac{\varphi}{4\pi}\frac{d}{d\Delta\nu}\int_0^z I_p d\xi, \tag{II.47.a}$$

$$\tau_p = \frac{1}{2\pi}\frac{d\Phi_p}{d\Delta\nu} = -\frac{g_B}{2\pi\Delta\nu_B}\frac{1-(2\Delta\nu/\Delta\nu_B)^2}{\left[1+(2\Delta\nu/\Delta\nu_B)^2\right]^2}\int_0^z I_s d\xi - \frac{\varphi}{4\pi}\frac{d}{d\Delta\nu}\int_0^z I_s d\xi. \tag{II.47.b}$$

Complex gain coefficient can be moved out of the integral when the Brillouin frequency distribution is uniform as shown in the right hand side of equations (II.47) (Ravet 2006).

Typical examples of gain, phase and group delay frequency dependence are presented in Figure II.8 for a Stokes beam and Figure II.9 for a pump beam (Pump and Stokes intensities are computed according to the method presented in Appendix 1). Physical meaning can be extracted from these two sets of curves. Plain curve in Figure II.8.(a) shows that at the peak of the resonance of the Brillouin interaction (at the Brillouin frequency), the phase changes its sign from negative to positive (Figure II.8.(a), dashed curve). That has the effect to increase the group index. An increase in the group index decreases the group velocity provoking the retardation of a pulse propagating down the fibre i.e. the pulse takes more time to travel the fibre length. The maximum delay occurs at $\Delta\nu$=0, which is the peak amplitude of the group delay spectrum (Figure II.8.(b)). Another interesting behaviour is observed in Figure II.8. As the Stokes is amplified at the expense of the pump, the pump is *depleted*, and the resonance is inverted (Figure II.9.(a), plain curve) and the phase changes its sign from positive to negative (Figure II.9.(a), dashed curve) at the Brillouin frequency. That induces a decrease of the group index and an increase of the group velocity. Eventually the pulse will experience advancement, the total propagation time being reduced by the minimum of the group delay spectrum shown in Figure II.9.(b).

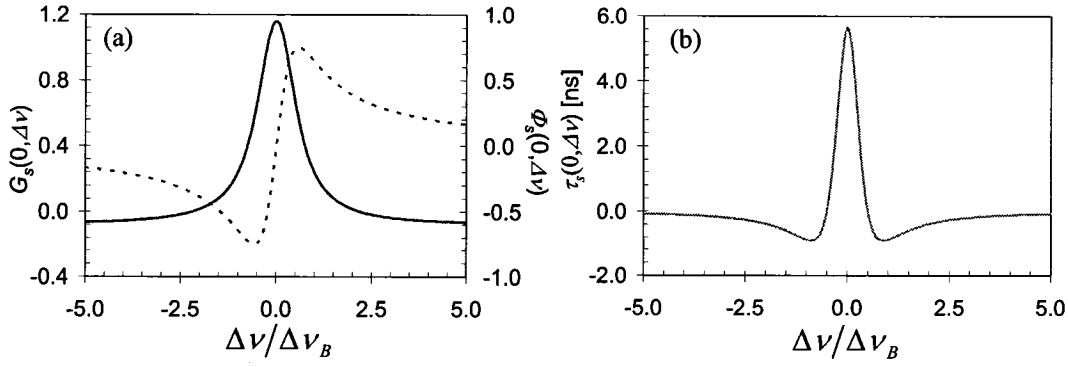

Figure II.8: (a) The plain curve is the Brillouin gain spectrum of output Stokes beam; the dashed curve is the phase of output Stokes beam; (b) group delay of output Stokes beam; Simulation parameters are P_{sL} = 1 mW, P_{p0} = 6 mW, L = 1000 m, z = 0 m, $\Delta\nu_B$ = 32 MHz, α = 0.2 dB/km, g_B = 2.3 m/W, A_{eff}=80μm^2.

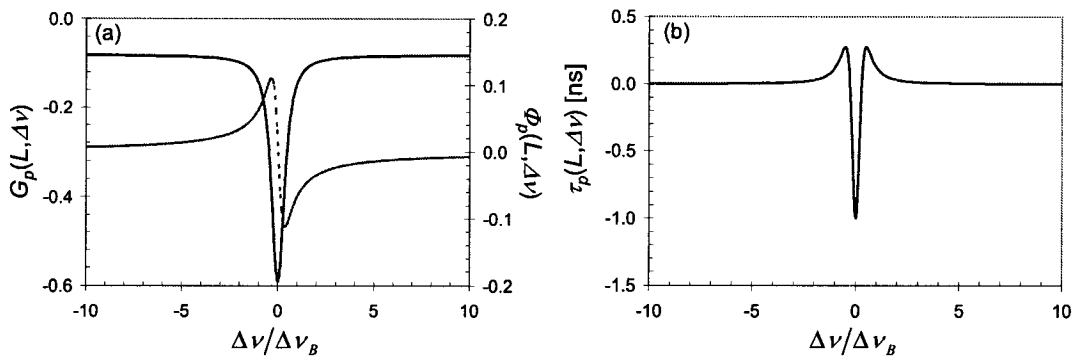

Figure II.9: (a) The plain curve is the Brillouin loss spectrum of output pump beam; the dashed curve is the phase of output pump beam; (b) Relative group delay of output pump beam; Simulation parameters are P_{sL} = 1 mW, P_{p0} = 6mW, L = 1000 m, z = 1000 m, $\Delta\nu_B$ = 32 MHz, α = 0.2 dB/km, g_B = 2.3 m/W, A_{eff}=80μm^2.

In contrast to a linear resonant medium, the various curves of Figures II.8 and II.9 are not only determined by the real and imaginary parts of equation (II.42). It is expected here, due to the nature of stimulated Brillouin interaction, that gain, phase and group delay vary locally. In fact, the shape, the width and the amplitudes of gain, phase and delay depend on the strength of the interaction, which is a function of the power, fibre length and local properties as well as position. That feature appears also in the off-resonance level of the gain. For instance, it is clear that in equation (II.42), the Brillouin

natural gain off-resonance level vanishes ($g(\Delta\nu)\rightarrow 0$ when $\Delta\nu\rightarrow +/-\infty$). The off-resonance level of G_s (and G_p) is negative due to the natural loss, which increases when the pulse propagates away from the fibre input.

II.D.5. Undepleted approximation and steady state condition

A very simple solution can be obtained by assuming that the pump is attenuated by the fibre loss only. In this case, the pump is said to be undepleted. It means that we neglect the Brillouin term in equation (II.45.a). The pump dependence with length is then a very simple result

$$I_p(L) = I_{p0} e^{-\alpha L}. \tag{II.48}$$

We introduced here the effective length that can be interpreted as the total length over which the pump remains constant. The Stokes intensity is obtained by replacing the pump intensity by its expression (equation II.48) in equation (II.45.b), which yields, after integration over the whole fibre length,

$$I_s(0) = I_{sL} \exp\left[g I_{p0} L_{eff} - \alpha L\right] \tag{II.49}$$

From this equation, it is clear that in the undepleted approximation, the Stokes intensity grows exponentially with input pump intensity, fibre length and position. In the case of the Brillouin generator, we assume that the input Stokes intensity is ignited from spontaneous scattering and has a power level equivalent to $N_{ph} h \nu_s \Delta\nu_B$ which is a fraction of a nanowatt. Figure II.7, where pump depletion is taken into account, also illustrates that the Stokes wave experiences an exponential growth against position.

The transition from spontaneous to stimulated regime is certainly not abrupt. As soon as both pump and Stokes waves propagate in the fibre, they can stimulate the acoustic wave. For Brillouin generators, spontaneous scattering acts as a seed that contributes to the stimulation of the effect. In this case, the question is then to find the pump power threshold for which the effect of scattering is significant enough to alter the property of the fibre, and, consequently to provoke an important depletion of the pump[8] (see also Figures II.7 for the effect of pump depletion). As early as 1972, the question was raised and answered by Smith (Smith 1972). Using a relation equivalent to equation (II.49) and considering spontaneous scattering only, he derived an approximate expression for the power threshold based on an arbitrary criterion: the threshold power is the pump input "power for which the backward stimulated Stokes power equals the input pump at z=0" (Smith 1972). This expression, corrected from Smith's original formula by a χ_{SBS} factor to account for depolarisation effects (van Deventer 1994, Bao 1995)[9], is

$$P_{th} \approx 21\frac{A_{eff}}{\chi_{SBS} g_B L_{eff}}. \qquad \text{(II.50)}$$

In most of the cases, χ_{SBS}=2/3. We will discuss the experimental validitation of this threshold definition in Chapter III. In the same chapter, we will also see how the threshold definition can be extended to Brillouin amplifiers and account for the input Stokes power.

Although formula (II.49) is simple to use and seems to reflect correctly the behaviour of the Stokes wave, the approximation made is such that it does not predict

[8] Such question is of particular interest for optical communication professionals who see SBS as a detrimental effect for their link budget.

[9] The depolarization effect is included in all the calculations of the present thesis by including χ_{SBS} in the Brillouin gain coefficient.

the pump behaviour even for moderate pump depletion[10] (when SBS induced attenuation becomes comparable or slightly larger than the fibre natural attenuation). Hopefully, it is not necessary to implement equations (II.46) to study moderate depletion regime. Starting from expression (II.49) and replacing the Stokes intensity in the pump intensity equation (equation (II45.a)), we obtain an expression for the pump intensity that partly accounts for depletion (Bao 1995)

$$I_p(L) = I_{p0} \exp\left\{ -\alpha L - \int_0^L g I_{sL} \exp\left[g I_{p0} \frac{e^{-\alpha L}}{\alpha} \left(e^{\alpha\zeta} - 1\right) - \alpha\zeta \right] d\zeta \right\}. \tag{II.51}$$

Equation (II.49) clearly predicts that the gain must grow as the pump power increases. That behaviour is shown in Figure II.10 (curve with filled squares). The output Stokes power for the depleted case calculated by the implicit solutions (equations (II.46)) is matching the undepleted result very well for input pump power lower than the calculated threshold (P_{th} = 17.94 mW). Similar observation can be made if we compare the output pump computed with equations (II.46) and (II.51). Again, the agreement between depleted and undepleted approximations fails when the pump power threshold is crossed. It is worthwhile to note that in a logarithmic representation, the power threshold is located near an inflexion point of the Stokes power curve. Mathematically it means that above the threshold, the Stokes power increases linearly instead of exponentially. Physically, this can be interpreted as a change in the stimulated emission regime. We will see in Chapter III that the Stokes power becomes saturated because the pump depletion is not negligible anymore.

[10] We will see in subsequent chapters that we definitely need to account for pump depletion, even weak, if we want to study SBS based fibre sensors

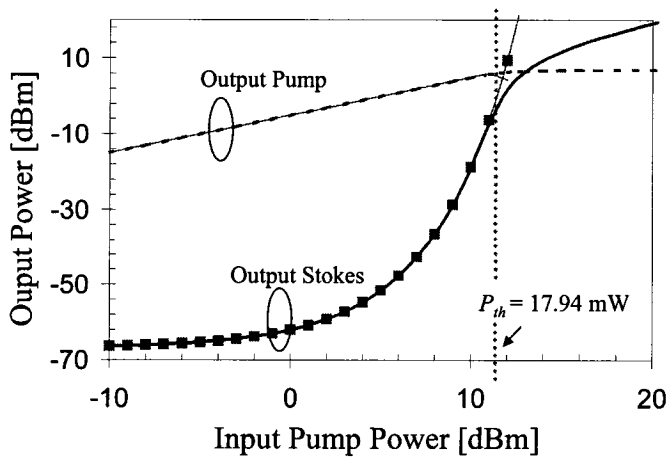

Figure II.10: This figure represents output power in a Brillouin generator as a function of pump input power, both expressed in dBm[11]. The thick plain curve is the output Stokes power calculated with equations (II.46) and is compared with the undepleted approximation; Similar comparison is made for the output pump computed with equations (42) (dashed curve) and the weakly depleted case (thin curve); Simulation parameters are typical for a SI fibre: P_s = 0.66 nW, L = 20000 m, α = 0.25 dB/km, g_B = 1.12 m/W, A_{eff}=80μm^2.

As a final comment to this section, we want to discuss the impact of neglecting pump depletion in the undepleted pump approximation. In that case, equation (II.47.a) reduces to the first term. The group delay at the Brillouin frequency becomes (Thévenaz 2006)

$$\tau_s = \frac{g_B I_p L_{eff}}{2\pi\Delta\nu_B}. \qquad \text{(II.52)}$$

The comparison of equation (II.52) and equation (II.47.a) shows that the pump frequency and position dependence of the pump intensity significantly impacts the delay. It is important to take pump depletion into consideration to have a complete picture of SBS induced delay in optical fibres.

[11] Power expressed in dBm is an absolute power measurement because it refers to a power variation from a power level fixed at 1mW. It is defined as $P_{dBm}=10\log_{10}(P_{mW}/1mW)$.

II.D.6. Transition from spontaneous to stimulated Brillouin scattering

We have seen that in the spontaneous regime, the Rayleigh line is the main contribution to the backscattered spectrum while Stokes and anti-Stokes components have a low but similar intensity (Figure II.4). When the pump power is increased, the Stokes power grows exponentially to eventually become the dominating peak of the backscattered spectrum (Figure II.11). As illustrated in Figure II.11.(c), the anti-Stokes line has completely disappeared in the stimulated regime. Actually, the highest pump power at which the anti-Stokes component could be measured is 50 mW (Figure II.11.(a)). Figure II.11.(a) also show a comparison of measurements and numerical simulations (equations (II.46)) where the agreement between experiment and model is very good.

The disappearance of the anti-Stokes component in stimulated regime can be understood with a simple physical picture. We have seen that the scattering process reinforces the acoustic wave co-propagating with the pump (Figure II.6). It can also be understood microscopically. In the Stokes process, a pump photon is annihilated, a Stokes photon and an acoustic phonon are created. The increase of the number of pump photon contributes to the rise of the number of phonons, stimulating the scattering and hence the generation of Stokes photons. In the anti-Stokes process, the scattering of a pump photon leads to the creation of a Stokes photon and the annihilation of an anti-Stokes phonon. The anti-Stokes process leads then to the decrease of the number of counter-propagating phonons, which contributes to reduce the efficiency of the process (Niklès 1997a).

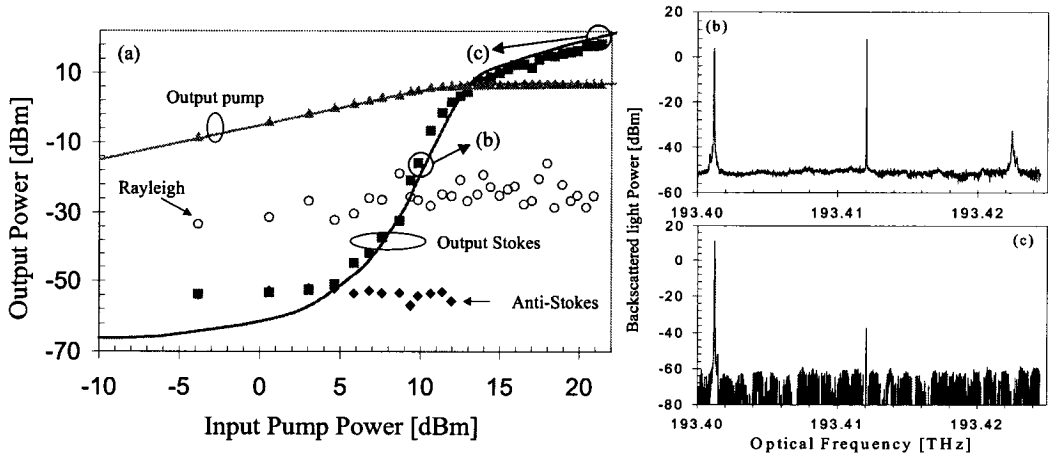

Figure II.11: (a) Output peak power versus input peak power obtained experimentally and numerically (simulation parameters same as in Figure II.10): output pump experimental (triangles) and numerical (plain line), Stokes experimental (square) and numerical (plain line), experimental anti-Stokes (diamond), experimental Rayleigh (open circles); complete backscattered spectrum for (b) P_{p0} = 15.63 mW and (c) P_{p0} = 122.74 mW; details of the experimental set-up are presented in Chapter III and Appendix 2. Measured fibre is SI type.

II.E. Summary

Spontaneous Brillouin scattering arises from the interaction of a lightwave (pump beam) with an acoustic wave. The acoustic wave is a propagating pressure wave inducing periodic variations of the density and consequently of the refractive index. The acoustic wave can then be viewed as a propagating grating that diffracts the incident wave. Doppler effect shifts the diffracted wave in frequency by an amount proportional to the acoustic wave velocity. Due to the optical fibre geometry, the only Brillouin scattering observed is backward and is composed of two components of similar intensities: Stokes and anti-Stokes lines. In such regime, it is a good approximation to consider that the scattered power grows linearly with the incident power.

When two counter-propagating lightwaves are simultaneously present in the fibre, both externally fed or simply produced by the backscattering of the pump, they

can beat and induce, by electrostriction, a temporal and spatial variation of the density. The density wave and the pump beam have the same direction of propagation. The acoustic wave in the fibre is enhanced as soon as the created density grating reaches its frequency. It then contributes to increase the Stokes scattering and hence the intensity of the Stokes beam. The process enters in the stimulated regime. The growth of the Stokes intensity is exponential (non linear) and become so large that it completely dominates the backscattered spectrum. The input pump has then crossed the power threshold. Above threshold, the Stokes power growth is linear again due to pump depletion effect.

Chapter III: Brillouin fibre generator and amplifier

III.A.Introduction

Chapter II was dedicated to the presentation of Brillouin scattering and of the main concepts as well as to the introduction of the analytical tools that will be used in this work. In this new chapter, which is still a background discussion, we want to study in some more details the Brillouin fibre generator and amplifier configurations. We first carry out a systematic study, experimentally and numerically, of the Brillouin generator in order to determine the validity and the range of applicability of the interaction model described by equations (II.46). Aware of their limitations, we then use them to study the Brillouin fibre amplifier and evaluate the discrepancy of the weakly depleted approximation for the pump wave (equation (II.51)).

We also take advantage of the present investigation to discuss Smith's formula (Smith 1972) and an experimental Brillouin threshold definition, which is the 1% input power criterion (Bayvel 1990). We then give a physical interpretation of the experimental definition of the SBS threshold, which leads to the proposal of two new thresholds definitions that are equivalent and based on the fact that the pump starts to be depleted once the threshold is reached. Because they are rooted in the physics of SBS, we see that these thresholds can unequivoquely be applied to the Brillouin amplifier configuration, which is equivalent to the layout of the sensor developed by our group. We also derive an original expression for the threshold in Brillouin fibre amplifier. This

threshold definition is certainly important for sensing applications as it sets a maximum input pump power to the Brillouin sensor, optimising its sensing operation.

III.B. Brillouin fibre generator

III.B.1. General configuration

As illustrated in Figure III.1, the Brillouin fibre generator (BFG) is composed of a pump signal and of an optical fibre. Backward waves, Rayleigh, Stokes and anti-Stokes, are emitted by the spontaneous scattering, which in turn initiates the stimulated regime. In such backscattering experiment, the emitted beams are measured at the pump input while the transmitted wave is detected at the other fibre end.

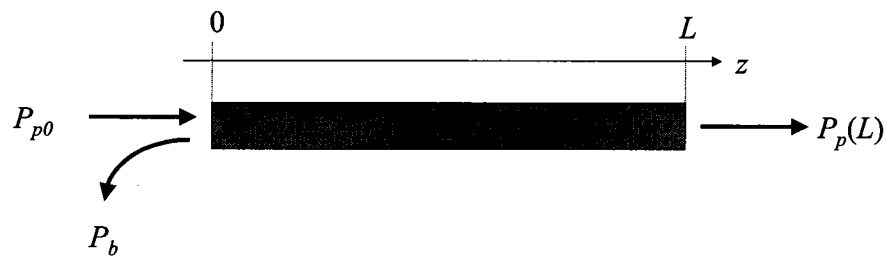

Figure III.1: Schematic of the Brillouin generator configuration and characterisation set-up. P_{p0} and $P_p(L)$ are input and output pump power respectively while P_b is the backscattered power.

III.B.2. SBS threshold

In principle, the threshold determination is the simplest backscattering experiment that can be carried out. It only requires the use of power meters in the Brillouin generator configuration. We implemented an experimental set-up based on the power meter approach (PMA) but we also introduced an additional instrument to monitor the backscattered spectrum, the Brillouin optical spectrum analyser, or BOSA (Appendix 2). The BOSA has a frequency accuracy of 0.01 GHz and a resolution bandwidth of 10 MHz. Power measurements with the BOSA are less accurate (relative

power accuracy is 1.50 dB) than measurements performed with a powermeter (relative power accuracy is 0.22 dB). That set-up was used to acquire the spectra and the power data presented in Figures II.4 and II.11. The fibre measured was a 20 km long SI fibre. We estimated the Brillouin frequency of the SI fibre to be 10.85 GHz with the BOSA when the the pump wavelength is 1554 nm. Using this set-up we also characterised a shorter SI type fibre (2 km), a triangular core refractive index fibre (LEAF: Large Effective Area Fibre; A_{eff} = 72 μm^2; Ruffin 2005), as well as two highly negative dispersion fibres (DCF: Dispersion Compensating Fibre) that are 8 km (A_{eff} = 15 μm^2) and 3.5 km (A_{eff} = 21 μm^2) long respectively.

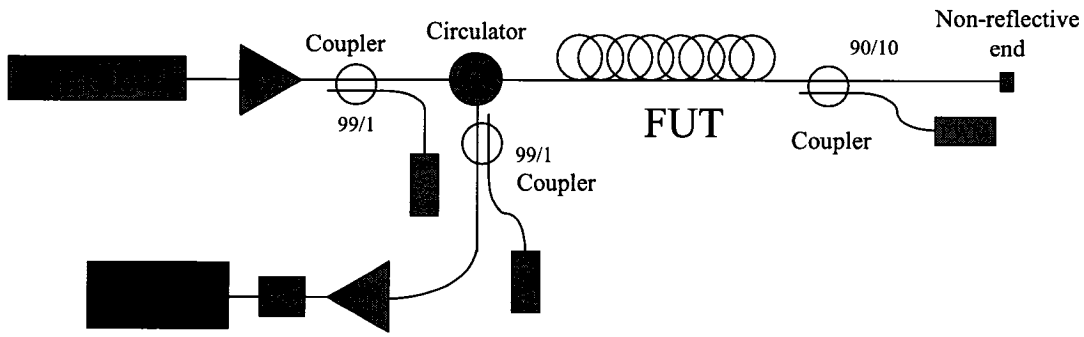

Figure III.2: Schematics of the backscattered signal measurement with the power meter approach (PWA) and the BOSA (ECL: External Cavity Laser, output power is 3 mW and linewidth smaller than 100 kHz; EDFA: Erbium Doped Fibre Amplifier, maximum output power is 250 mW; PWM: Power Meter; BPF: Band Pass Filter, bandwidth smaller than 1nm; FUT: Fibre Under Test).

Backscattered and transmitted power measurements on the 20 km SI fibre obtained with the PWA are shown in Figure III.3. The experimental conditions are the same as the ones used for these results presented in Figure II.11. It is not surprising that the backscattered power curve in Figure III.3 shows a large discrepancy at low input pump power with the Stokes curve in Figure II.11. The difference comes from the fact that in Figure III.3 the total backscattered power is measured and the three components

present in the spectrum (Rayleigh, Stokes and anti-Stokes) can not be discriminated. Actually, at lower input pump power, Figure II.11 showed that Rayleigh scattering is the dominant contribution of the backscattering process.

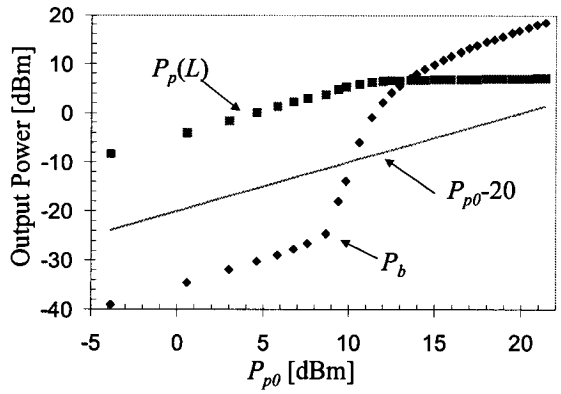

Figure III.3: Transmitted ($P_p(L)$, squares) and backscattered power measurements as a function of the input power ($P_b(0)$, diamonds). The plain curve is the 1% of the input power. Measured threshold is 10.57 mW (*1% criterion*) and calculated threshold is 18.94 mW (Smith).

In Chapter II, we have introduced Smith's definition stating that the SBS threshold is the input pump power "for which the backward stimulated Stokes power equals input pump power at $z = 0$" (Smith 1972). When observing Figure III.3 (as well as Figures II.10 and II.11), it is obvious that such definition is not practical at all: the backscattered power can barely be equal to the input power due to pump depletion. An experimental threshold definition that can be used is the input power at which the backscattered power reaches 1% of the input pump power (*1% criterion*), as it is illustrated by the plain curve in Figure III.3 (Bayvel 1990, Esman 1996). That definition also means that 1% of the pump input light is reflected by the Brillouin generator, and, according to Bayvel, corresponds approximately to a sharp increase (on a linear scale) of the backscattered power (Bayvel 1990). The threshold obtained on the measured backscattered spectrum of Figure III.3 according to the *1% criterion* is 10.57 mW with

the PMA and 10.39 mW with the BOSA (extracted from the Stokes line power variation of Figure II.11). Those values are smaller than the theoretical threshold obtained with Smith's definition, which is 18.94 mW[12].

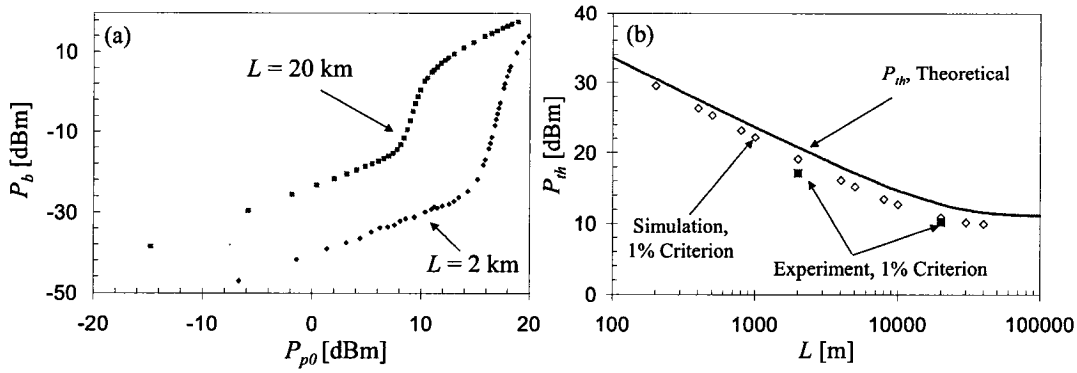

Figure III.4: (a) Backscattered power measurements as a function of the input power for two single-mode step index optical fibres (SI) of different length: L = 2 km (diamonds) and L = 20 km (square); the measured threshold is 10.57 mW for L = 20 km and 51.76 mW for L= 2km; (b) Power threshold as a function of fibre length measured with PWA and estimated with the 1% criterion (full square), calculated with Smith's definition (plain curve), calculated by simulation and estimated with the 1% criterion (open diamond); parameters for the simulation and Smith's threshold are: P_{sL} = 0.66 nW, α= 0.25 dB/km, g_B = 1.12 m/W, A_{eff}=80μm^2.

As suggested by the threshold definition and as illustrated in Figure III.4, Brillouin scattering threshold depends on the fibre length[13]. The scattering process reaches the stimulated regime for lower pump levels when the fibre length is increased. As shown in Figure III.4.(b), Smith's threshold definition (Equation (II.50)), the threshold derived from measurements (Figure III.4.(a)) with the *1% criterion* and the threshold calculated from simulations of Equations (II.46) show similar trends. Smith definition is systematically higher than both experimental and simulation results. We believe that there are two reasons why these threshold definitions do not match. First,

[12] Such difference can look insignificant but in applications such as long-haul optical communications, where each dB counts, it is critical to remain below threshold. Engineers are in a situation where they are limited by the maximum input power while they also need to push the link design to obtain the largest power budget.

[13] It is worth mentioning that the fibres are SI type from the same manufacturer but were not produced the same year. Their optical characteristics are nominally identical but not accurately the same.

Smith's definition is based on an undepleted approximation and Brillouin backscattered power levels that can not be achieved experimentally. Second, the *1% criterion* has no physical relationship with Smith's definition. Other authors have presented similar discrepancies with Smith's relation, that is to say a systematic overestimation of the threshold when it is compared with experiments (Billington 1999) or numerical approximations (Le Floch 2003), and some proposed corrected formula where the 21 factor was adjusted to fit their data (proposed values range from 16 to 19, depending on simulation parameters and experimental conditions).

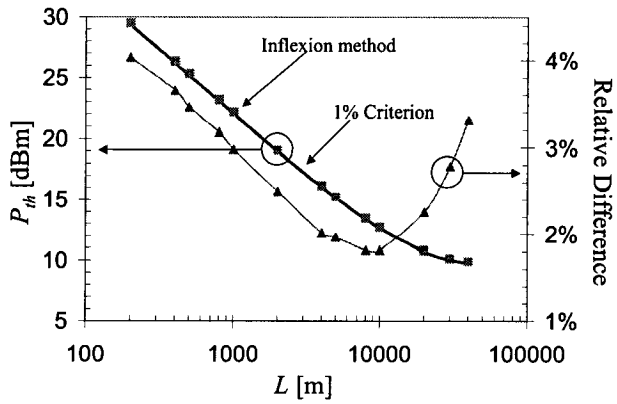

Figure III.5: Comparison of threshold calculations from the same simulated data by the 1% criterion (plain curve) and the inflexion method (full squares). The curve with the triangles is the relative difference between the two curves. Parameters for the simulation are: P_{sL} = 0.66 nW, α= 0.25 dB/km, g_B= 1.12 m/W, A_{eff}=80μm^2.

It could be argued that the *1% criterion* has no physical meaning and is a pure mathematical artefact. That last definition has obvious practical advantages: it is easy to use and it only requires backscattered power measurements. In addition, BOSA data, presented in Figure II.11, suggests that for these power levels, the spectral components that do not participate to SBS have little impact i.e. spectral components such as Rayleigh and anti-Stokes lines. An observation of the backscattered power curves (in dBm) shows that there is an inflexion point. On a linear scale, it is the point where the

exponential growth becomes linear. As mentioned in Chapter II, the change in the curve shape is induced by pump depletion. Interestingly, the 1% line intersects the backscattered power curve very close to the inflexion point. We computed the inflexion point abscissa of the simulated data and plotted the result in Figure III.5 (*inflexion method*). We compared the results with the thresholds obtained by the *1% criterion*. As it appears in Figure III.5, the inflexion method overestimates the threshold obtained with the *1% criterion* by less than a percent (for fibre lengths smaller or equal to 20 km). By extension, the 1% criterion can then be associated with a regime change in the SBS process. It gives the input power for which the pump power starts to be depleted. Equivalently, we can say that when 1% of the input power is reflected, the pump becomes depleted.

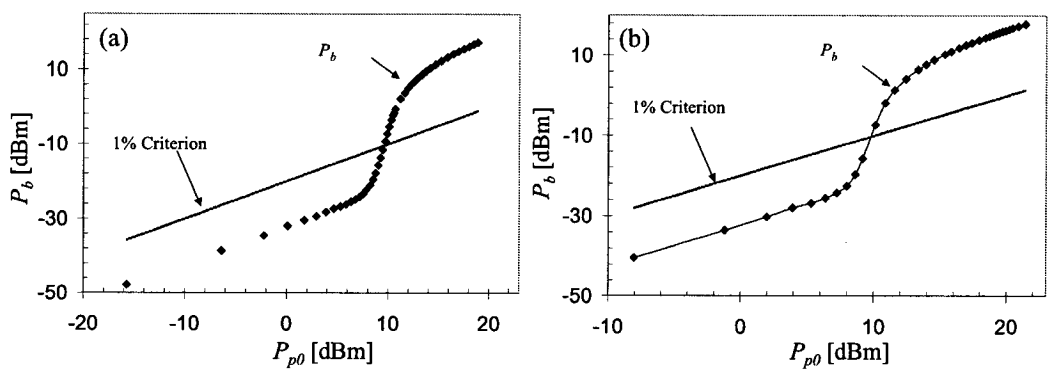

Figure III.6: (a) Backscattered power measurement for (a) a 25 km LEAF, and, (b) a 8 km DCF (A_{eff} = 15 μm^2). The measured threshold is 9.07 mW for the LEAF and 9.70 mW for the DCF.

The equivalence between the *1% criterion* and the *inflexion method* is not an accident. First it applies to any length of the same fibre type as illustrated in Figure III.5. Second, it is also observed in all experiments we conducted on the other fibre. Typical examples are presented in Figure III.6 and show backscattering data we obtained from measurements on LEAF (Figure III.6.(a)) and DCF (Figure III.6.(b)). In both

cases, the 1% criterion line crosses the backscattered power curve at its inflexion point. Their measured threshold (1% criterion) is 9.07 mW and 9.70 mW for LEAF and DCF respectively. Measured SBS threshold for the various fibre types can be found in Table III.1.

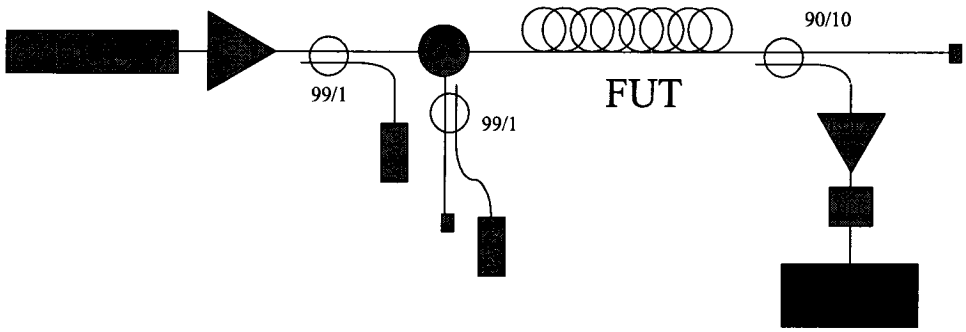

Figure III.7: Schematics of transmitted spectrum measurements with the BOSA and backscattered power with a power meter (PMA). The characteristics of the set-up are the same as in Figure III.2.

III.B.3. Transmitted spectrum characteristics

The spectrum of the lightwave, transmitted by the fibre, can be measured by modifying the set-up of Figure III.2, and, by replacing the power meter by the BOSA as shown in Figure III.7. Measurement results are presented in Figure III.8. These forward measurements, done on three different fibres (SI 20 km, LEAF 25 km, DCF 8 km, and DCF 2km), confirm that the transmitted pump (TP) power is depleted and then saturates when the threshold is crossed (Figures II.10, II.11, III.3). It also reveals features that were not resolvable in pure power measurements such as the appearance of a line in the forward spectrum at the Brillouin frequency of the fibre. That spectral component is the Rayleigh backscattering of the Stokes wave (RSS: Rayleigh Scattering of the Stokes wave). It becomes visible when the Stokes wave reaches the stimulated regime. At higher input pump power ($P_{p0} > P_{th}$), an additional line is observed at twice the Brillouin

frequency in LEAF and DCF (both 2 and 8 km) cases only. We attribute this spectrum component to the Brillouin scattering of the Stokes wave (SOS: Second Order Stokes wave).

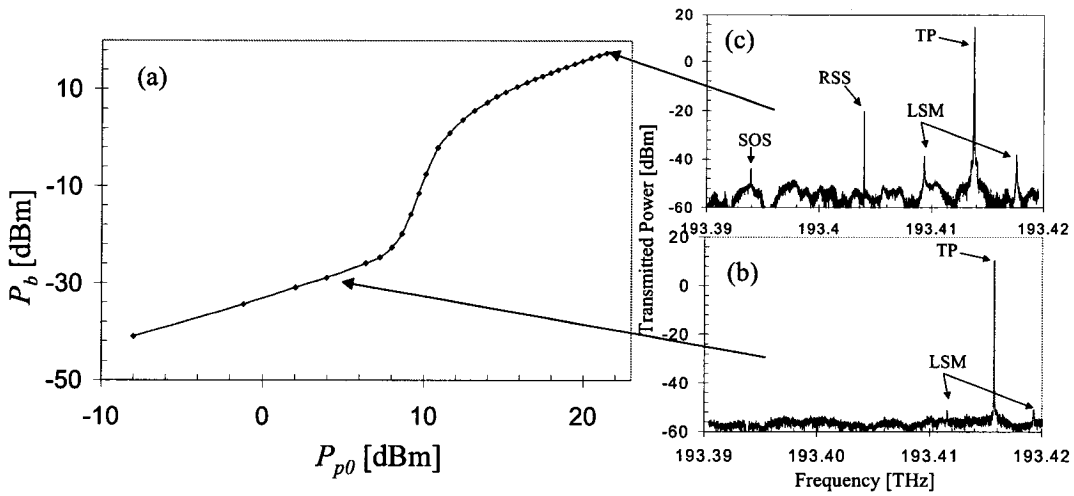

Figure III.8: (a) Backscattered power measurement from the 8 km long DCF; transmitted spectrum measured from the DCF for (b) P_{p0} = 3.38 mW and (c) P_{p0} = 138.36 mW (TP: Transmitted Pump; LSM: Laser Side Modes; RSS: Rayleigh Scattering of the Stokes wave; SOS: Second Order Stokes wave). Note that the presence of the side-modes was detected by a characterisation of the source spectrum.

III.B.4. Stokes spectrum characterisation

The resolution bandwidth of the BOSA is not small enough to study detailed spectral characteristics of the individual components generated by Brillouin scattering. Another approach must be followed. We propose here to measure the backscattered spectrum by using a heterodyne method (Nazarathy, 1989, Derickson 1998) presented in Figure III.9. In such technique, we combine the backward signal with a reference lightwave, in this case a fraction of the input pump, and detect the product of the mixing with a photo-detector (PD) of 32 GHz bandwidth. The electrical beat signal visualised and recorded with the electrical spectrum analyser is actually proportional to the square of the optical intensity at the photodetector. The resolution bandwidth of the electrical

spectrum analyser (ESA) is smaller than 100 kHz. Each spectrum is the result of an average of 100 acquisitions over a frequency span of 1 GHz. The spectrum shown in Figure II.5, that represents the Stokes spectrum coming out of the 20 km long SI fibre, is measured with this set-up. As in the threshold study, we also investigated the spectral properties of the 2 km long SI, the LEAF and the DCF's.

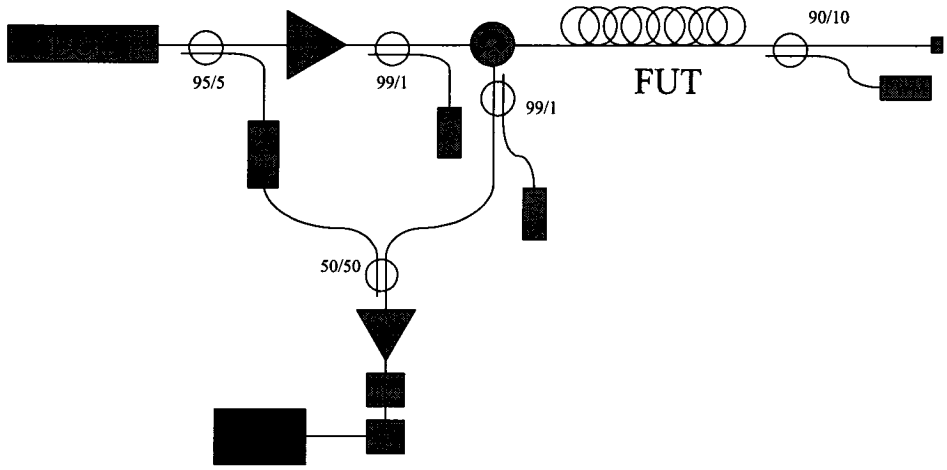

Figure III.9: Schematic of backscattered spectrum measurements with the ESA and backscattered/transmitted levels with a power meter (PWA The characteristics of the set-up and the various components are the same as in Figure III.2 except that the BOSA is replaced by the ESA and that a photo-detector (PD) has been added.

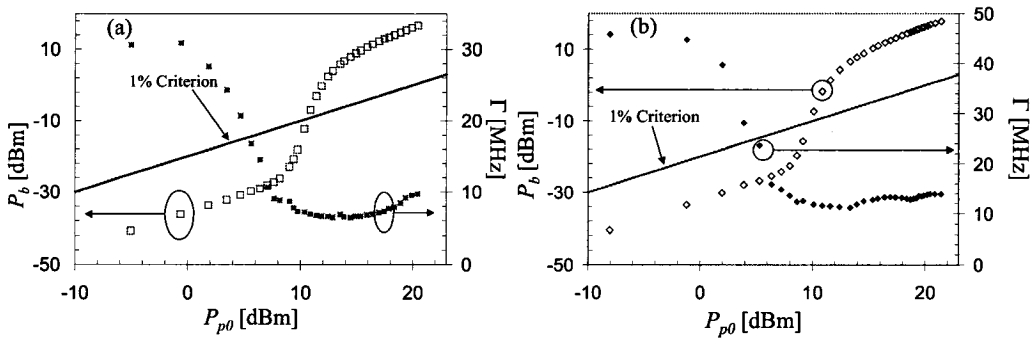

Figure III.10: (a) Backscattered power (open symbol) and Brillouin linewidth (full symbol) measurements as a function of the input power for: (a) a 20 km long SI optical fibres; (b) a 8 km long DCF.

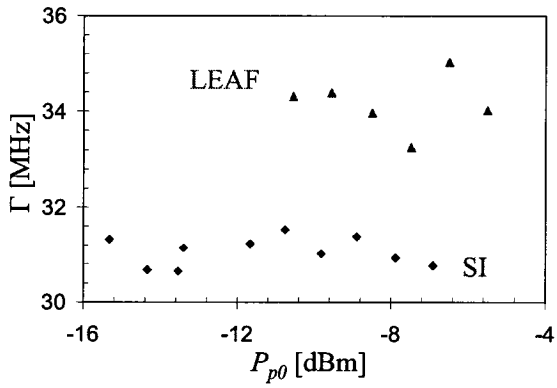

Figure III.11: Low pump input power measurements (well below threshold) of linewidth for SI (diamonds) and LEAF (triangles) types.

We systematically measured the Stokes spectrum from all the fibres for various input power. We then calculated the spectrum linewidth (Γ), defined as the distribution full width at half maximum. At the same time as spectra were acquired, we were monitoring the total backscattered power. Typical linewidth versus pump power curves for both SI (2 and 20 km) and the 8 km long DCF are presented in Figure III.10. The linewidth power dependence curves show trends in agreement with results obtained by Gaeta (1991) on short SI fibres, Esman (1996) on a 25 km long dispersion shifted fibre, and Yeniay (2002) on a large variety of long single-mode fibres. Experimental set-ups used by Esman and Yeniay are similar to ours while Gaeta recorded the Stokes spectrum with a Fabry-Perot interferometer. Three regions can be distinguished in the displayed linewidth curves:

- First, at low power (P_{p0} < 1 mW), the linewidth is constant (or experience very small variations). It is also the region where the backscattered power increases linearly with the input pump. Brillouin scattering is still in spontaneous regime and the linewidth is $\Gamma = \Delta\nu_B$.

Such stationary behaviour can not be questioned when observing Figure III.11.

- Second, following the plateau region, the linewidth drops at a rate of a few MHz per mW. That drop occurs at the same time as the backscattered power increases exponentially. Here, Brillouin scattering enters into the stimulated regime. Linewidth narrowing can be understood by considering energy conservation arguments. In fact, pump depletion being still negligible[14], the exponential rise of the backscattered intensity is only possible if the spectrum width reduces. Simulation results (Figure III.12.(a)) also confirm the trends of the experimental data as long as the SBS threshold (*1% criterion*) is not reached.

- In the third region, when the input power is larger than the threshold, the experiments show that the linewidth value becomes steady. Undepleted approximation predicts that the linewidth would narrow indefinitely as the pump power increases (Boyd 1990). In the same article, Boyd and his co-authors also developed a numerical model that explains the linewidth stationary behaviour (more rigorously, their numerical model demonstrates that the linewidth still decreases but at a much lower rate than expected in the undepleted pump approximation). Boyd's numerical model accounts for pump depletion in the three wave equations (equations (II.37)) and describes the seed Stokes wave as

[14] Below threshold, the natural fibre loss is the only visible contribution of the pump attenuation.

generated by thermal phonons acting as distributed noise sources. Our simulations (Figure III.12.(a)) fail to reproduce the linewidth curve flattening at higher power demonstrating the limit of applicability of the steady state approximation to describe the SBS generator spectral properties above threshold.

One of the main differences between Boyd's approach and our model resides in the nature of the Stokes source: in their approach, they consider a distributed noise source, while we assume that the Stokes wave is launched from the fibre opposite to the pump side (Zel'dovich 1985). The steady state approximation as we implemented then describes a Brillouin amplifier probed with a very low power and narrowband Stokes source whose frequency is tuned over a frequency centred on the Brillouin frequency. In the Brillouin amplifier configuration, the linewidth broadening can be understood as provoked by the Stokes spectrum saturation occurring when the pump depletion is not negligible anymore. .

At least, our model is reasonably good in the vicinity of the SBS threshold and below. That leads us to point out a similarity with the correspondence we found between the *1 % criterion* and the Stokes power inflexion point (Figure III.5). We propose to apply the same correspondence between the *1 % criterion* and the minimum of the linewidth curve (Figure III.12.(a)). As shown in Figure III.12.(b), the power value at the linewidth minimum compares well with the *1 % criterion.* The relative difference is a few percent as in the inflexion point method case. That minimum is then a characteristic parameter of the Brillouin process. We define it as the stimulated Brillouin scattering linewidth ($\Delta\nu_{SBS}$) measured at the SBS threshold, and, hence, by

extension the linewidth at which the pump power depletion is not negligible anymore. The SBS linewidth found for the 20 km SI fibre, and according to that definition, is $\Delta\nu_{SBS}$ = 7.02 MHz (for the simulation $\Delta\nu_{SBS}$ = 7.83 MHz). Measured spontaneous and stimulated spectrum linewidths for the various fibre types can be found in Table I. Note that we were not able to measure the spontaneous spectrum of the 2 km SI fibre, our experimental set-up being probably insufficiently sensitive for that case.

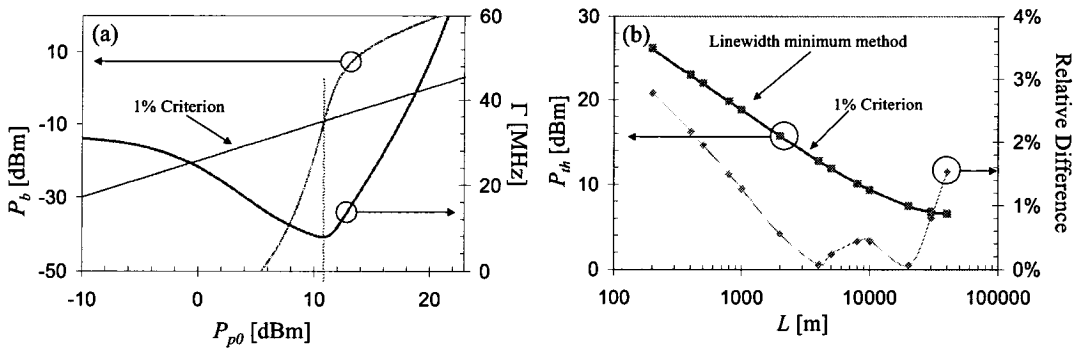

Figure III.12: (a) Stokes power (shaded curve) and Brillouin linewidth (plain curve) as a function of input pump power obtained from simulation of a 20 km SI fibre. (b) Power threshold estimated with the 1% criterion and linewidth minimum method as a function of fibre length. Parameters for the simulations are: P_{sL} = 0.66 nW, α = 0.25 dB/km, g_B = 1.12 m/W, A_{eff}=80μm^2.

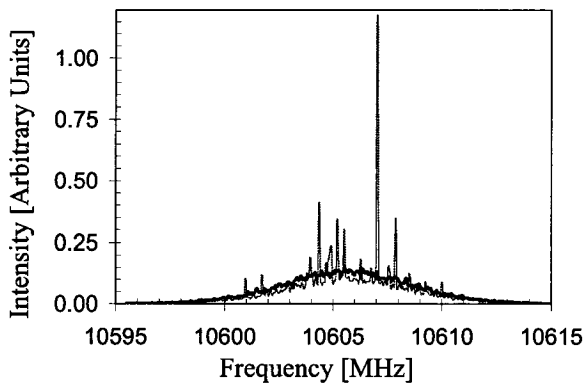

Figure III.13: Spectra measured from the 25 km LEAF near threshold (thick line, P_{p0} = 9 mW) and high above threshold (thin line, P_{p0} = 106 mW). The intensity is normalised by the total intensity of the spectrum.

If we look closely to the high power dependence of the linewidth in Figure III.10, we observe that the curve fluctuates around the estimated $\Delta\nu_{SBS}$ value. Esman (1996) and Yeniay (2002) did not mention such variation instead they insisted that the value should become steady, as their measurements suggest. The main difference with our results lies in the launched pump power. In their measurements they barely reached a pump power of 50 mW while we were able to inject up to 110 mW into the fibre. At a power much larger than the threshold, the detected spectrum appears to have strong and narrow spectral components as shown in Figure III.13, which is a behaviour not described by Boyd's numerical model and a unique observation in low loss fibres without known sources of feedback. Extreme narrowing of the spectrum was reported when feedback was induced by fibre end reflection (Dämmig 1993). The two spectra of Figure III.13 were acquired in the same conditions except for the pump power. The smooth spectrum (thick line) was measured for a pump value near threshold while the spectrum with strong spikes was taken at a power that is an order of magnitude above threshold. These narrow and intense line could be attributed to the presence of multiple beams at the Brillouin frequency that are counter-propagating. In fact, we have seen in Figure III.8.(c) that the transmitted spectrum has a line at the Brillouin frequency due to Rayleigh backscattering of the Stokes wave. That wave, in turn, can be Rayleigh scattered leading to the initiation of feedback in the fibre for frequencies near the Stokes component. Unfortunately, the narrow line is not stable in time. It disappears and appears randomly around the peak of the Stokes spectrum within a time scale less than 10 seconds. Stable narrow band emission can be achieved if the feedback is not disturbed by external sources, which is a difficult condition to achieve in long fibres. An

experimental and numerical study shows that multiple counter-propagating beams at the Stokes frequency, induced by Rayleigh scattering, lead to further linewidth narrowing when the pump power is increased (Fotiadi 1998). These authors obtained linewidth value well below 100 kHz for a short fibre (300 m) with a very high loss coefficient (17 dB/km). For such loss, the induced Rayleigh scattering is strong enough to act as a feedback source even if the fibre length is very short. Their work does not really address the long term stability of the cooperative feedback as only time scales of the order of 10 μs are displayed. Stable narrow band Stokes spectrum can be achieved when the feedback is controlled such as in a fibre laser (Dämmig 1993, Debut 2000, Debut 2001). From this discussion, we conclude that at high power, and, if the fibre does not experience externally induced feedback, the linewidth will reach a plateau value that is only an average estimate. The actual value can fluctuate around it.

Table III.1: Parameters and measured characteristics of the various fibres studied. A_{eff} data are nominal values provided by the fibre manufacturer

Fibre Type	SI	SI	LEAF	DCF	DCF
L [km]	20	2	25	8	3.5
A_{eff} [μm^2]	80	80	72	15	21
ν_B [MHz]	10874	10846	10646	9854	9870
P_{th} [mW]	11	52	9	10	18
$\Delta\nu_B$ [MHz]	31	-	35	46	47
$\Delta\nu_{SBS}$ [MHz]	7	10	11	12	10

The various measurement results summarised in Table III.1 indicate a significant variation of the Brillouin frequency shift with the fibre type. These differences are not a surprise and can be qualitatively explained by simple arguments supported by the scientific literature. From relation (II.19), we know that the Brillouin frequency shift is

proportional to the core refractive index and the acoustic mode velocity, which are both influenced by the dopant used to create the waveguide (Shibata 1987, Shibata 1988, Jen 1988, Shibata 1989). A systematic characterisation of the Brillouin gain has shown that the Brillouin frequency decreases with the dopant concentration, which was in this case GeO_2 (Niklés 1997). In this same study, it is observed that the spontaneous linewidth rises with an increased concentration of GeO_2. The cause of the linewidth broadening is a stronger attenuation of the acoustic wave. Thomas (1979), Shibata (1989) and Jen (1988) mention that the quantitative difference between bulk silica and optical fibres can only be explained by the guided nature of the acoustic modes. Jen (1985, 1988) states that the optical fibre acts as a waveguide for both optical and acoustic modes. Besides, if a fibre supports only one optical mode, it can allow the propagation of various acoustic modes depending on the waveguide structure. The ability of the waveguide to carry multiple acoustic modes leads to the existence of multiple peaks in the Brillouin spectrum (Jen 1988, Shibata 1988, 1989). A spectrum with multiple peaks, measured with our set-up, is shown in Figure III.14 for LEAF type. Starting from the fibre core structure, and, hence, its doping concentration, some authors have reconstructed the measured gain spectrum by simulation (Koyamada 2005, Mc Curdy 2006).

Our spectrum measurements have revealed that LEAF has four peaks as shown in Figure III.14. The highest peak (peak 1) is associated with the scattering of the pump by the fundamental longitudinal mode. The other peaks come from the scattering of the pump by higher order longitudinal guided modes that are supported by LEAF type (Jen 1988, Shibata 1988, Shibata 1989). The first peak intensity is larger because the optical mode overlaps the fundamental acoustic mode more completely than it does with the

other acoustic modes i.e. the interaction giving birth to the first peak is stronger than the interaction leading to the satellite peaks (Thomas 1979, Jen 1988, Shibata 1988, Shibata 1989, McCurdy 2006). Table II presents LEAF characteristics in spontaneous regime, obtained experimentally, which are the Brillouin frequencies, the Brillouin linewidth and the relative peak power (*RPP*) of each line. The relative peak power is defined as the ratio of the peak power to the main peak power. The simulation result, based on equations (II.46), is a phenomenological reconstruction of the gain curve from the data of Table III.2 (Brillouin frequencies and *RPP*).

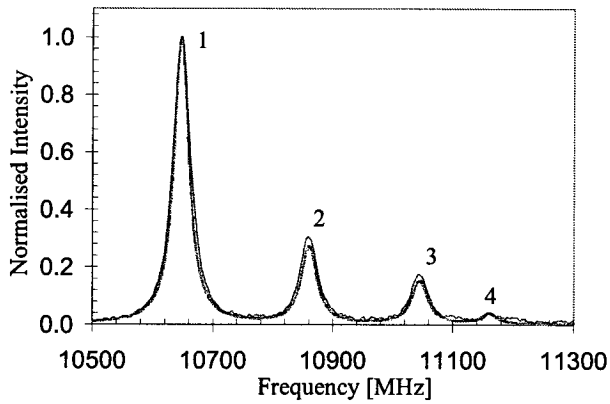

Figure III.14: Stokes spectrum measured (plain curve) form the 25 km long LEAF in spontaneous regimes (P_{p0} = 305 μW). The numbers on the figure identify the various peaks observed. Shaded curve shows the simulated spectrum for the same fibre with the following parameters: P_{sL} = 0.66 nW, α = 0.25 dB/km, g_B = 1.12 m/W, A_{eff}=72μm^2.

Table III.2: Measured spectral characteristics of LEAF in spontaneous regime.

Peak	1	2	3	4
ν_B [MHz]	10646	10860	11044	11160
RPP	1.00	0.30	0.18	0.04
$\Delta\nu_B$ [MHz]	35	36	36.5	56

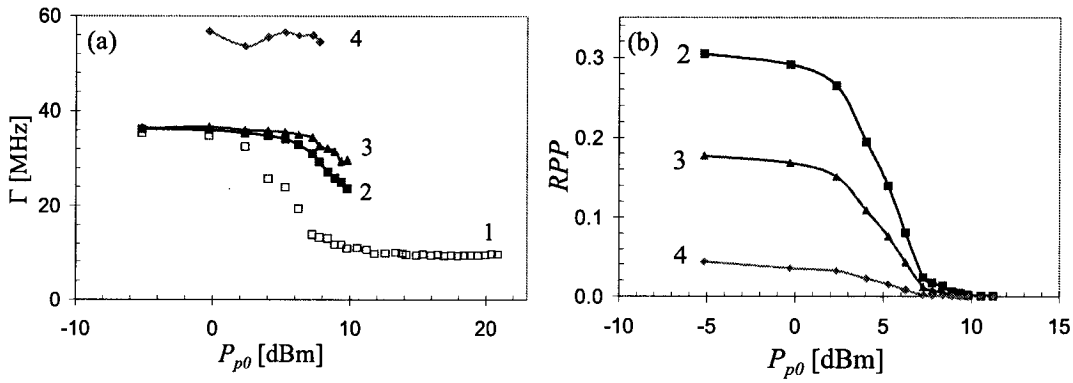

Figure III.15: (a) Brillouin linewidths of the various peaks as a function of input pump power measured from the 25 km long LEAF. (b) Relative peak power (RPP) of the various peaks in the Stokes spectrum measured for the 25 km long LEAF. The reference power is the first peak (main peak).

We also studied the input pump power dependence of the LEAF spectrum. The data are displayed in Figure III.15. The linewidth of the main peak evolves similarly to the results obtained for the SI and DCF type fibres (Figure III.15.(a)). The linewidth of peaks 2 and 3 decreases slowly, and then drops abruptly. As shown in Figure III.15.(b), their respective *RPP* also decreases significantly until the peak becomes undetectable above 10 mW. No linewidth data are reported at power higher than the threshold because their *RPP* is two orders of magnitude lower than the main peak, which reduces the signal-to-noise of each measured peak below 3 dB. The fourth peak linewidth behaviour can only be observed over a smaller input power range for the same reason. The simulations presented in Figure III.16 show a qualitative agreement with the experimental curves, at least below threshold. We believe that the *RPP* decrease and the ultimate disappearance of peaks 2 to 4 can be explained by the fact that the main peak enters into stimulated regime before the other peaks do. The main peak output power then increases exponentially. Ultimately, the main peak has strongly depleted the pump leaving too little power to the other peaks to significantly contribute to the electrostrictive process, and, hence to the growth of their power.

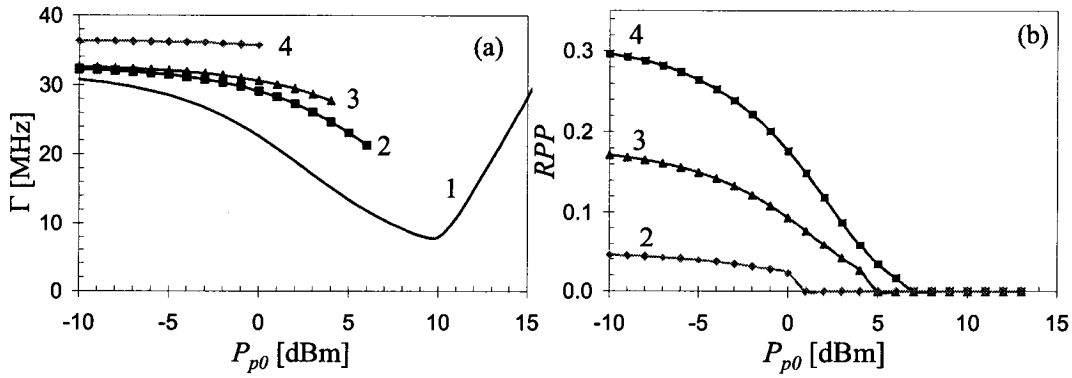

Figure III.16: (a) Brillouin linewidths of the various peaks as a function of input pump power simulated for the 25 km long LEAF. (b) Relative peak power (RPP) of the various peaks in the Stokes spectrum simulated for the 25 km long LEAF. Parameters for the simulations are: P_{sL} = 0.66 nW, α = 0.25 dB/km, g_B = 1.12 m/W, A_{eff}=72μm^2.

III.C.Brillouin fibre amplifier

III.C.1. General configuration and characteristics

In the Brillouin generator, the Stokes wave is initiated with the scattering of the pump by thermal phonons: only one lightwave, the pump, is launched into the fibre. To the contrary, the Brillouin fibre amplifier (BFA) requires that a Stokes wave to be injected at the opposite end of the fibre as illustrated in Figure III.17 (Olsson 1986, Tkach 1989, Ferreira 1994). The two counter-propagating lightwaves are coupled through electrostriction, which leads to the amplification of the Stokes[15] at the expense of the pump. Even if the Stokes power is in the range of tens of nW, the thermally generated scattering is a small contribution to Brillouin interaction and equations (II.46) of Chapter II describes accurately the physics of the Brillouin amplifier (Tang 1966). That applicability remains true for the spectrum characterisation as long as the amplified spontaneous emission remains small (Ferreira 1994).

[15] In the BFA configuration, it happens that the Stokes wave is also called probe or signal.

According to equation (II.43) from Chapter II, the BFA can be characterised by gain (G_s) and loss (G_p) intensity coefficients. The coefficients can be expressed as a function of the detuning frequency $\Delta\nu$ and position as

$$G_s(0,\Delta\nu) = \ln\left[\frac{P_s(0,\Delta\nu)}{P_{sL}}\right], \tag{III.1.a}$$

$$G_p(L,\Delta\nu) = \ln\left[\frac{P_p(L,\Delta\nu)}{P_{p0}}\right], \tag{III.1.b}$$

where P_{p0} and $P_p(L,\Delta\nu)$ are input and output pump power respectively, while $P_s(0,\Delta\nu)$ and P_{sL} are output and input Stokes power respectively. From Figures II.8 and II.9, we know that the gain reaches its peak value ($G_s(0,0)$) and its largest loss ($G_p(L,0)$) when $\Delta\nu = 0$.

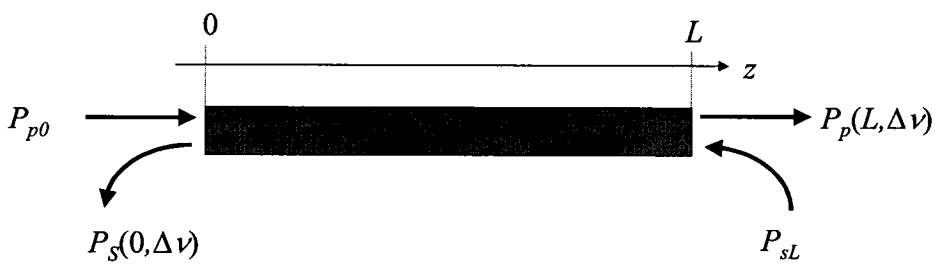

Figure III.17: Schematic of the Brillouin amplifier configuration. P_{p0} and $P_p(L,\Delta\nu)$ are input and output pump power respectively, while $P_s(0,\Delta\nu)$ and P_{sL} are output and input Stokes power respectively.

Typical gain peak and maximum loss as a function of input Stokes power are presented in Figure III.18. The gain curve (Figure III.18.(a)) is characterised by two regions. At low input Stokes power, the gain is large and constant. That is known as the small signal gain region, which is a characteristic of any amplifier (Siegman, 1986 Agrawal 1997). In the second region, the gain drops as the Stokes input power rises. In that regime, the amplifier is said to be saturated. The gain saturation effect can be

associated with pump depletion. A strong input Stokes power enhances electrostriction which in turn contributes to increase the scattering of the pump. That induces significant pump depletion (Figure III.18.(b)). As the pump becomes depleted near $\Delta\nu = 0$, the available energy in the pump for the Stokes amplification drops. Instead, for $\Delta\nu \neq 0$, the depletion has not taken effect yet. The amplitude of the tails of the gain spectrum then increase and brings linewidth broadening as shown in Figure III.18.(a). A similar linewidth broadening due to the input Stokes power increase was experimentally evidenced (Niklès 1997). The linewidth (Γ_n) represented in Figure III.18.(a) is normalised and defined as the ratio of the actual linewidth Γ to the small signal gain linewidth.

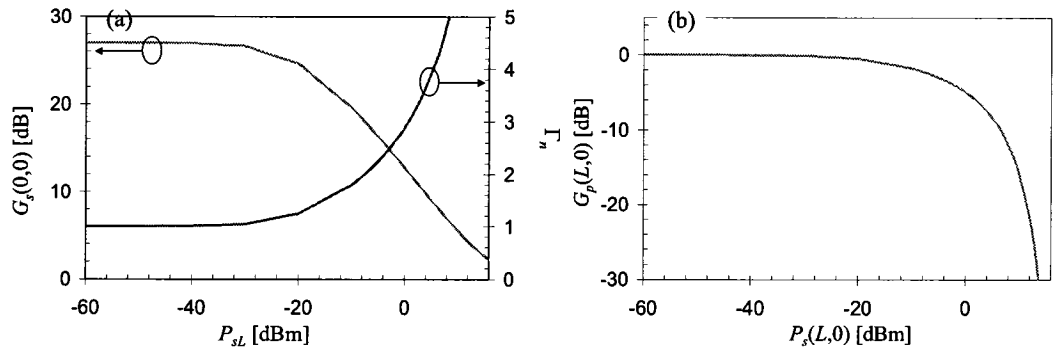

Figure III.18: (a) Stokes spectrum peak gain and normalised linewidth as a function of input Stokes power. (b) Maximum pump loss as a function of input Stokes power. Parameters for the simulations are: L = 2km, P_{p0} = 24 mW, α = 0.25 dB/km, g_B = 1.12 m/W, A_{eff} = 80 μm^2.

III.C.2. Power threshold in a Brillouin fibre amplifier

As for the Brillouin generator, we can draw the output Stokes power and linewidth as a function of the input pump power as represented in Figure III.19. We see that for both input Stokes power cases, P_{sL} = 0.66 nW and P_{sL} = 1 μW, identical output Stokes power regimes can be observed and were demonstrated previously by others for

the Brillouin amplifier case (Tang 1966, Ferreira 1994). Ferreira has shown that the linewidth passes through a minimum but, if the power is further increased, it reaches a plateau region. He attributed this linewidth flattening to the degradation of the Stokes output signal by amplified spontaneous emission. The difference with our approach lies in the fact that, in our model, we do not account for the generation and the amplification of distributed spontaneous Stokes photons. In our case, the only contribution to the spectrum shape is determined by the Stokes gain saturation.

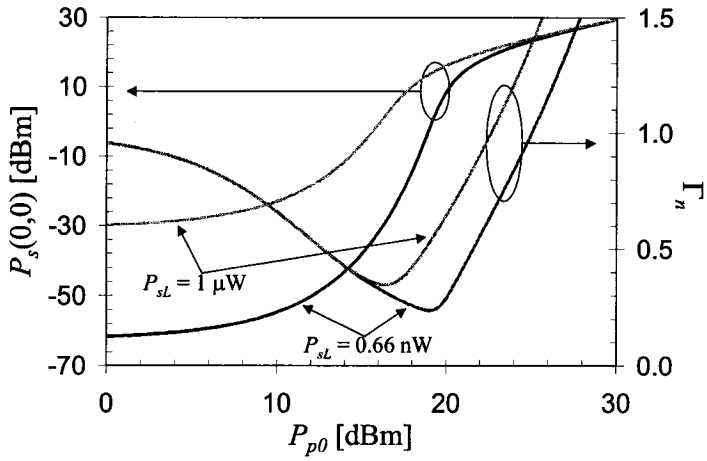

Figure III.19: Stokes peak power and normalised linewidth as a function of input pump power for $P_s(L)$ = 0.66 nW (plain curves) and $P_s(L)$ = 1 μW (shaded curves). Parameters for the simulations are: L = 2000 m, α = 0.25 dB/km, g_B = 1.12 m/W, A_{eff} = 80 μm^2.

From Figure III.19, it is clear that both Stokes linewidth and power curves are shifted to the upper left corner of the graphic as the input Stokes increase. That makes the use of the 1% criterion unoperational for the determination of the threshold in a Brillouin amplifier. Hopefully, the methods we introduced in the previous sections can still be used as the inflexion point of the power and the minimum of the linewidth are accompanying the curves shift with the input Stokes power rise. Figure III.19 then

shows that the threshold is decreased when the Stokes power is increased and that our new criterion definitions are still applicable in BFA cases.

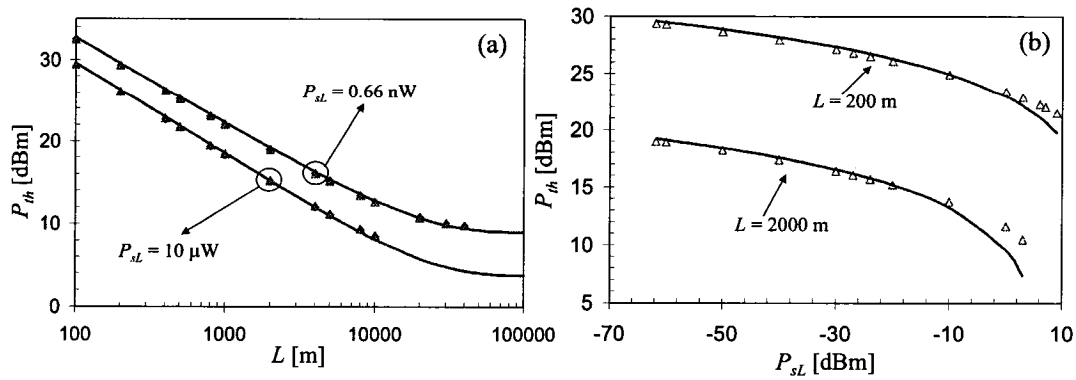

Figure III.20: (a) Power thresholds, theoretical model (plain curve), inflexion method (full diamonds) and open triangles (linewidth minimum), as a function of fibre length for P_{sL} = 0.66 nW and P_{sL} = 1 μW. (b) Power thresholds, theoretical model (plain curve) and open triangles (linewidth minimum), as a function of input Stokes power for L = 200 m and L = 2000 m. Parameters for the simulations are: α = 0.25 dB/km, g_B = 1.12 m/W, A_{eff} = 80 μm^2.

At the present stage, and, to the best of our knowledge, there are no mathematical expressions relating the threshold to the input Stokes power in a BFA without feedback. Such threshold definition is certainly useful for distributed sensing applications where the depletion effect needs to remain moderate to achieve optimum sensing operation. A power threshold definition would then set an upper limit to the input powers into the fibre. We propose to address that lack by considering the same argument as Smith (1972) which is that the threshold is the input pump such that the output Stokes is equal to the input pump. That criterion, applied to the undepleted pump approximation (equation (II.50)), leads to the following equality

$$f(x) = x - I_{sL} \exp\left[\chi_{SBS} g_B x L_{eff}\right] \tag{III.2}$$

The root of that equation is the threshold we want to find. Equation (III.2) must be solved numerically and that can be done by the Newton-Raphson method (Abramowitz 1964, Press 1999). Newton-Raphson method is based on a Taylor expansion of f near its zero:

$$f(x+\delta) \approx f(x) + f'(x)\delta + \frac{f''(x)}{2}\delta^2 + \ldots \tag{III.3}$$

When $|\delta| << 1$, which happens for $f(x+\delta)$ is very close to zero, higher order terms can be neglected. We can then write that

$$\left|\frac{f(x)}{\delta}\right| \approx |f'(x)| < \eta \qquad 0 < \eta < +\infty \tag{III.4}$$

The condition on η is imposed by the fact that the first and second order derivatives of f have to be defined. Calculating explicitly f' and using the argument that η is a finite number, we find that the power threshold is bounded as follows

$$\frac{A_{eff}}{\chi_{SBS} g_B L_{eff}} \ln\left[\frac{(1-\eta)A_{eff}}{P_{sL}\chi_{SBS} g_B L_{eff}}\right] < P_{th} < \frac{A_{eff}}{\chi_{SBS} g_B L_{eff}} \ln\left[\frac{(1+\eta)A_{eff}}{P_{sL}\chi_{SBS} g_B L_{eff}}\right]. \tag{III.5}$$

Additionally, equation (III.5) imposes that $\eta < 1$. We can then express the threshold as

$$P_{th} = \frac{A_{eff}}{\chi_{SBS} g_B L_{eff}} \ln\left[\frac{\zeta A_{eff}}{P_{sL}\chi_{SBS} g_B L_{eff}}\right] \qquad 1-\eta < \zeta < 1+\eta \tag{III.6}$$

We found that $\zeta = 0.9205$ by fitting equation (III.6) to the data of Figures III.4.(a), III.5 and III.12.(a). The root-mean-square deviation of the relative error is better than 0.5 %. Figure III.20 illustrates the analytical power threshold definition behaviour with fibre length and input Stokes power. It also shows the comparison with both inflexion and

linewidth minimum methods. As it appears in Figure III.20.(a), the agreement is good. Excepted at Stokes power larger than 1 mW, the match is satisfactory too when the threshold dependence against Stokes power is considered. The discrepancy at higher power can be attributed to the fact that depletion cannot be neglected.

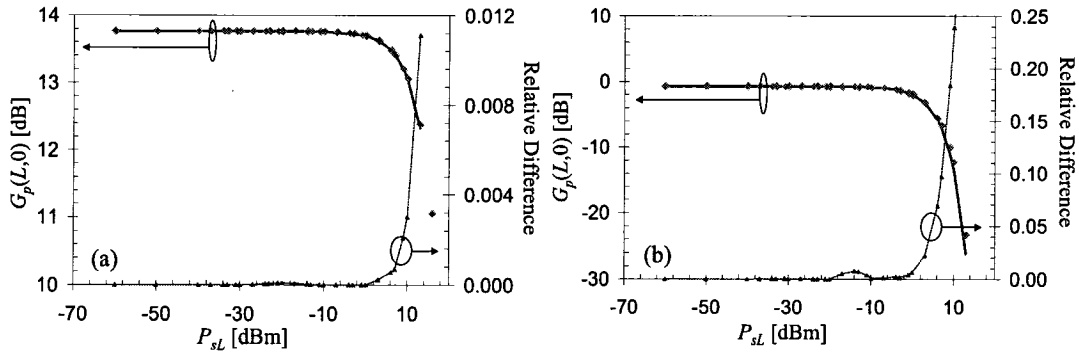

Figure III.21: Maximum pump loss, weakly depleted model (plain curve) and numerical simulation (full diamonds), as a function of input Stokes power for (a) L = 100 m and P_{p0} = 24 mW, (b) L = 2000 m and P_{p0} = 1 mW. Other parameters for the simulations are: α = 0.25 dB/km, g_B = 1.12 m/W, A_{eff} = 80 μm^2.

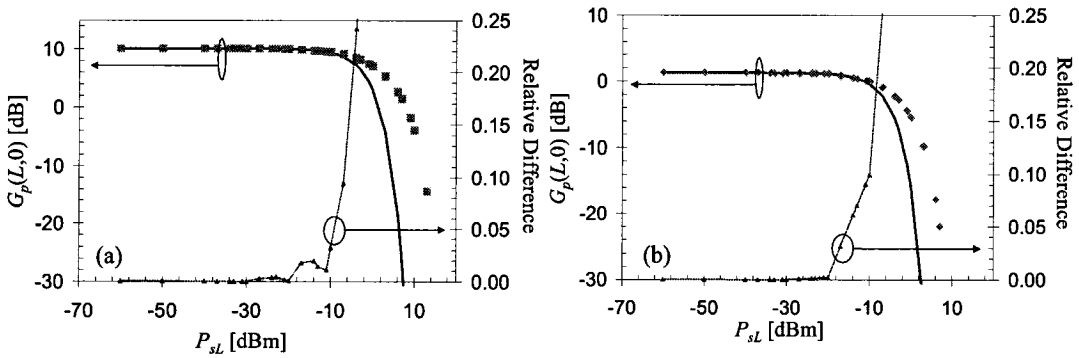

Figure III.22: Maximum pump loss, weakly depleted model (plain curve) and numerical simulation (full diamonds), as a function of input Stokes power for (a) L = 2000 m and P_{p0} = 12 mW, (b) L = 10000 m and P_{p0} = 1 mW. Parameters for the simulations are: α = 0.25 dB/km, g_B = 1.12 m/W, A_{eff} = 80 μm^2.

III.C.3. Limitation of weakly depleted approximation

Since we introduced the weakly depleted approach in section II.C.5, we did not discuss the validity of the moderate pump depletion approximation, which has given relation (II.51), an analytical expression, which is always simpler to implement than the numerical solutions of equations (II.46). Figure III.21 shows the comparison of the pump loss calculated with equation (II.51) and the pump loss obtained by computation of relations (II.46). For L = 100 m, the error of estimating the Brillouin loss with the moderate depletion approximation is negligible, even at pump and Stokes powers in the tens mW range. In the case of a 2 km long fibre, the disagreement is still below 10% if Stokes and pump power are about 1 mW. A 10 % error can still be achieved for higher pump power of the 2 km long case but the Stokes power launched into the fibre then need to be reduced by 10 dB at least (Figure III.22.(a)). The same kind of error is possible on a longer fibre (L = 10 km) for similar Stokes levels at the only condition that the pump power is decreased too (Figure III.22.(b)). The condition for applicability of relation (II.51), for any Stokes or pump power, requires then that the fibre is short, or, by extension, that the interaction length is about a hundred meters long maximum. If BFA configurations with longer fibre as well as larger pump or Stokes power need to be studied with equation (II.51), we can consider that the power threshold given by expression (III.6) sets the upper limit of validity of the moderate depletion approximation.

III.D.Summary

The steady state approximation introduced in Chapter II is a good model to describe the power behaviour of the Brillouin generator for any fibre length and pump

power. The model is also a good tool to study the backscattered spectrum behaviour, at least for pump powers lower than the Brillouin threshold. At higher power, the model should account for the distributed nature of the Stokes wave generation as well as the unwanted feedback generated by multiple Rayleigh scattering of the Stokes wave.

The Brillouin threshold, for both BFG and BFA, is the maximum input pump power below which the output pump is weakly depleted. It is a function of fibre length, fibre characteristics and, specifically for the BFA, input Stokes power. Once the threshold is crossed, the Stokes power exponential growth converts into a linear rise, while the Stokes linewidth stops to decrease and starts to saturate or to broaden. Below the threshold, the moderately depleted model for pump power describes the Brillouin loss with a good accuracy.

Chapter IV: The Brillouin sensor

IV.A. Introduction

We have seen that the Brillouin frequency shift is a characteristic of the material in which the scattering occurs. Brillouin scattering has been used to probe an optical fibre and extract informations about its structure and its composition (Shibata 1987, Shibata 1988, Shibata 1989, Niklès 1997, Yeniay 2002, Yu 2003, Zou 2003, Koyamada 2004, McCurdy 2005, Shibata 2006). The Brillouin frequency shift being material dependant and associated with density fluctuations of the medium, it is natural to consider that it can be influenced by environmental perturbations such as temperature variations or mechanical stresses (Culverhouse 1989, Horiguchi 1989).

The present chapter is a review section about Brillouin scattering as mechanism for temperature and strain sensing (sections IV.B and IV.C). The Brillouin frequency relationship with strain and temperature will be presented. We will then discuss specifically the distributed Brillouin sensor (DBS) developed at the University of Ottawa. The parameters describing the sensor performance will be introduced. These are the spatial resolution, the frequency resolution and the dynamic range. Although these sections do not bring new features to the works done at the University of Ottawa on the DBS (and to the field in general), we believe that this reviewing task is necessary because it introduces what we need to develop a simple model of the sensor operation as presented at the end of this chapter (Ravet 2006c).

In section IV.D, we qualitatively discuss the sensor settings and configuration related to the measurement performance. Through an original study, grounded on the

results of Chapters II and III, we investigate the effect of optical power, fibre length and position on Brillouin spectrum and we see how this is affecting frequency and spatial resolution as well as the dynamic range (Ravet 2006a).

Section IV.E, which is an original work too, is dedicated to the development of the phenomenological model, a simple mathematical model simulating the DBS (Ravet 2006c). The model integrates the various elements of the DBS such that it can predict the sensing operation with accuracy without requiring complicated calculations or lengthy computation times. That approach can be used to study sensing configurations and hence optimise the sensing fibre layout. If the approach is simple and easy to implement, it can also be employed in a signal processing scheme taking into account the sensor parameters as it will be discussed in Chapter V.

IV.B. Distributed Brillouin sensor description

IV.B.1. Brillouin frequency relationship with strain and temperature

The Brillouin effect is the scattering of a lightwave by an acoustic wave. In other words, it is the scattering of the lightwave by a periodic variation of the density of the medium. The scattered beam optical frequency experiences a shift equals to ν_B. According to Equation (II.19), the Brillouin frequency is proportional to the refractive index of the fibre (n) and to the acoustics wave velocity (V_A). Any temperature or mechanical stress would change the density of medium, and, in consequence, both n and V_A.

According to Bucaro, the acoustic velocity in fused silica varies by about 7% when the temperature is increased from 20 to 1620°C (Bucaro 1974). That change is a

negligible contribution when compared to the variation induced by the refractive index temperature dependence (Li 1980). The temperature variation relates to the Brillouin frequency as (Horiguchi 1995)

$$\nu_B(T) = \nu_B(T_r)\left[1 + C_T(T - T_r)\right], \tag{IV.1}$$

where T is the temperature and T_r is the reference temperature. A typical value for the temperature coefficient C_T is 1.361 MHz/°C. Culverhouse demonstrated the feasibility of a temperature sensor based on the mechanism of Brillouin scattering (Culverhouse 1989). Kurashima has raised an important issue related to the structure of the optical fibre (Kurashima 1990): the temperature variation induces a stress at the cladding-coating interface that affects the Brillouin frequency shift. That effect is negligible when the waveguide is coated with acrylate (Kurashima 1990, Niklès 1997).

When considering the influence of a mechanical stress on the optical fibre, both n and V_A need to be taken into account. The refractive index is changed through the elasto-optic effect which is mathematically described by the elasto-optic tensor. The optical fibre being an isotropic material, the refractive index change (δn) reduces to

$$\delta n = -\frac{n^2}{2}\left[p_{12} - \kappa_p(p_{11} + p_{12})\right], \tag{IV.2}$$

where p_{11} and p_{12} are the elasto-optics coefficients, κ_p is the Poisson's ratio (Butter 1978, Bertholds 1988, Horiguchi 1989). The acoustic velocity is expressed as

$$V_A = \sqrt{\frac{K(1-\kappa_p)}{(1+\kappa_p)(1-2\kappa_p)\rho}}, \tag{IV.3}$$

where K is the Young's modulus and ρ is the material density (Landau 1967a). The acoustic velocity variation not only depends on the material density change but also on the both K and κ_p due to the non-linear nature of the silica response to a mechanical stress (Mallinder 1964). All these effects contribute to the strain proportionality coefficient C_ε that relates the Brillouin frequency variation to the tensile strain[16] (ε'), when temperature remains unchanged, as (Horiguchi 1995)

$$\nu_B(\varepsilon') = \nu_B(0)\left[1 + C_\varepsilon \varepsilon'\right] \tag{IV.4}$$

A typical value for C_ε is 0.0660 MHz/με.

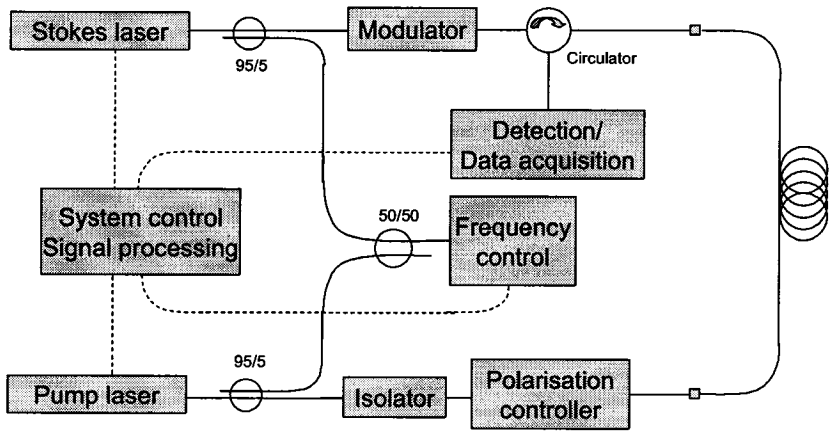

Figure IV.1:

Figure IV.1: Schematic of the distributed Brillouin sensor.

IV.B.2. Distributed Brillouin sensor set-up

In all the practical cases discussed in the present thesis, the sensing medium of the DBS is a standard single-mode fibre (ITU G.652). Two laser beams are injected into this fibre in a counter-propagating configuration (Figure IV.1). Figure IV.1 is actually a schematic of principle of the distributed Brillouin sensor (DBS). An enhanced

[16] Tensile strain is defined as the ratio of the length increase δl to the gauge length l. It is a relative quantity that can be expressed in percents or in με (microstrains) which a thousandth of a percent.

interaction between the two beams happens when the frequency difference of the two lasers matches the frequency of the longitudinal acoustic phonons of the optical fibre. There is then a transfer of energy from the high frequency beam (pump) to the low frequency beam (probe). The amount of loss of the pump is recorded at one end of the fibre as a function of the frequency difference in the form of Brillouin spectrum. The maximum loss occurs at the Brillouin frequency (ν_B), which is the phonon frequency. The sensor description is based on Brown (2000) and DeMerchant (2000) thesis.

The distributed nature of the sensor is achieved by intensity modulating the probe beam. An electro-optic modulator (EOM) creates an optical pulse whose duration is $\Delta\tau$. The pulse propagates through the fibre and interacts with the pump. The pump power (and then the Brillouin loss) variation with time is measured by a photodiode at the pulse input, giving a waveform that can be converted into a spatial profile (Figure IV.2).

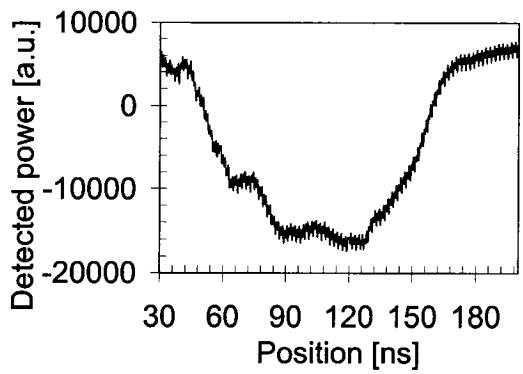

Figure IV.2: Waveform of a 10m long loose fibre measured at a beat frequency of 12800 MHz ($\Delta\tau$=2 ns).

The measurement procedure is based on the acquisition of the spectrum of the pump at the output of the fibre. The Brillouin frequency being extracted from the

spectrum, the detection requires that the optical frequencies of the two lasers be controlled accurately. The frequency control block is designed to perform three actions:

1. Measurement of the frequency of the beat signal of the two lasers;

2. Locking the frequency of the beat signal of the two lasers during the acquisition of a waveform;

3. Stepping up (or down) the frequency once the waveform is recorded.

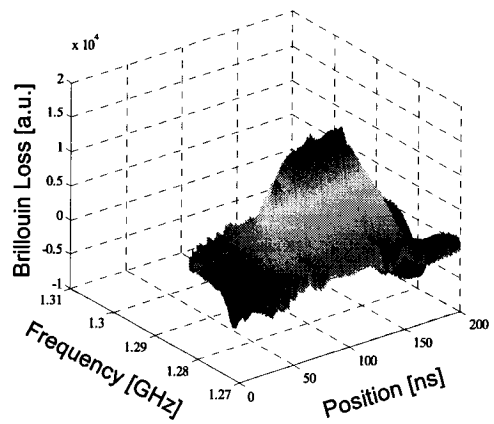

Figure IV.3: Spectrum distribution of a 10 m long loose fibre (same fibre and conditions as for the waveform shown in Figure IV.2).

The design of the frequency control unit is determined by the characteristics of the two lasers and the target performance of the sensor. A temperature resolution better than 1°C or a strain resolution better than 15 με require a beat frequency stability much lower than 500kHz over the measurement time. For instance, narrow band sources such as Nd:YAG lasers (linewidth<5kHz) have a long-term frequency stability of about 50 MHz/hour. That drift is unacceptable for sensing applications. The frequency control unit then measures the frequency, detects any change by using a phase locked loop circuit. The detected change is sent to the signal control unit, which, in turn, modifies

the laser cavity length to correct the frequency. With such frequency constraints on the sources and the frequency control unit, the frequency resolution is limited by the Brillouin linewidth only (Horiguchi 1995). Combining both time and frequency domain measurements give a three dimensional picture of the detected pump power spectrum (Figure IV.3). The accurate Brillouin frequency determination from a local spectrum is made by fitting a Lorentzian distribution, an extremum search routine or more elaborate techniques (as discussed in Chapter V).

The polarisation controller is an indispensable device. The Brillouin interaction is strongly polarisation dependent. When Stokes and pump fields are aligned, the energy transfer is maximum while it is negligible when the two fields are orthogonal. Due to birefringence and polarisation mode coupling, both polarisation states vary along the fibre. The waveforms then experience large amplitude variation as a function of position than could be misinterpreted as stress induced. Moreover, the spectrum Signal-to-Noise Ratio (SNR) from one location to another would change dramatically: large and poor SNR would alternate degrading the Brillouin frequency detection. By measuring systematically two waveforms obtained with two input pump fields orthogonally polarised, and, by computing the average waveform, these polarisation dependent effects can be minimised.

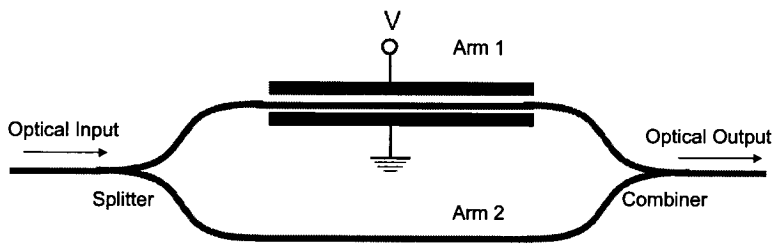

Figure IV.4: Schematic of an electro-optic modulator based on the Mach-Zehnder interferometer configuration.

IV.B.3. Electro-optic modulator and pulse characteristics

The EOM implemented in the DBS is a Mach-Zehnder interferometer in which at least one of the two arms has electro-optic properties (Li 2003). A schematic is shown in Figure IV.4. The electro-optic sensitive arm is made of $LiNbO_3$ which is a crystal whose refractive index changes linearly when an electric field is applied.

Let us now detail the working principle of the EOM. A *cw* laser lightwave enters into the device and is separated spatially by the splitter. Both waves propagate along the two arms and recombine before exiting the EOM. The propagation in the two arms induces a phase difference such that the recombination leads to interferences. The phase difference, and hence the interferences, can be controlled by applying a voltage to the electro-optic sensitive arm. The output intensity is maximum when the two fields are in phase while it becomes minimum when the fields are 180° out of phase. The output intensity I_{out} can be expressed as

$$I_{out} = \frac{1}{2}\left[I_1 + I_2 + 2\sqrt{I_1 I_2}\cos(\phi_1 - \phi_2)\right], \tag{IV.5}$$

where I_1, ϕ_1, I_2, ϕ_2 are the optical intensities and phases when the lightwaves exit the two arms and recombine. If the input has no excess loss, the input intensity is $I_{in}=I_1+I_2$ and the modulator transfer function is given by

$$T_{EOM} = \frac{I_{out}}{I_{in}} = \frac{1}{2}\left[1 + b\cos(\phi_1 - \phi_2)\right], \tag{IV.6}$$

where

$$b = \frac{2\sqrt{I_1 I_2}}{I_1 + I_2}, \tag{IV.7}$$

which is in practice different from unity due to the splitter power imbalance. The phase difference can be expressed as

$$\phi_1 - \phi_2 = \phi_0 + \Delta\phi_V = \phi_0 + \pi\frac{V}{V_\pi} \tag{IV.8}$$

ϕ_0 is the phase when no voltage is applied due to optical path difference between the two arms, V is the voltage applied that would change the phase by $\Delta\phi_V$ and V_π is the voltage that would provoke a phase shift of π. V_π is the parameter that characterises the electro-optic medium of the modulator. A schematic of an EOM transfer function curve is shown in Figure IV.5.

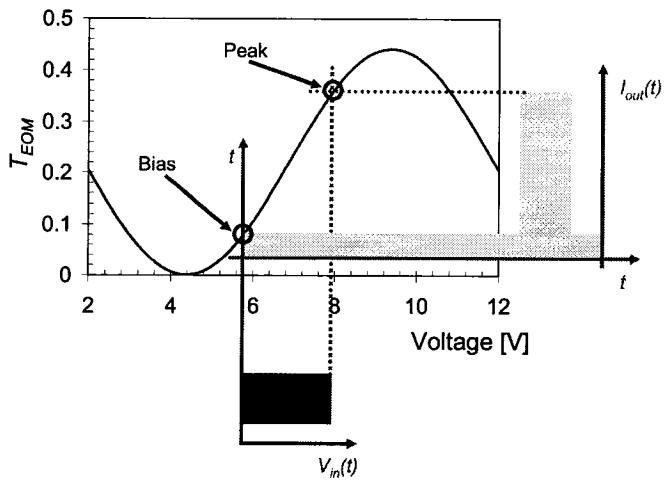

Figure IV.5: Characteristic curve of an EOM transfer function. The effect of the arms optical path length difference and power splitter imbalance is shown (V_π=5 V, A_1/A_2=1.1). The conversion from an electrical to an optical pulse is also illustrated. This figure emphasises the combined effect of EOM technological weaknesses and pulse generation.

Figure IV.5 also show how a pulse can be created when a time varying signal is applied to the electro-optic sensitive arm. Pulse distortions are minimised when the

EOM is biased to limit the excursion of the time dependent voltage in the linear region of the transfer function. The EOM bias has the effect to generate pulses composed of AC (time dependent) and DC (*cw*) parts. That effect leads us to introduce the pulse extinction ratio

$$ER = 10\log\left(\frac{I_{\max}}{I_{\min}}\right). \tag{IV.9}$$

I_{max} and I_{min} are the optical pulse maximum and minimum intensities, respectively. For example, the largest extinction ratio that can be achieved with the EOM whose transfer function is shown in Figure IV.5 is 25.4 dB.

IV.B.4. Receiver

The conversion from optical to electrical signal is achieved by a receiver block constituted of a p-i-n photodiode and a large gain electrical amplifier stage. The photodiode performance is characterised by the signal-to-noise electrical power ratio (SNR_e) defined as (Agrawal 1997)

$$SNR_e = \frac{I_p^2}{\sigma_s^2 + \sigma_T^2} = \frac{(RP_{in})^2}{\sigma_s^2 + \sigma_T^2}, \tag{IV.10}$$

where I_p is the photocurrent proportional to the input light average intensity (P_{in}), σ_s and σ_T are shot and thermal noises respectively, R is the photodiode responsivity. The shot noise term is proportional to P_{in} and can be neglected for low optical levels. The *SNR* photodiode is also limited by the bandwidth (Δf) of the device. In fact, the *SNR* is inversely proportional to the device bandwidth. In thermal noise limited photodiodes, it is convenient to introduce the noise equivalent power (*NEP*) defined as $P_d/\Delta f$, P_d being

the minimum detectable optical power that produces a SNR_e equals to unity. As we will see in section IV.C, the SNR affects significantly the frequency resolution and impacts the sensing operation. The targeted frequency resolution will determine the lowest optical input level.

There is also an upper limit to the receiver input power. There is an optical power threshold that should not be reached as the generated current becomes so high that it can provoke a permanent damage to the junction.

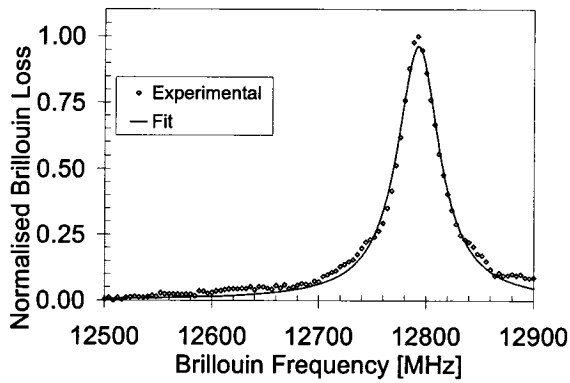

Figure IV.6: Example of spectrum measured at a one position of a 30 m long loose fibre with a 1.5 ns pulse. The plain curve is the result of a Lorentzian fit on the experimental spectrum. The curve fitting routine uses the Levenberg-Marquardt algorithm (Press 1999). It gives a Brillouin frequency of 12792.56MHz and a FWHM of 48.09MHz with R^2=0.9954[17].

IV.C. Performance parameters

IV.C.1. Spatial resolution

After Beller, "spatial resolution indicates instrument ability to resolve two adjacent events" (in Derickson 1998). In the case of the Brillouin sensor, the spatial

[17] R^2 is the determination coefficient and indicates the percentage of the measured data that are well modeled by the fitted mathematical curve (here a Lorentzian distribution). R^2 = 1 means that 100 % of the data points are matching exactly the mathematical curve. See also Equation (V.4) in section V.C.1.

resolution is the ability of the instrument to resolve two adjacent sections of distinct Brillouin frequencies, induced by either strain or temperature. The length over which the interaction between pump and Stokes wave occurs determines this parameter. This interaction length is the pulse length and it is defined as $v_g \Delta\tau$ where v_g is the pulse group velocity in the optical fibre and $\Delta\tau$ is the pulse width. The spatial resolution is then expressed as

$$w = v_g \Delta\tau / 2. \tag{IV.11}$$

The factor ½ comes from the backscattered nature of the detected signal. It accounts for the round trip of the signal in the fibre (Hartog 1984, Danielson 1985, Horiguchi 1995). For example a 1.5 ns pulse gives a spatial resolution of 15cm.

IV.C.2. Brillouin frequency resolution

The Brillouin frequency resolution is defined as the smallest Brillouin frequency that can be resolved at a given location along the fibre. Horiguchi proposed a relation that gives an estimate of the minimum detectable frequency change (Horiguchi 1995, Naruse 2005)

$$\delta\nu_B = \frac{\Gamma}{\sqrt{2SNR_o}} = \frac{\Gamma}{\sqrt{2}(SNR_e)^{1/4}}, \tag{IV.12}$$

where Γ is the FWHM of the Brillouin spectrum. SNR_o and SNR_e are the optical and the electrical signal-to-noise power ratios, respectively. The relation between optical and electrical power can explain the difference between the variation of $\delta\nu_B$ with SNR_o and SNR_e. Equation (IV.10) reminds us that the optical power is proportional to the detected photocurrent while the electrical power varies as the square of the photocurrent. The

relation function of SNR_o is appropriately used when the optical spectrum is recorded as it is achieved with BOSA type technique (Appendix 2), or, when the lasers are tuned over the frequency range of interest. The other relation applies to the case of heterodyne (or homodyne) detection of the scattered signal. The spectrum is then analysed with an ESA (section III.). As it appears in equation (IV.12), Brillouin frequency resolution not only depends on the signal level but also on the spectrum width. Common distributed Brillouin sensors are then limited in frequency resolution when $\Delta\tau \leq \tau_B$ due to spectral broadening induced by pulse width shortening (Fellay 1997). For most of the Brillouin sensor configurations, there is clearly a trade-off between spatial and frequency resolution (Naruse 1999).

An example of experimental spectrum was presented in Figure IV.6 for a pulse of $\Delta\tau = 1.5$ ns. Such short pulse would imply that the Brillouin linewidth be broadened by a factor 20 while this spectrum is only 10MHz wider than the Brillouin natural linewidth. This spectrum clearly reveals a unique feature of our DBS. That linewidth narrowing effect has been evidenced experimentally (Bao 1999) and discussed theoretically (Lecoeuche 2000, Afshar 2003, Kalosha 2006). In our DBS, the broadening effect is mitigated by the presence of a DC part in the pulse as the EOM generates pulses with finite extinction ratio. The linewidth reduction is attributed to coherent probe(pulse)-pump(*cw*) interaction (Zou 2005). The DC component interacts with the pump giving two contributions to the loss spectrum: 1) the interaction of the DC component present outside of the pulse with the pump gives a spectrum characteristic of the whole fibre; 2) the interaction of the DC component inside the pulse with the pump gives a spectrum characteristic of local stress as does the pulse interaction with the

pump. At a fixed location, DC component in 2) and pulse have the same frequency and phase leading them to interact coherently with the pump. Eventually, Brillouin loss signal is enhanced and is narrower than the signal that would be produced by the pulse-pump interaction only (infinite ER case). In the experiments discussed in subsequent chapters, we usually use extinction ratios of 20 dB or lower which keep the Brillouin loss spectrum linewidth within a few percent of the Brillouin gain natural linewidth. In these conditions, our DBS can record the Brillouin loss curve at different locations along the fibre and still measure ν_B accurately even for short pulse ($\Delta\tau < 5$ns).

Although equation IV.12 is widely used by the sensing community, this definition specifically applies to the minimum detectable change when the fibre Brillouin frequency is uniform over spatial resolution. It does not address the issue of the frequency resolution when ν_B is not uniform over w. That problem will be discussed in Chapter V and a definition of the spatial resolution accounting for non-uniform ν_B distribution will be proposed (Ravet 2005).

IV.C.3. Dynamic range

The dynamic range (DR) expressed in dB is defined as the difference between the maximum input power to the photodetector and the smallest optical power level that can be detected (case for which the photodiode $SNR_e = 1$). It is a measure of the total loss that can be accommodated by the instrument when performing a measurement (Danielson 1985). The dynamic range is then a function of the power launched into the fibre, the Brillouin interaction, the loss of the components and the receiver characteristics (Horiguchi 1995). It can be expressed as

$$DR = \frac{1}{2}\left\{P_{\max} - |G_p| - \alpha_{comp} - P_d - \frac{1}{2}SNR_{req} + \frac{1}{2}SNR_{imp}\right\}, \quad \text{(IV.13)}$$

where P_{max} is the maximum fibre input power, G_p is the Brillouin loss, α_{comp} is the loss of any component located along the fibre, SNR_{req} is the electrical signal-to-noise ratio required to achieve a target frequency resolution (Equation (IV.12)), and, SNR_{imp} is the electrical signal-to-noise ratio improvement obtained by electrical signal processing (averaging, electrical amplifiers). Various causes limit the maximum fibre input power: 1) P_{max} must be smaller than the non-linear threshold; 2) P_{max} has to be lower than the maximum power that the receiver can handle; 3) another technological constraint on P_{max} is determined by the available power at the laser output. For Brillouin loss and considering that conditions 1) and 2) are verified, we will assume that $P_{max}=P_{cw}$. The factor ½ in front of the bracket is introduced to account for the fact that the signal suffers twice the loss as it propagates in both directions before being measured (Danielson 1985, Horiguchi 1995). The other ½ factors account for the fact that these SNR's are expressed in electrical decibels.

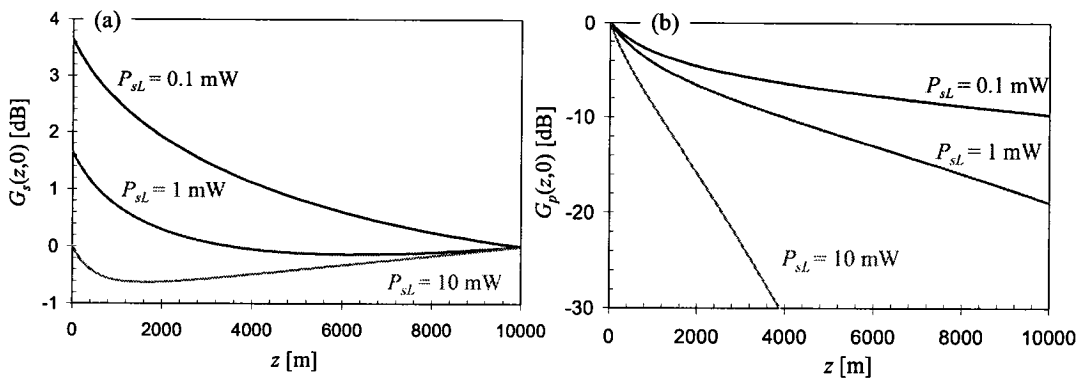

Figure IV.7: (a) Stokes gain in a 10 km long fibre with P_{sL} = 0.1 mW, P_{sL} = 1 mW, P_{sL} = 10 mW and P_{p0} = 6 mW; (b) Pump loss in a 10 km long fibre with P_{sL} = 0.1 mW, P_{sL} = 1 mW, P_{sL} = 10 mW and P_{p0} = 6 mW (Ravet 2006a).

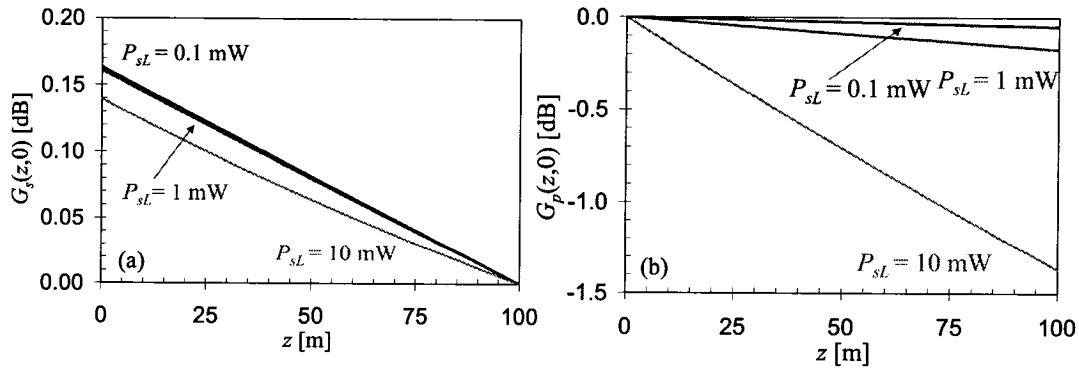

Figure IV.8: (a) Stokes gain in a 100 m long fibre with P_{sL} = 0.1 mW, P_{sL} = 1 mW, P_{sL} = 10 mW and P_{p0} = 6 mW; (b) Pump loss in a 10 km long fibre with P_{sL} = 0.1 mW, P_{sL} = 1 mW, P_{sL} = 10 mW and $P_{p)}$ = 6 mW (Ravet 2006a).

IV.D.Effect of fibre length, position, pump and Stokes power

From the previous sections, it appears that the performance parameters depend on the sensor settings and configuration. Moreover, Chapter II and III taught us that input pump and Stokes powers, as well as fibre length have an influence on the Brillouin interaction. To study further the relationship between sensor settings and performances, we propose to carry out numerical simulations using the steady state solutions (equations (II.46)). We compute Stokes and pump intensities, as a function of power, detuning frequency, position and fibre length, and then analyse the simulations outcomes in terms of spatial resolution, dynamic range and frequency resolution. We can also study the group delay change (equation (II.47.a)), which contributes to delay a Stokes pulse propagating in the fibre. In this section, we propose to address the possible influence of this effect on the sensor performance, and, more specifically, to spatially resolved defects. All these computations were performed for fibre lengths of 100 m, 1 km, 2 km and 10 km. The other parameters of the simulations are $\Delta\nu_B$ = 32 MHz, α= 0.35 dB/km, g_B = 2.3 m/W and A_{eff}=80μm^2 (Ravet 2006a). Note that our approach being based on steady state solutions, it is then valid for pulses larger than 10 ns, without DC

components, and, shorter pulses if its extinction ratio is 20 dB or smaller (and then the DC component large).

IV.D.1. Effect on Brillouin gain and loss

Figure IV.7(a) represents the position variation of pump and Stokes power as a function of Stokes input power. When the input Stokes power is small (P_{sL} = 0.1 mW), the Stokes gain increases monotonically as does the Stokes power. At the Stokes input, the pump power is large enough to contribute to the amplification of the Stokes signal everywhere in the fibre (Figure IV.7(b)). In the case of an input Stokes of 1 mW, the gain first is constant as the pulse moves towards the other fibre end. In that region, the pump is strong enough to balance the effect of the natural loss of the fibre. When the Stokes signal gets closer to the pump origin, the amplification rises because the pump is stronger. When the input Stokes power is 10 mW, the pump is strongly depleted at z=L. The energy transfer to the Stokes beam cannot compensate the natural fibre loss. The amplification increases only in the first 2 km of the fibre. In that last case, very little pump can contribute to the sensing process for position passed 2 km.

The comparison of Figures IV.7 and IV.8 shows that the pump depletion effect reduces as the fibre length decreases. For much shorter fibre (L = 100 m), neither gain nor powers suffer strong variation over the length. On the contrary, they vary monotonically as a function of position as shown in Figure IV.8. Although depletion is weak, it is obvious that it cannot be neglected in the case of 10 mW Stokes and 6 mW pump case.

IV.D.2. Influence of spectrum shape

Similar behaviours are observed when input pump is kept constant but the input Stokes power is increased as reported in Brillouin gain and loss diagrams of Figure IV.9. As the input pump increases, the gain is enhanced (Figure IV.9.(a) to (d)) and can overcome the natural loss of the fibre. When the pump power is raised from 0.1 to 1 mW, the Brillouin gain is significantly improved and the spectrum distribution along the fibre is better resolved (from Figure IV.9.(a) to (b)). The corresponding Brillouin loss spectrum distribution does not show significant differences between these two input pump powers (from Figure IV.9.(e) to (f)): the rate of depletion looks similar. When the pump is set to 6 mW, the rate of depletion becomes larger (Figure IV.9.(g)), which can be associated with an interesting effect visible in Figure IV.9.(c): a double peak is observed in the spectrum one kilometre away from the Stokes input and is developing further when we look down the fibre. The same effect becomes obvious for a pump power of 24 mW, which appears here hundred meters after the pump input end (Figure IV.9.(d)). The frequency of that minimum is the Brillouin frequency of the fibre. That dip formation must be attributed to a very strong depletion of the pump power along the fibre, which is associated to Stokes gain saturation (Takushima 1995, Kovalev 2000, Stépien 2002, Fotiadi 2002). In fact, the Brillouin loss distribution against position reveals that with an increasing Stokes (Figure IV.7) or an increasing pump (Figure IV.9.(e) to (h)), the pump power becomes more and more depleted. Here the limitation comes from the power induced multiple peak spectrum. Such spectral structure would suggest that the fibre is subjected to a non-uniform strain (temperature) distribution along its length.

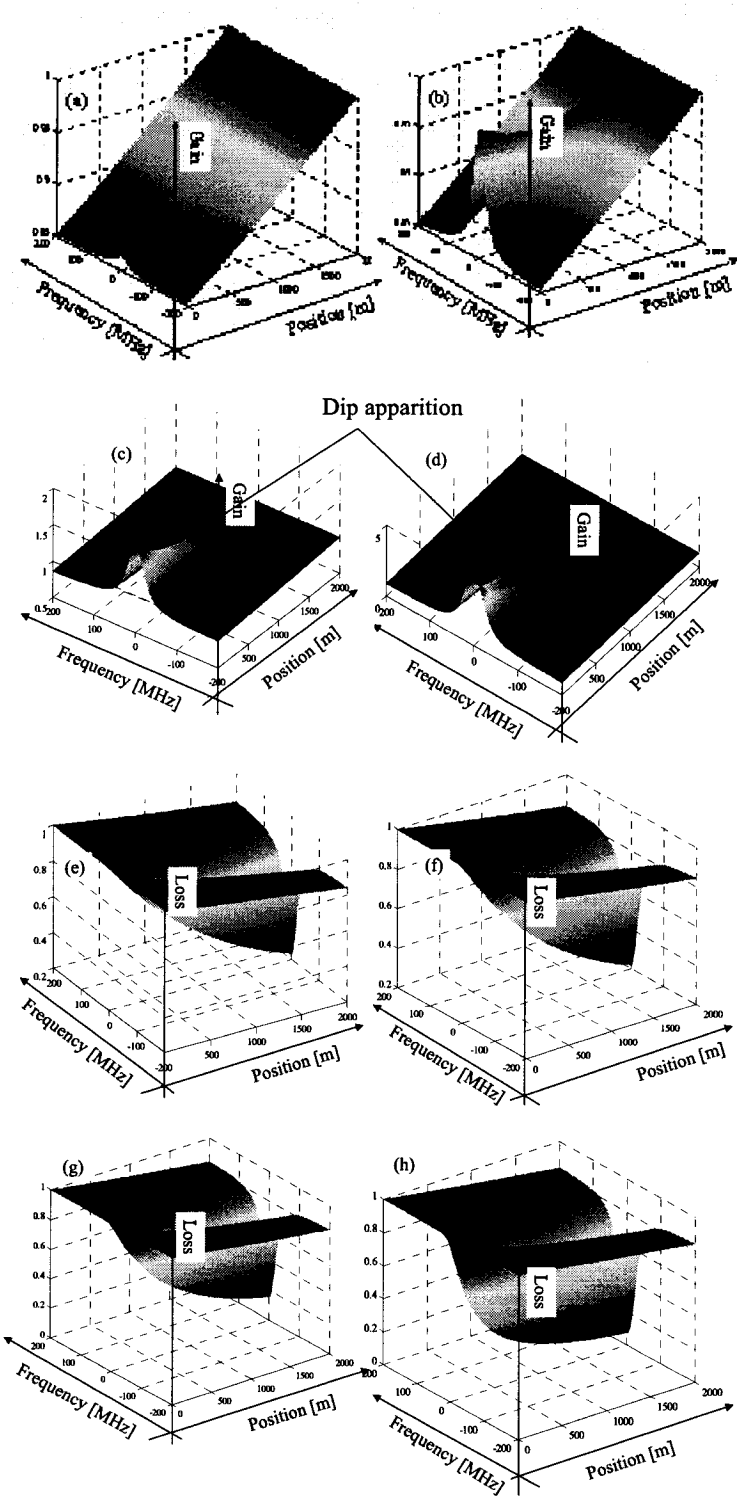

Figure IV.9: Brillouin gain in a 2 km long fibre for constant Stokes power (P_{sL} =0.5 mW) but increasing pump power (a: P_{p0} = 0.1mW; b: P_{p0} = 1 mW; c: P_{p0} = 6 mW; d: P_{p0} = 24 mW); Brillouin loss in a 2 km long fibre for constant Stokes power (P_{sL} = 0.5 mW) but increasing pump power (e: P_{p0} = 0.1mW; f: P_{p0} = 1 mW; g: P_{p0} = 6 mW; h: P_{p0} = 24 mW).

IV.D.3. Effect on group delay

Two extreme cases distinct by the fibre length are presented in Figure IV.10. Figure IV.10.(a) shows the delay variation as a function of position in a 10 km long fibre. The delay of the Stokes signal at the fibre output (z=0) is 20 ns for P_{sL} = 0.1 mW, 11 ns for P_{sL} = 1 mW and 3 ns for P_{sL} = 10 mW while the undepleted case (equation (II.52)) yields 55 ns when the pulse exits the fibre. Both delay variations with position remain far below the undepleted approximation. Hence lower Stokes power induces more delay. Because of the depletion effect, the real Brillouin gain is much smaller than the undepleted case. The location error due to slow light effect is well below the spatial resolution defined by the pulse width. Figure IV.10.(b) depicts the delay variation with position in a 100 m long fibre. In 100 m applications, the targeted spatial resolution can be as low as 20 cm, which corresponds to a pulse width of 2 ns.

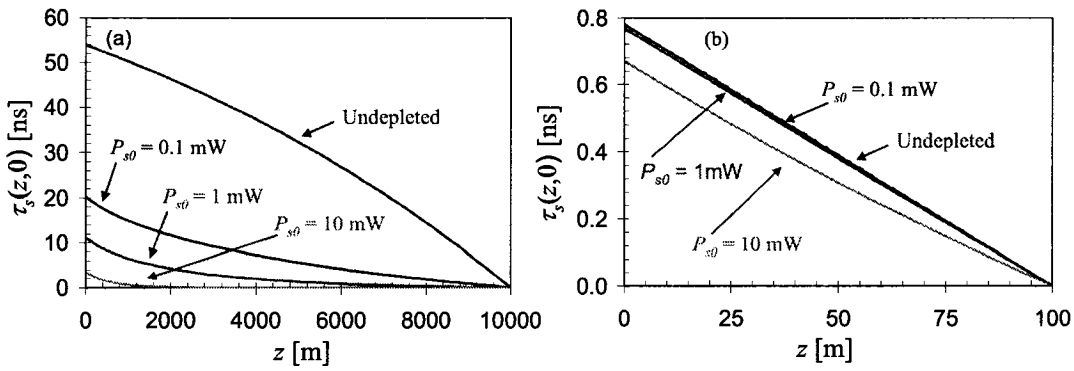

Figure IV.10: (a) Group delay in a 10 km long fibre with P_{sL} = 0.1 mW, P_{sL} = 1 mW, P_{sL} = 10 mW and P_{p0} = 6 mW;; (b) Group delay in a 100 m long fibre with P_{sL} = 0.1 mW, P_{sL} = 1 mW, P_{sL} = 10 mW and P_{p0} = 6 mW (Ravet 2006a).

For a given fibre length with an appropriate selection of Stokes and pump powers, pulse delay can be mitigated and the location error minimized. For example, the location error in the 100 m can be lowered further as it is reported in Figure IV.10 where

a Stokes power larger than 10 mW is used. Figure IV.10 also reveals that the undepleted approximation is the asymptotic case of our model. When the Stokes power diminishes, the delay increases until it reaches a plateau value

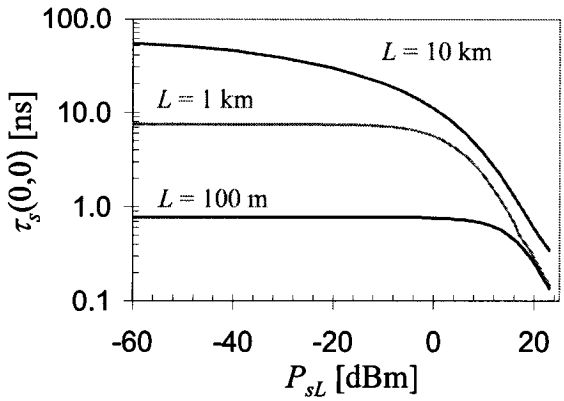

Figure IV.11: Group delay of output Stokes beam (z = 0) as a function of input Stokes power for three fibre lengths (L = 100 m, L = 1 km, L= 10 km) and P_{p0} = 6mW (Ravet 2006a).

The purpose of the Brillouin sensor is to detect temperature and/or strain variations that are linearly related to Brillouin frequency changes. Moreover, in practical conditions, the Brillouin frequency is never uniform due mainly to environmental stresses on the fibre. These variations shift local resonances and then reduce pump depletion along the fibre. Ultimately, they affect group index and hence decrease group delay. In order to estimate qualitatively the impact of a non-uniform Brillouin frequency distribution, we study two profile cases for a 1 km long fibre. These profiles are made of a short section (stressed section) of different length (δl = 10m and δl = 100 m) whose Brillouin frequency is up-shifted by 50 MHz and located in the middle of the test fibre. The Brillouin frequency is unshifted elsewhere along the fibre. A non-uniform Brillouin frequency profile limits the delay as shown in Figure IV.12.(a) where those two cases are compared with a uniform fibre. It is clear that the delay decreases when the fibre strain or temperature is non-uniform because during

propagation pulse encounters sections that are off-resonance. The amplitude of the delay reduction increases if the section is larger. That behaviour can be associated to the largest gain drops that occurs for the case of the fibre whose "stressed" section is longer (δl = 100 m) as presented in Figure IV.12.(b). The short section case (δl = 10 m) does not differ excessively from the uniform. The same analysis was conducted for stressed section located elsewhere in the fibre and for longer fibres (10 km), both leading to similar results.

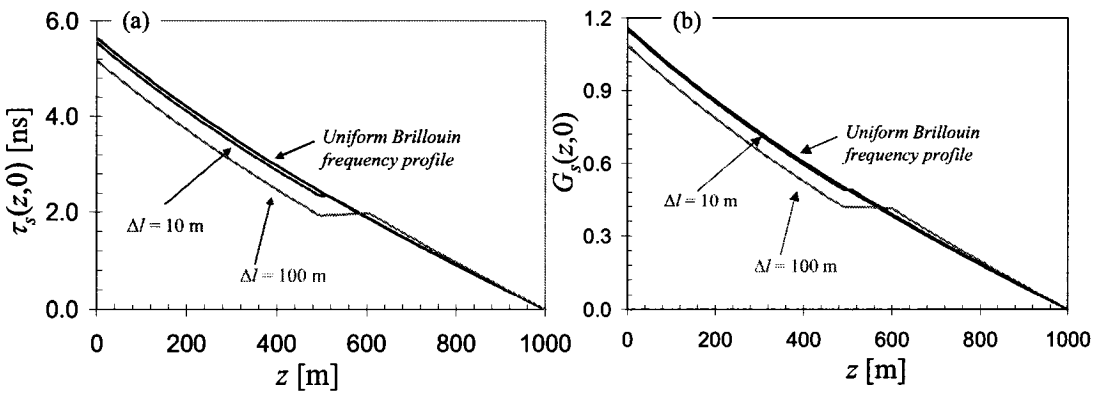

Figure IV.12: Group delay (a) and gain (b) of a Stokes beam calculated at the Brillouin frequency of a fibre as a function of position for uniform and non uniform (δl = 10 m, δl = 100 m) Brillouin frequency profile; power parameters are P_{p0} = 6 mW, P_{sL} = 1 mW. The non-uniform cases are up-shifted by 50 MHz (Ravet 2006a).

The pulse delay depends on the pump power, the Stokes power, fibre length as well as Brillouin frequency distribution. These parameters strongly influence the actual gain experienced by the pulse and hence the Stokes group delay. Uniform Brillouin frequency leads systematically to higher delay. It corresponds to the highest location error for distributed sensor, and it is less than the pulse width.

IV.D.4. Optimum power settings

Figure IV.7 clearly emphasizes the role of gain build-up and pump depletion. The overall high gain for Stokes power of 0.1 mW indicates high delay as shown in

Figure IV.10. In the 10 mW case, small delay is associated with small overall gain, while Stokes power and gain distributions vary significantly over the last 2 km of the pulse propagation in the fibre. This behaviour is the result of a stronger interaction of pump with Stokes, which is a condition for better Brillouin frequency resolution as electrostriction is enhanced. An example of contrast increase is shown in Figure IV.13 where the Brillouin loss distribution at the stressed frequency is drawn as a function of position. That effect results in SNR improvement and hence in better strain and temperature resolution.

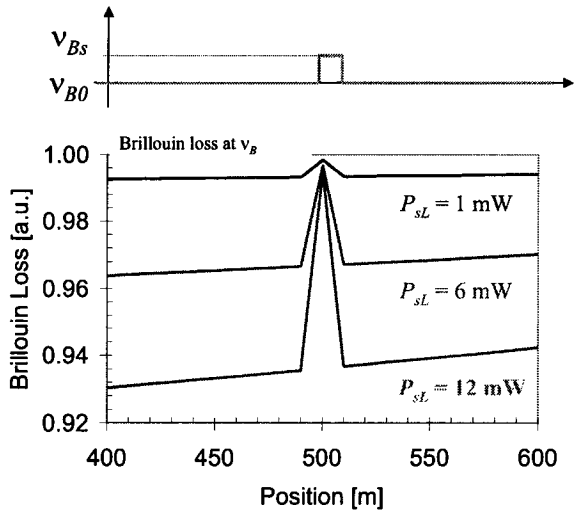

Figure IV.13 Brillouin loss distributions calculated, at ν_{B0} of a 1 km long fibre, for P_{sL} = 1 mW, P_{sL} = 6 mW, P_{sL} = 12 μW; a stress induced Brillouin frequency shift of ν_{Bs} = 50 MHz is located at z = 500m; other simulation parameters are P_{p0} = 6 mW, δl = 10 m.

If depletion is required, it should remain moderate because too high depletion brings in three kinds of negative effects. First, a large depletion of the pump would make it impossible to sense temperature and strain over the whole fibre length. Only the initial sections of the fibre would be measurable while no pump power would be left along the rest of the fibre to achieve interaction between pump and Stokes beams.

Second, when the pulse DC level is strong, which helps to limit the delay, there is always the risk of having the local spectrum contaminated with events happening elsewhere along the fibre, which is also known as non-local effects as it is illustrated in Figure IV.14 (Bao 1995, Geinitz 1999, Bao 2006). Figure IV.14 shows the effect of a stress, located in the middle of the fibre, on the Stokes spectrum measured near the fibre output for various DC Stokes levels. It is clear that an increase Stokes power contributes to distort strongly the spectrum. Third, large power contributes to the increase of the phonon relaxation time (Bao 2006), which in turn degrades spatial resolution and SNR. According to the experimental results presented in (Bao 2006) for a 40 m long single mode fibre, we know that SNR improves as a function of power until it reaches a maximum around 5 mW. SNR then drops degrading the frequency resolution. These effects should be avoided for distributed sensor systems. Therefore moderate depletion is recommended for the pump and probe power of 4-5 mW (Bao 1995, Bao 2006).

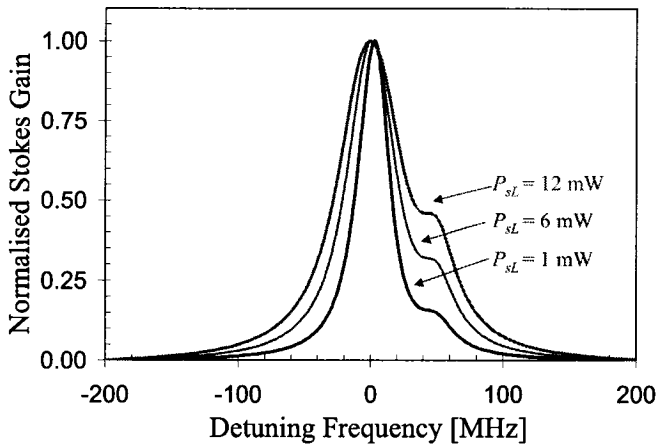

Figure IV.14 Brillouin gain spectrum near the fibre Stokes output for P_{sL} = 1 mW, P_{sL} = 6 mW, P_{sL} = 12 mW for a uniform fibre except on z = 1000 m where a stress induced frequency shift is 50 MHz. Simulation parameters are L = 2 km, P_{p0} = 6 mW, δl = 200 m.

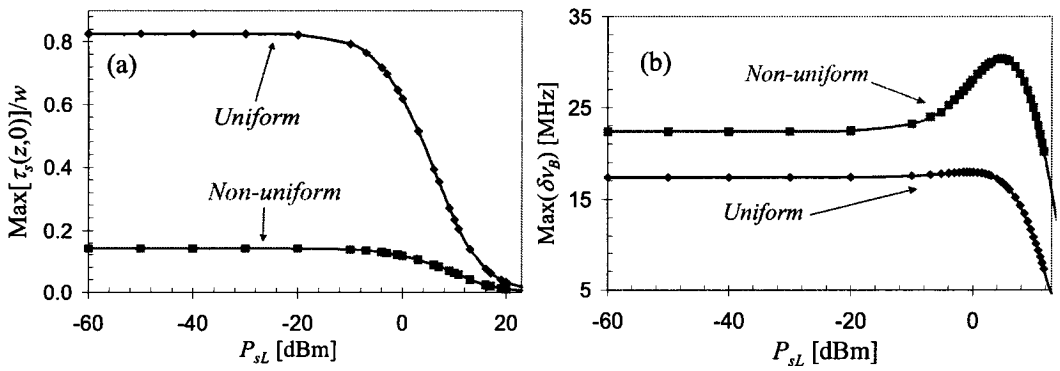

Figure IV.15 (a) Comparison of the effect (worst-case) of slow light on spatial resolution for uniform and non-uniform fibres ($\Delta\tau$ = 10 ns); (b) Comparison of the worst-case Brillouin frequency resolution for uniform and non-uniform fibres. Simulation parameters are L = 1 km, P_{p0} = 6 mW.

Figure IV.15 summarises the outcomes of whole section IV.D for the BOTDA configuration based on the measurement of pump depletion. It shows the effect of increasing input Stokes power on spatial and frequency resolutions (equation (IV.12)) for two fibres with uniform and sinusoidal (amplitude is 25 MHz and period is 100 m) Brillouin frequency distribution. Figure IV.15.(a) compares the fraction of delay relative to the spatial resolution (w = 1 m) for the two fibre types. It appears that the non-uniform fibre experiences a smaller spatial resolution error deviation (positive deviation) than the uniform fibre (see also Fig. IV.12) for any level of input Stokes power. As mentioned in setion IV.C, the total gain experienced by a Stokes pulse propagating in a uniform fibre at a fixed frequency is lower than in the case of a uniform fibre. As a consequence, the delay must be smaller, and, hence the spatial resolution degradation is then mitigated. At the contrary, a non-uniform fibre has a broadened spectrum (see also Fig. IV.14) and reduced SNR (due to smaller gain and lower pump depletion), which contribute to degrade the Brillouin frequency resolution from the uniform fibre case (Fig. IV.15.(b)). An interesting feature can be observed in Fig.

IV.15(b). For both fibres, the error first worsens when the input Stokes power is increased. As expected, pump depletion leads to the broadening of the spectrum. At the same time, a stronger depletion should improve the SNR as shown in Fig. IV.13. Here the linewidth dominates the ratio of equation (IV.12). The error on the frequency resolution then decreases because the depletion becomes large enough to compensate for the broadening as it can be seen on Fig. IV.15(b). Note that in this regime, the dynamic range would be limited. It is then clear that a trade-off between large gain and pump depletion over the entire sensing length must be achieved: on the one hand, the sensor needs a large dynamic range, which is obtained with low Stokes power but with large delays; on the other hand, power depletion brings stronger interaction and then lower gain influencing strain and temperature resolution, but significantly reducing delay. Those two issues must be accounted for to provide the best spatial resolution combined with optimum temperature and strain resolution. The power threshold (relation (III.6)) for Brillouin fibre amplifiers derived in Chapter III gives an upper limit to the launched pump power.

IV.E. Phenomenological modelling of the Brillouin sensor operation

IV.E.1. Model description

In Chapter II, we have introduced the steady state coupled intensity equations that describe stimulated Brillouin scattering interaction between two counter-propagating laser beams as a Brillouin loss process (equations (II.45)). We propose to base our model on these equations in which the Stokes signal is a pulse, and, the pump is a *cw* lightwave. We also assume that the gain coefficient g depends on position. The position dependence of g is attributed to the fact that fibres do not have a perfectly

uniform Brillouin frequency distribution. In addition, the purpose of a sensor is to detect Brillouin frequency variations induced by the environment. Rigorously, these equations can only be used to describe steady state or long pulses ($\Delta\tau > 10$ ns) interaction. We discuss here how this model can accommodate shorter pulses.

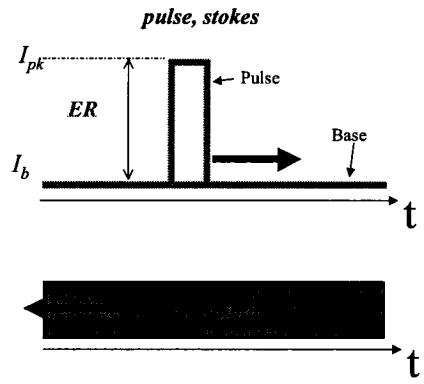

Figure IV.16: Model of pump-stokes (pulse) interaction.

The weakly depleted approximation can be applied to most of the sensing cases we will meet. Let us give two major reasons. First, the pulse length, and hence the Brillouin interaction length, exceeds rarely 100 m, in which case the pump depletion is always weak (Figure III.20.(a)). Second, the DC component of the pulse can significantly deplete the pump if the fibre is longer than a few hundred meters. We then want to make sure that $P_b < P_{th}$. Hopefully, it is in practice a fraction of the pulse peak power (e.g. a few tenth of mW at the very maximum). We then assume that the steady state condition is verified. As in section II.C.5, we make the assumption that pump is weakly depleted. If we choose to let the pulse enter into the fibre at $z = 0$ and to launch the pump from $z = L$, then initial conditions to equation II.45.b are I_{s0} and I_{cwL}, for the Stokes and the *cw* pump lightwaves respectively. Solving equation II.45.b leads to an approximate expression for the Stokes intensity similar to Equation II.49

$$I_s(\nu,z)=I_{s0}\exp\left[g(\nu,z)I_{cwL}\frac{e^{-\alpha L}}{\alpha}\left(e^{\alpha z}-1\right)-\alpha z\right]. \tag{IV.14}$$

We now follow the assumption that the Stokes wave is constituted of two components (Lecoeuche 2000, Afshar 2003, Kalosha 2006): one is time dependent (AC part of the pulse), which is characterized by the pulsewidth ($\Delta\tau$) and the peak intensity (I_{pk}); the other is the base (DC part) which is a continuous wave signal (*cw*) and determined by its intensity (I_b). Figure IV.16 illustrates this model. The residual DC part in the pulse must be attributed to the EOM leakage and/or the deliberate bias of the EOM as discussed in previous sections of the current chapter. We have seen that the presence of the DC component has some benefits (Zou 2005). The Stokes intensity is then the sum of these two components $I_s=I_{pk}+I_b$. Solving equation II.45.b with these Stokes intensities, and their spatial dependence expressed as equation IV.14, we obtain the total Brillouin loss, which can be expressed in this general form for an arbitrary length l (Bao 1995)

$$\begin{aligned}
G_T(\nu,z) &\equiv \frac{I_{cw}(\nu,z)}{I_{cw}(\nu,z+l)} \\
&= \exp\left\{\alpha w-\int_z^{z+l} g(\nu,\zeta)I_{p0}\right. \\
&\qquad \left.\exp\left[g(\nu,\zeta)I_{cwL}\frac{e^{-\alpha L}}{\alpha}\left(e^{\alpha\zeta}-1\right)-\alpha\zeta\right]d\zeta\right\} \\
&= \exp\left\{\alpha w-\int_z^{z+l} g(\nu,\zeta)\left(I_{pk}+I_b\right)\right. \\
&\qquad \left.\exp\left[g(\nu,\zeta)I_{cwL}\frac{e^{-\alpha L}}{\alpha}\left(e^{\alpha\zeta}-1\right)-\alpha\zeta\right]d\zeta\right\}.
\end{aligned} \tag{IV.16}$$

We see that the AC and DC components of the pulse can be separated leading to the following generic form of the Brillouin loss

$$G_T(\nu,z)=G_{pk}(\nu,z)G_b(\nu,z), \tag{IV.17}$$

where G_{pk} is the Pump-AC Brillouin loss and G_b is the Pump-DC Brillouin loss. Due to their very distinct natures, we want to separate the calculation of these two interactions.

First, we consider the pump-AC interaction. The steady state approximation is valid for pulses larger than the phonon lifetime ($\Delta\tau$ > 10ns), which is equivalent to a spatial resolution w>1m. We know that nanosecond pulses provoke the broadening of the Brillouin loss spectrum and then reduce the strain (temperature) measurement accuracy, while such pulses are required to achieve centimetre spatial resolution. As the broadening is induced by the wide spectrum of the pulse, we assume that each pulse spectrum component excites individually the phonon field whose spectrum is given by a Lorentzian distribution. These individual excitations are adding up over the pulse spectrum frequency range. That mechanism is described mathematically by a convolution product. Therefore, we account for the pulse effect in these equations by replacing g with the transient gain coefficient g_{pk}, defined as the convolution of the Brillouin natural gain $g(\nu,z)$ with the distribution $P_{pk}b(\nu)$ of the power spectrum of the pulse (Naruse 1999, Smith 1999)

$$g_{pk}(\nu,z)=g(\nu,z)*b(\nu). \tag{IV.18}$$

We then assume that the pulse waveform has a rectangular shape, we can then calculate the convolution analytically:

$$g_{pk}(\nu,z)=g(\nu,z)\left\{1-\frac{1}{\pi\Delta\nu_B\Delta\tau}\frac{g(\nu,z)}{g_B}\left(1-\left(2\frac{\nu-\nu_B(z)}{\Delta\nu_B}\right)^2\right)+\right.$$
$$\left.+\frac{e^{-\pi\Delta\nu_B\Delta\tau}}{\pi\Delta\nu_B\Delta\tau}\frac{g(\nu,z)}{g_B}\left[\left\{1-\left(2\frac{\nu-\nu_B(z)}{\Delta\nu_B}\right)^2\right\}\cos(2\pi(\nu-\nu_B(z))\Delta\tau)-4\frac{\nu-\nu_B(z)}{\Delta\nu_B}\sin(2\pi(\nu-\nu_B(z))\Delta\tau)\right]\right\}. \tag{IV.19}$$

Finally, we integrate equation II.45.b for the AC part of the Stokes wave at any position over the spatial resolution (w) (Bao 1995) and obtain the Brillouin loss spectrum G_{pk} at z:

$$G_{pk}(\nu,z)\equiv\frac{I_{cw}(\nu,z)}{I_{cw}(\nu,z+w)}$$
$$=\exp\left\{\alpha w-\int_{z}^{z+w}g_{pk}(\nu,\zeta)I_{pk0}\right.$$
$$\left.\exp\left[g_{pk}(\nu,\zeta)I_{cwL}\frac{e^{-\alpha L}}{\alpha}\left(e^{\alpha\zeta}-1\right)-\alpha\zeta\right]d\zeta\right\}, \qquad \text{(IV.20)}$$

Now, we want to evaluate the interaction between the base and the pump wave. Due to the DC nature of the base, we assume that its interaction with the pump can be modelled by the steady state equations (II.45) without additional assumptions. Here the Stokes intensity reduces to $I_b=ERI_{pk}$ where ER is the extinction ratio of the optical pulse. The integration interval extends to the whole fibre length. The Brillouin loss spectrum contribution from the base-pump is then expressed as

$$G_b(\nu,z)=\exp\left\{\alpha(z-L)-ER\int_{z}^{L}g(\nu,\zeta)I_{pk0}\right.$$
$$\left.\exp\left[g(\nu,\zeta)I_{cwL}\frac{e^{-\alpha L}}{\alpha}\left(e^{\alpha\zeta}-1\right)-\alpha\zeta\right]d\zeta\right\}. \qquad \text{(II.21)}$$

When it is assumed that the Stokes pulse is the sum of two parts, DC and AC intensities, that are decoupled but interacting individually with the pump, the total Brillouin loss spectrum is the product of G_{pk} and G_b as shown in equation IV.17. G_T of a uniform Brillouin frequency distribution is characterized by a single peak spectrum whose FWHM, Γ, is close to $\Delta\nu_B$ when pump is weakly depleted and under steady state condition. In general, Γ varies with L, z, I_{pk0}, I_{cwL} and ER, which are the cause of spectrum distortion.

IV.E.2. Model discussion

We conducted a systematic study of the influence of pulse width, extinction ratio on the linewidth of the Brillouin loss. Brillouin frequency was assumed to be uniform along the fibres. Typical results for short and long fibres are presented in Figure IV.17, which are confirmed by simulations on short fibres (up to 10 m) by an accurate model based on the exact solution to the three wave equations for SBS (Kalosha 2006). This agreement with exact solutions strengthens our confidence in the validity of the present approach. As shown in Figure IV.17, Γ increases when the pulse width decreases until it reaches a maximum. Then Γ drops to a value close to $\Delta\nu_B$. Small *ER* clearly limits the increase of the linewidth. As previously discussed, the region of very short pulse offers optimum sensing characteristics because it combines high spatial and frequency resolutions (Kalosha 2006).

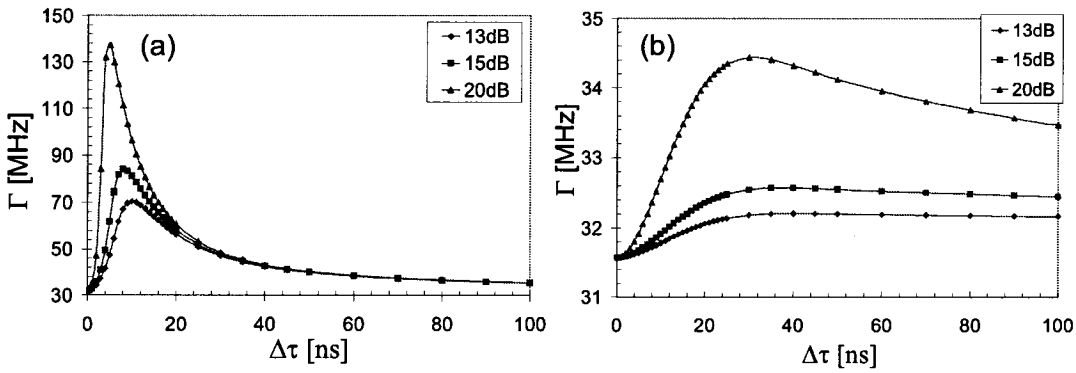

Figure IV.17: Brillouin loss spectrum width as a function of pulsewidth and extinction ratio: (a) P_{p0} =10 mW, P_{cwL} =5 mW, L = 10 m, z = 5 m; (b) P_{p0} = 10 mW, P_{cwL} = 5 mW, L = 10000 m, z = 5000 m (Ravet 2006c).

When $\Delta\tau \approx$ 10 ns, the observed broadening must be attributed to the pulse spectrum widening. For nanosecond pulses, Γ drops due to the DC level dominating the Brillouin interaction over long fibre length and relative small contribution of the pulse

portion. If large pulses are used ($\Delta\tau >> 10$ ns), the pulse spectrum is much narrower than $\Delta\nu_B$. The Brillouin loss spectrum tends to be similar to the spectrum resulting from the interaction of *cw* pump and Stokes lightwaves. The main difference between short and long fibres, respectively Figures IV.17.(a) and (b), must be attributed to increased influence of the base. Pump and base interaction extending over the whole fibre length, Γ tends to remain close to steady state value when the fibre is long as it appears in Figure IV.17.(b).

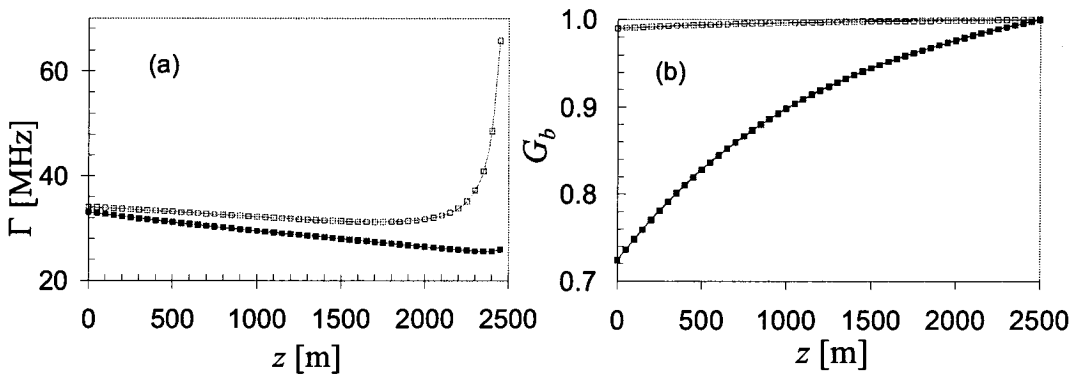

Figure IV.18: (a) Brillouin loss spectrum width as a function of position and extinction ratio (filled symbols:*ER* = 10 dB; open symbols: *ER* = 25 dB); (b) base contribution to total Brillouin loss as a function of position and extinction ratio (filled symbols: *ER* = 10dB; open symbols: *ER* = 25dB), these values are calculated at the Brillouin frequency; Simulation parameters are: $\nu = \nu_B$, $P_{p0} = 25$ mW, $P_{cwL} = 5$ mW, $\Delta\tau = 10$ ns, $L = 2500$ m (Ravet 2006c).

Γ also varies with position as shown in Fig IV.18 (for a 2500 m long fibre and w = 1 m. In the *ER*=25dB case, it is observed that Γ first decreases. In the last kilometres, Γ starts to rise significantly. The increase of Γ is very weak when considering the *ER* = 10 dB situation. Similarly to Figure IV.18, these curves confirm the role played by the base in mitigating the spectrum broadening. The effect of spectrum narrowing with increasing distance can be attributed to the enhancement of the scattering of Stokes spectral components near the peak of the resonance while the pulse is propagating along

the fibre. Equivalently, a broader spectrum at the pulse input can be attributed to the effect of pump depletion. Spectrum widening observed at the fibre end can be understood by analysing Figure IV.18.(b) representing the base (G_b) contribution to the total Brillouin loss (G_T) as a function of position and *ER*. In the case of high spatial resolution sensor ($w \leq 1$ m), the change of G_{pk} as a function of z is small relative to G_b and does not depend on *ER*. Close to the pump input, the Brillouin loss is smaller ($G_b \rightarrow 1$ when $z \rightarrow L$). That effect is emphasized and affects G_b over the whole fibre length ($G_b \approx 1$) when the pulse extinction ratio is large. It is then possible to observe the pulse spectrum broadening in the last few hundred meters of the fibre. Spectrum narrowing with position can be experimentally evidenced as illustrated in Figure IV.19. The experiment was carried out with a Brillouin sensor using two DFB laser in the 1.55 μm region. The typical linewidth of these lasers is about 10 MHz and contributes to broaden the Brillouin loss spectrum. Under weak depletion condition, we measured that $\Gamma \approx \Delta\nu_B \approx 45$ MHz. The phenomenological model is used to calculate the spectrum along the fibre. The FWHM of the reconstructed profile is plotted on Figure IV.19. It is obvious that the reconstruction matches the experimental trend, which is a confirmation that the model is capable to simulate the effect of moderate pump depletion that influences the spectrum shape.

IV.F. Summary

After reviewing strain and temperature mechanisms, the DBS and the sensor performance parameters, we have discussed the influence of the sensor settings on the instrument performance. The major outcome is that the sensor must operate in moderate pump depletion regime to achieve good spatial resolution without affecting the

frequency resolution or the dynamic range. An estimate of the upper limit power settings that can be chosen are given by the power threshold for Brillouin fibre amplifier (equation III.6).

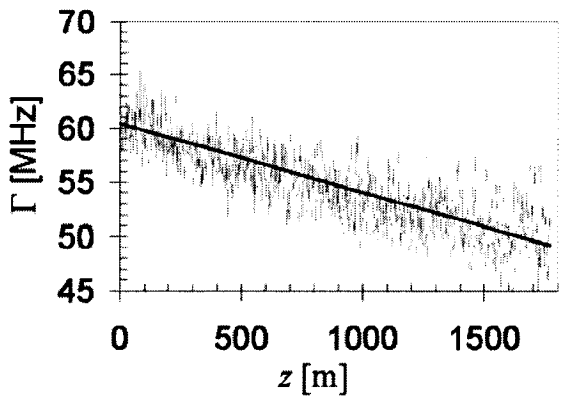

Figure IV.19: Measured (light grey line) and calculated (dark line) Brillouin loss spectrum width, Γ, as a function of position for a uniform fiber; experimental and simulation parameters are P_{p0} = 20 mW, P_{cwL} = 5 mW, L = 1800m, $\Delta\tau$ = 10 ns, ER = 10 dB, $\Delta\nu_B$ = 45 MHz (Ravet 2006a).

We introduced a simple mathematical model that describes the sensor operation in moderate depletion regime. It succeeded to reproduce results from the literature obtained experimentally and by the simulation of the three wave equations for SBS. Thanks to its simplicity, we were able to obtain results in a few seconds with Pentium IV personal computer instead of days of computation that would have been required by the resolution of the three wave equations (II.37) on a linux server. The model was also successful to predict the trends observed in experimental data.

Chapter V: Data analysis methodology

V.A. Introduction

In the previous chapter, we have seen that the accuracy of the measurement of temperature and strain is affected by the Brillouin spectrum shape. The Brillouin spectrum shape itself is influenced by pulse width ($\Delta\tau$), pulse shape, Stokes (pulse peak power, P_{pk0}) and pump powers (cw, P_{cwL}), as well as extinction ratio of optical pulse (ER) or fibre length (L). In addition, strain is rarely uniform over the pulse length, which results in distortion of the Brillouin spectrum. Therefore large strain gradients over short length integrated in the Brillouin spectrum are underestimated while these are an indication that the structure can be in jeopardy. Accurate strain detection and localization can be achieved by a data processing method, which consists of reconstructing the measured Brillouin spectrum by solving the three wave equations for stimulated Brillouin scattering (SBS) such that sensor parameters are taken into account (Kalosha 2006). Strain profiling requires centimeter spatial resolution so that big problems can be detected at an early stage of their formation and then potential disaster can be prevented. This implies that the sensor operates in transient regime. Solutions to the three wave equations are only numerical and require powerful computers and lengthy computations (from hours to days) for fibres that are hundred meters long. This situation is unacceptable because critical stresses must be detected in real-time and sensing length can be as large as 50 km (Bao 1995).

To overcome this practical difficulty, we propose to implement the phenomenological model, which is a description of the sensing mechanism based on

steady state analytical solution adapted to transient regime. We have seen in Chapter IV that the phenomenological model brings in two features: 1) It carries the pulse information through the convolution of the natural Brillouin gain with the pulse power spectrum; 2) the pulse base is treated as pure steady state contribution. These two processes are calculated separately. This approach has three advantages. First, it can deal with analytical relations, which makes this approach easier to handle large distances while the transient wave equations can only deal with tens to hundreds of meters of fibre length with a reasonably short computation time. Moreover, the model is capable to handle complicated strain profiles over the pulse length thanks to the analytical nature of its solution, which makes the processing time faster than that of a rigorous numerical solution. Second, it is also more accurate than the current de-convolution technique using multiple distributions fitting (DeMerchant 2000), without any consideration for experimental conditions. Third, the model can handle non-local effects induced by pump depletion, which is a cause of spectrum distortion (Bao 1995, Bernini 2002). In fact, under large pump depletion Brillouin frequency shift at a given location influences the gain shape at the next positions. In such a case, the spectrum may be distorted.

All these issues being addressed in previous chapters, we want to focus here on the implementation of a signal processing approach based on the phenomenological model (Ravet 2006c). The spectrum reconstruction being recursive, its efficiency can be improved by choosing appropriate initial conditions. We want these initial conditions based on the physics of the DBS which is possible by analysing the shape of the spectrum. The shape analysis is possible by introducing a set of tools such as the length-stress diagram (Ravet 2005a, Ravet 2006c), the spectrum form factors (Ravet 2006) and the Rayleigh Equivalent Criterion (REC, Ravet 2005). This chapter first discusses the

validity of these tools. It then shows how they can be used in conjunction with the phenomenological model. Finally, the whole signal processing scheme is applied to well controlled experimental data.

Note that a signal processing technique has been developed recently (Bernini 2002, Minardo 2005). The authors applied a harmonic decomposition to the unknown strain/temperature profile, and reconstructed, iteratively, the waveform at each detuning frequency. They treated the Brillouin interaction by solving the coupled intensity equations in moderately depleted regime, limiting the applicability to pulse width larger than the phonon lifetime. Our method differs from their approach in two aspects. First, our spectral evaluation is based on peak search, Rayleigh criterion and form factor analysis. The strain components are obtained by an analysis of the spectrum shape constraining the initial values, and, hence speeding up the iterative process of the reconstruction. Second, we adapted the steady state solution to account for the pulse influence on the spectrum shape such as those induced in transient regime.

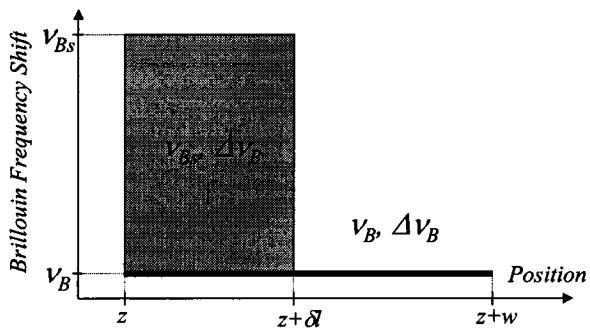

Figure V.1: Brillouin Frequency distribution within the length of the spatial resolution. Both sections have the same Brillouin linewidth but have a distinct Brillouin frequency (Ravet 2005a).

V.B. Tools for data analysis

V.B.1. Effect of stress length and strength

To study the effect of changing stress length and strength on the spectrum shape, we assume that the sensing fibre has a uniform Brillouin frequency (ν_B) over its whole length (L) except for a short section at distance z whose spatial extension δl is smaller than the spatial resolution ($\delta l \leq w$) and has a different Brillouin frequency shift (ν_{Bs}). As appearing in Figure V.1, within the spatial resolution at z, the Brillouin frequency shift (ν_{Bs}) is constant over δl, while the rest of the pulse covers w- δl with a Brillouin frequency shift of ν_B. We use the phenomenological model for $w > 1$ m to generate composite spectra for various combinations of ν_B, ν_{Bs} and δl. Smaller spatial resolution could be considered but the analysis would be more complex without bringing useful information. We introduce the normalized Brillouin frequency shift $\Omega_{Bs}=(\nu_{Bs}-\nu_B)/\Gamma$ where Γ is the FWHM of the normalized Brillouin loss spectrum for given sensing parameters.

Figure V.2 illustrates how the Brillouin spectrum shape changes when ν_B, ν_{Bs} and δl are varied. In this case, we have that δl = 5 m, ν_B = 12800 MHz while ν_{Bs} is 12810MHz (curve a), 12820MHz (curve b) and 12860MHz (curve c). Curve (a) is a single-peak distribution but lightly distorted. Curve (b) is still a single-peak distribution but it appears to be skewed. The central frequencies in Curves (a) and (b) are shifted from stress-free frequency (12800MHz), even if δl (stress section) is only 25% of the spatial resolution. The curve (c) has two peaks at 12800MHz and 12860MHz respectively due to the loose part of the fibre and the stressed section.

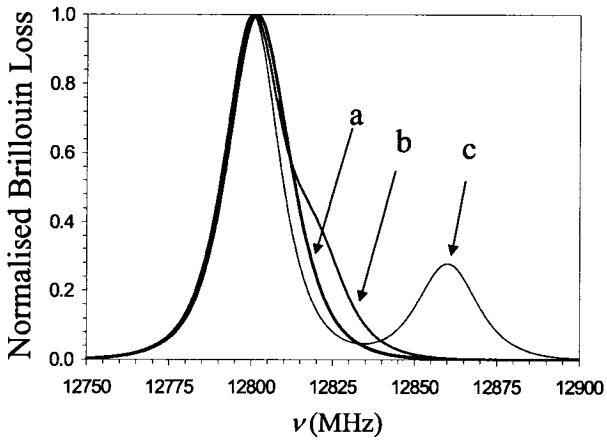

Figure V.2: Composite spectra for three distinct Brillouin frequency shift. Spectra a, b, and c are respectively associated with a Brillouin frequency of 12810MHz, 12820MHz and 12860MHz. The unstressed Brillouin Frequency shift is 12800MHz. The simulation parameters are P_{pk0} = 30 mW, P_{cwL} = 5 mW, L = 1000 m, z = 500 m, w = 20 m, δl= 5 m. (Ravet 2005a).

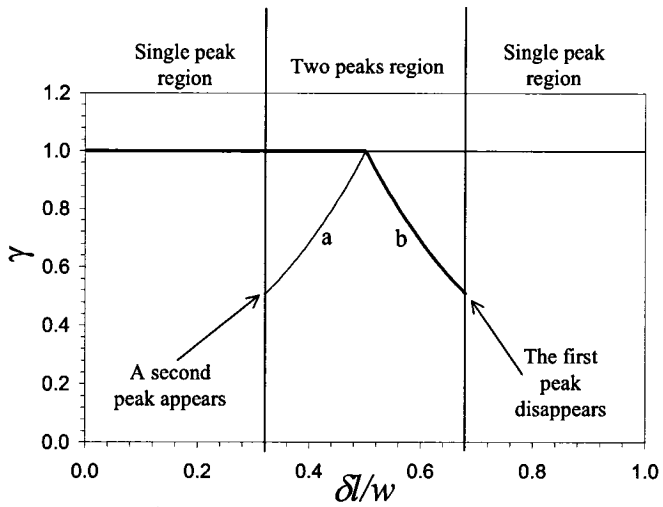

Figure V.3: Relative peak height (γ) calculated for the following simulation parameters: P_{pk0} = 30 mW, P_{cwL} = 5 mW, L = 1000 m, z = 500 m, w = 20 m, Ω_{Bs} = 0.75. Curves a and b correspond to stressed and unstressed peaks respectively (Ravet 2005a).

The curves in Figure V.2 clearly show the influence of the both stress length and strength on the spectrum shape. There is a transition from a single peak spectrum to a dual peak spectrum, which is depending on the stressed length as shown in Figure V.3.

Figure V.3 represents the dependence of the relative peak height (γ) [18] as a function of $\delta l/w$. In this example the frequency difference is kept constant ($\Omega_{Bs} = 0.75$) but $\delta l/w$ is varied from 0 to 1. Curves a and b reports respectively the γ of the stressed and unstressed peaks. When $\delta l/w < 0.5$ the unstressed peak (b) is the dominant contribution to the loss profile. When $\delta l/w > 0.5$ the stressed peak (a) becomes the dominant contribution to the loss profile. $\delta l/w = 0.5$ acts as the border that separates the attribution of the dominant peak. The stressed peak (a) appears as soon as $\delta l/w > 0.32$. The unstressed peak (b) disappears as soon as $\delta l/w > 0.68$. In summary, two peaks profile can be observed when $0.32 \leq \delta l/w < 0.68$ for a normalised Brillouin frequency shift of 0.75. Similar behaviours can be reproduced for other values of the normalised Brillouin frequency shift but the range of $\delta l/w$ over which the two peaks can be detected decreases when Ω_{Bs} is reduced.

V.B.2. Length-Strength diagram

Section V.B.1 has shown that the spectrum shape is driven by the combination of the normalised Brillouin frequency shift and the stressed section length. Such behaviour is summarised in a Length-Strength diagram represented in Figure V.4. This diagram is the result of a systematic analysis of the spectrum shape as a function of the normalised Brillouin frequency shift and the stressed section length. We search for the number of peaks present in the spectrum for each combination of $\delta l/w$ and Ω_{Bs}. We record each couple ($\delta l/w$,Ω_{Bs}) corresponding to the transition from single to dual peak spectrum. The values are then reported on a single diagram (Figure V.4) in the form of a curve that

[18] The peak amplitudes and frequencies are found by extrema search routine. An extremum is defined as the frequency where the first derivative of the spectrum is zero. Data interpolation is implemented to increase the accuracy of the peak finding procedure.

shows Ω_{Bs} as a function of $\delta l/w$. Below the curve, only one peak can be seen; above the curve, two peaks are present. When the normalized Brillouin frequency shift is below 0.65, only one peak is observed whatever the value of $\delta l/w$. It is clear that there is a threshold frequency Ω^{th} that governs the number of peaks in the spectrum and that is determined by the Length-Strength diagram (LS).

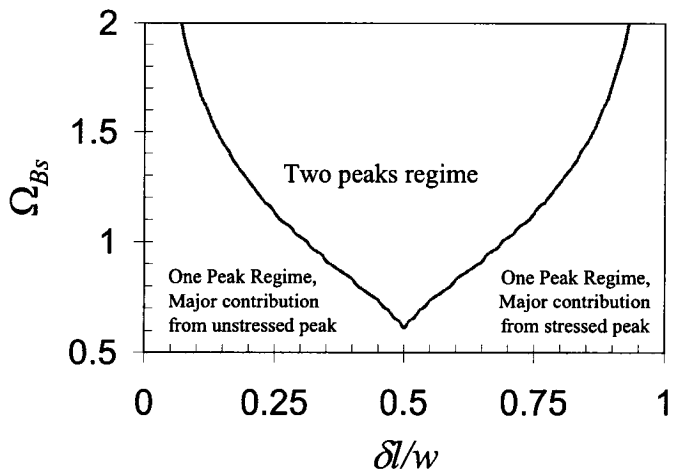

Figure V.4: Length-Strength diagram: this figure reports the normalized Brillouin frequency shift at which two peaks start to be observed as a function of $\delta l/w$. Below the curve, only one peak can be seen. Above the curve, two peaks are present. The simulation parameters are $P_{pk0} = 30$ mW, $P_{cwL} = 5$ mW, $L = 1000$ m, $z = 500$ m, $w = 20$ m (Ravet 2005a).

V.B.3. Rayleigh Equivalent Criterion

In previous section, we distinguished two frequency regimes characterized by single and two-peaks Brillouin loss spectra. We found a frequency threshold Ω^{th} that sets the border between the two regions. As long as Ω_{Bs} is very different from Ω^{th}, there is no ambiguity in finding peak frequency. This claim is not valid when $\Omega_{Bs} \approx \Omega^{th}$, because the discrimination of the two peaks requires the peak search to be very precise. Besides, experimental data are contaminated with noise. That makes it more difficult to

distinguish the two regimes. We want to introduce a practical and reproducible criterion that allows the unambiguous detection of multiple peaks and to determine the smallest resolvable frequency shift (Ω_{res}) using Rayleigh criterion (Born 1999).

Rayleigh criterion is known to be a criterion that allows the determination of the smallest resolvable frequency difference. It applies to two distributions of equal intensity whose equations have the generic shape $I = \mathrm{sinc}^2(\beta)$ where β is the normalized frequency. The criterion assumes that these two peaks can be resolved as soon as the maximum intensity of the first peak coincides with the first minimum of the second peak, which happens for $\beta = \pi$. The distance between these two peaks is then the smallest resolvable frequency difference. The minimum between the two peaks has an intensity of $8/\pi^2$.

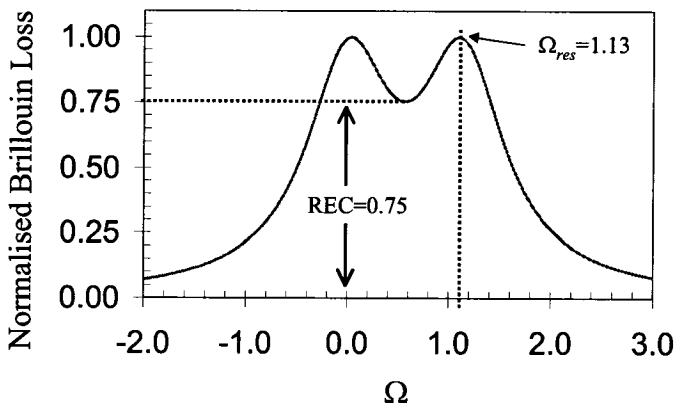

Figure V.5: Definition of the Rayleigh Equivalent Criterion for simulated Brillouin loss spectrum with the following parameters L=1000m, z=0, P_{p0}=30mW, P_{cwL}=5mW, w=20m (Ravet 2005).

Our objective is to derive an equivalent criterion that applies to Brillouin Loss Spectrum. We make the assumption that both the normalised Brillouin loss spectrum and I must have the same FWHM. If we define the normalised frequency in I to be

$\beta=\upsilon\pi\nu/\Gamma$, it is easy to find that υ =1.7718 for Brillouin spectra that are Lorentzian like. Figure V.5 shows Brillouin loss spectrum obtained by simulation of the phenomenological model. The dip amplitude (minimum of the Brillouin loss spectrum comprised between the two peaks) is 0.75 corresponding to $\Omega_{obs} = \Omega_{res} = 1.13$. We propose to define the dip amplitude as the Rayleigh Equivalent Criterion (REC).

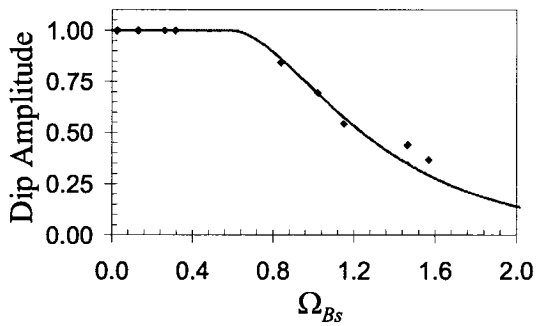

Figure V.6: Normalised Brillouin loss spectrum dip as a function of the normalised Brillouin frequency shift. Simulation results (plain curve) and experimental data (diamond), sensor settings are L = 40 m, z = 20 m, P_{pk0} = 5 mW, P_{cwL} = 3 mW, w = 0.2, ER = 11 dB, P_{cwL} = 3 mW, w = 0.2 m (Ravet 2005).

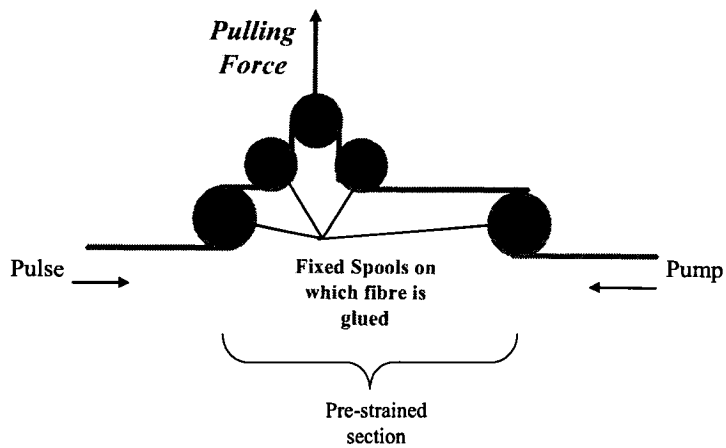

Figure V.7: Experimental set-up.

Figure V.6 also reports experimental data obtained in controlled laboratory conditions. A section of 1.5 m out of 40 m is subjected to stress by applying linearly

rising weight. The unstrained fibre Brillouin frequency is 12819.98MHz. The fibre has a strain coefficient C_ε = 0.0660 MHz/με. The induced length increase varies from 0 to 1.8 mm. The strain increase is converted into Brillouin frequency shift. Frequency scan step is 10 MHz and the scan starts at 12700MHz over a span of 500MHz. The experimental set-up is shown in figure V.7. The spectra associated with the boundary between the strained and unstrained sections were analysed. The minimum between two peaks is evaluated following the extrema search routine. Choosing simulation parameters identical to the experimental conditions, we obtain simulated data that agree with the experimental results.

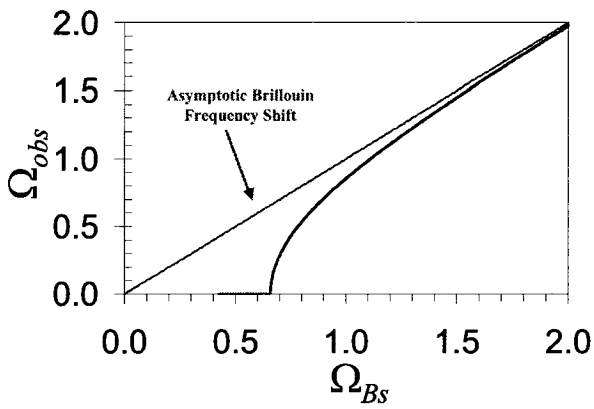

Figure V.8: Observed Brillouin frequency shift as a function of the expected Brillouin Frequency Shift (Ravet 2005a).

If the REC is helpful to discriminate two peaks, it does not state on how accurate the Brillouin frequency measurements are. In fact, the uncertainty must be quantified at this stage because the observed normalised Brillouin frequency shift (Ω_{obs}) and the actual normalised Brillouin frequency shift are not equal (Ω_{Bs}). That difference appears clearly when examining Figure V.8 where the Ω_{obs} is reported as a function of Ω_{Bs} for $\delta l/w$=0.5. The difference between Ω_{obs} and Ω_{Bs} comes from the fact that when two

Lorentzian distributions overlap, the actual peak frequencies differ from the observed ones.

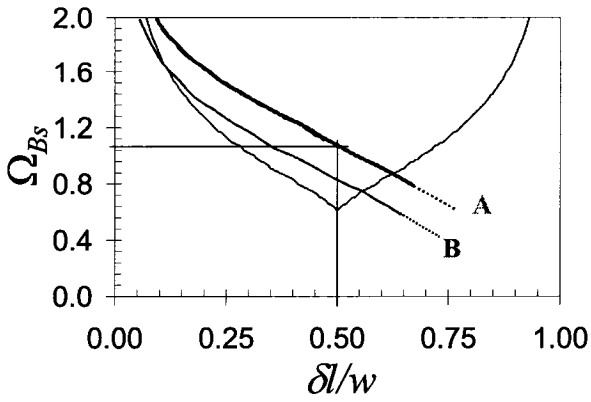

Figure V.9: This diagram reports iso-error curves (A: relative error=1%, B: relative error =5%) relating Ω_{Bs} to $\delta l/w$ for L=1000m, z=0m, P_{pk0} = 30 mW, P_{cwL} = 5 mW, w=20m (Ravet 2005a).

We conducted an analysis of the errors on determining Ω_{Bs} while measuring Ω_{obs} by introducing the relative error defined as $|(\Omega_{Bs}-\Omega_{obs})/\Omega_{Bs}|$. Results of the error analysis are summarized in Figure V.9 in the form of iso-error curves in the LS diagram. These curves relate Ω_{Bs} to $\delta l/w$ at a constant error. The analysis of figure V.8 allows us to relate Ω_{res}=1.13, found with the REC=0.75, to the Relative Error. When $\Omega_{Bs}=\Omega_{res}$, the relative error is about 1% and corresponds to the case $\delta l/w$=0.5. Clearly, by introducing the REC, the minimum spatially resolvable stress section has been reduced to $w/2$ instead of w with a Brillouin Frequency uncertainty of about 1%. We see that the minimum measurable strain length is smaller than w. The REC is an efficient threshold to unambiguously detect stress less than spatial resolution with an uncertainty lower than 1%. Smaller stress length can be achieved with larger error. For instance, a stressed

section whose length is $\delta l/w \approx 0.3$ can be detected with an error on the Brillouin frequency of 5% (curve B).

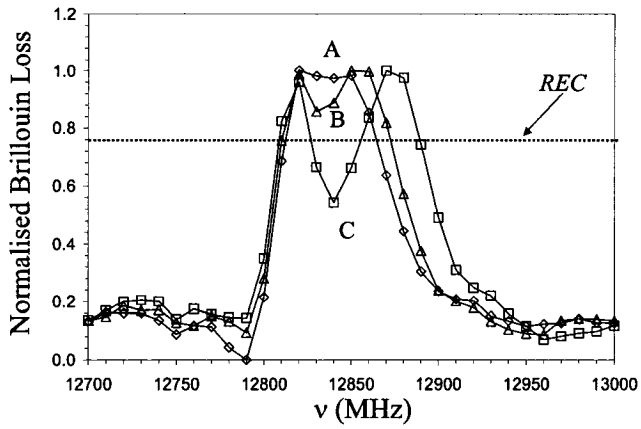

Figure V.10: Experimental Brillouin loss spectra measured at 20m at the boundary between the strained and unstrained sections for three strain values (A: 510με; B: 638 με; C: 893 με) (Ravet 2005).

Figure V.10 illustrates how the REC can be used in measuring stresses that are shorter than the spatial resolution. These spectra come from the same experiment that illustrates the REC dependence against the normalised Brillouin frequency shift. The discussion focuses on the location at the boundary between the strained and unstrained sections. Profiles A (510 με) and B (638 με) show that the pulse covers more than one stress. According to the REC they are not distinguishable. Note that spectrum B clearly experiences two peaks and then the stress could be measured but an uncertainty much larger than 5% must be expected. The same criterion states that Spectrum C (893 με) has a stressed section that can be clearly identified and measured, with an error much lower than 1%. The stressed contribution frequency is estimated to be 12873.33 MHz when the peak frequency is measured. The frequency shift associated with a strain of

893με is actually12878.90 MHz. Also the location accuracy has been reduced to ½ of the pulse length.

V.B.4. Form Factors

When two peaks can not be resolved according to the REC (i.e. the spectrum lies in the single peak region of the LS diagram), further analysis of the spectrum shape can be carried out and then useful information deduced. That is possible by introducing two form factors, asymmetric (F_A) and broadening (F_B) Factors that describe the distortion of single peak spectrum (Ravet 2006). The form factors are defined as

$$F_A = \frac{\Gamma_+}{\Gamma_-} \tag{V.1.a}$$

$$F_B = \frac{\Gamma_s}{\Gamma} \tag{V.1.b}$$

where F_A is the asymmetric factor and F_B the broadening factors, Γ_+ is the half width at half maximum of the right side of the spectrum, Γ_- is the half width at half maximum of the left side of the spectrum and Γ_s is the FWHM of the stressed fibre spectrum. Brillouin loss spectra measured at each location are analysed to extract these three parameters as illustrated in Figure V.11.

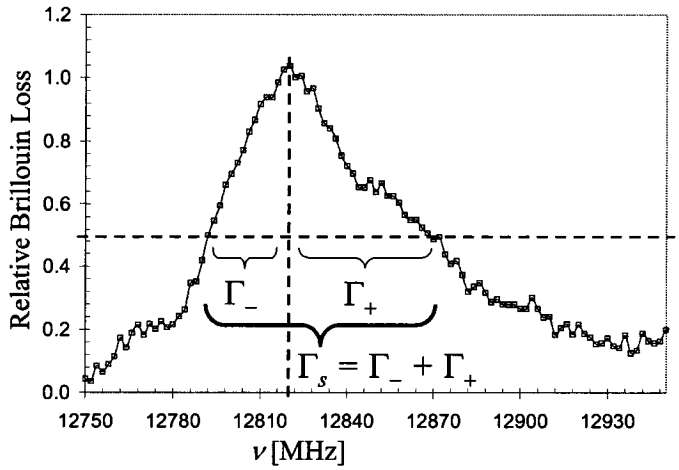

Figure V.11: Definition of the width parameters on an experimental Brillouin loss spectrum of a strained section of a single-mode optical fibre (Ravet 2006).

The asymmetric parameter, F_A, indicates the presence of large but short strain components. F_B describes the broadening of the Brillouin loss spectrum induced by non-uniform strain distribution. Let us discuss various strain regimes associated with the form factors value. Figure V.12 shows various cases with the same peak frequency but different strain distributions. When F_A =1 and F_B =1, the strain distribution is uniform. The spectrum is simply shifted and a peak finding approach is enough to characterize the status of the structure (Figure V.12.(a)). If the spectrum is still symmetric (F_A =1) but F_B >1, then the distribution is non-uniform (Naruse 2002). Peak finding technique describes the global behaviour of the structure but it fails to detect the presence of strain over section shorter than the pulse-width. The strain distribution becomes asymmetric when $F_A \neq 1$ as shown in Figure V.12.(b), which is an indication that the strain distribution is non-linear (Naruse 2003). For F_A >1, the strain distribution is non-uniform over the pulse length: a short length strain component, whose amplitude is large, and, a long strain component, whose amplitude is small, are covered by the pulse. In other words, the spectrum presents a broadening happening on the right of the

peak frequency. It indicates that small defects inducing large strain start to build up in the structure. In the case of F_A <1, a strain component, whose amplitude is large, is longer than the weaker strain components. When *FA* value becomes smaller than unity, strains induced by local defects are expanding and becoming the dominant contribution to the spectrum asymmetry. It means that the structure is in jeopardy because the defect starts to expand. Apparently, the use of F_A and F_B introduces two advantages: 1) even if the peak Brillouin frequency is the same, they show distinct stress distribution; 2) it provides a complete picture compared to average strain detection or peak analysis (when only distorted spectrum is measured). An example of data analysis based on the form factor only is presented in Chapter VI. More recently, a study based the form factor analysis has been carried out. The approach allowed the detection of

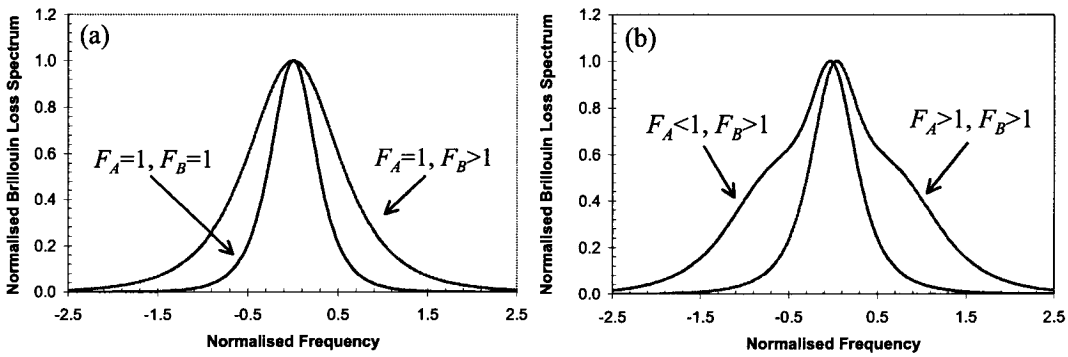

Figure V.12: Normalised Brillouin loss spectrum for various strain profiles included within *w*: (a) uniform strain (F_A=1, F_B=1), linear strain (F_A=1, F_B>1); (b) non-linear strain with short components whose amplitudes are larger than the main strain contribution (F_A>1, F_B>1), non-linear strain with short components whose amplitudes are smaller than the main strain contribution (F_A<1, F_B>1) (Ravet 2006).

V.C. Application of the phenomenological model for data analysis

V.C.1. Proposed methodology

We want to implement the phenomenological model in a spectrum reconstruction scheme where the spatial distribution of ν_B is unknown. This approach is efficient if the

spatial profile of ν_B is known in advance and then useful for theoretical discussions as it accounts for any change in the sensor settings. We propose to extract that information from a careful analysis of the spectrum shape using the tools introduced in section V.B. The first step would consist in determining to what part of the LS diagram the spectrum belongs. As mentioned, two types of spectrum shape are observed depending on the Brillouin frequency difference between stressed and unstressed components, as well as stressed section length. One type of spectrum has a single distorted peak which is broadened and asymmetric in most of the cases. The other type of spectrum has two peaks. Because the spectrum type is a function of Ω_{Bs} and $\delta l/w$, the classification in these two categories according to their dependence in stress value and length can be done as illustrated in Figure V.13 by the LS diagram. There is a clear border (shown as a line in Figure V.13.(a)) between the region where a single distorted peak is present (Figure V.13. (b)) and the region where two peaks can be identified (Figure V.13. (c)). The profile is then influenced by stress length and amplitude.

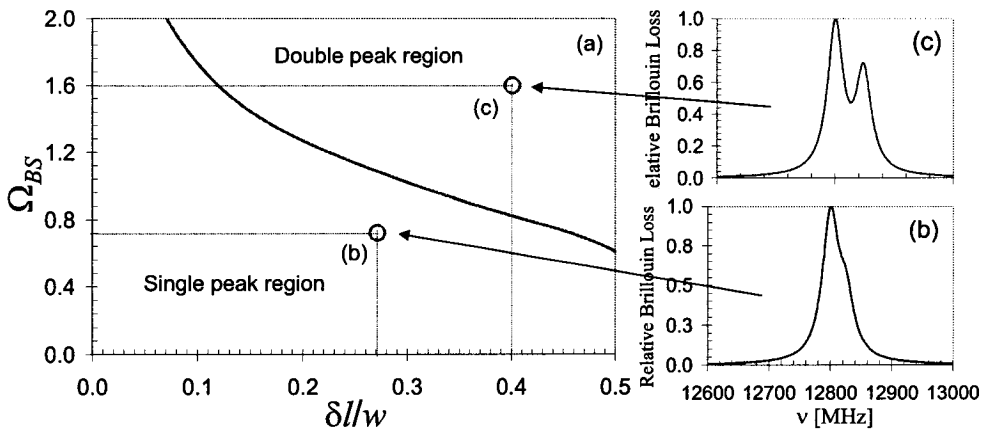

Figure V.13: (a) Length-Stress diagram for non-uniform Brillouin frequency over pulse length: the continuous line is the border between (b) single peak spectrum ($\delta l/w$ = 0.28, Ω_{Bs} = 0.72) and (c) two peaks spectrum ($\delta l/w$ = 0.40, Ω_{Bs} = 1.60). Simulation parameters are P_{pk0} = 10 mW, P_{cwL} = 8 mW, L = 100 m, w = 1 m, ER < 20 dB (Ravet 2005c).

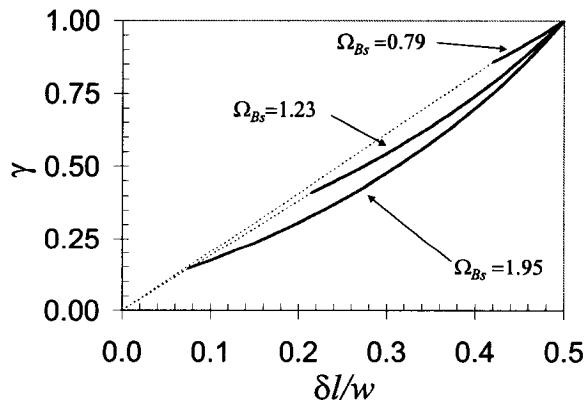

Figure V.14: Relative peak height of a stressed section as a function of the normalized stressed section length and Brillouin frequency shift. The solid line is the peak height when two peaks can be observed in the spectrum (all these points are in the double peak region of the LS diagram). The dotted line is a linear extrapolation of the stressed section peak height when the stressed contribution is buried in the single peak spectrum (all these points are in the single peak region of the LS diagram). Simulation parameters: P_{pk0} = 10 mW, P_{cwL} = 8 mW, L=100m, w=1m, ER<20dB (Ravet 2006c).

When two peaks are clearly identified, as shown on the spectrum of Figure V.13.(c), stressed section length and amplitude are translated respectively in relative peak height, γ (as in Figure V.3), and peak frequency. The relationship between γ, Ω_{Bs} and $\delta l/w$ is shown in Figure V.14. Handling multiple integrations at each position, as the phenomenological model would require, is not necessary. Instead we propose to calculate G_T (equation IV.16), assuming that g is constant over w but composite i.e. g at z is a linear combination of Lorentzian shape distributions defined as

$$g(\nu,z)=\frac{1}{N(z)}\sum_{i=1}^{N(z)}\frac{\gamma_i(z)g_B}{\left(2\frac{\nu_i(z)-\nu}{\Delta\nu_B}\right)^2+1}, \qquad \text{(V.2)}$$

where γ_i is the height and ν_i the peak frequency of the i^{th} peak in spectrum, N is the number of peaks. As it appears in equation V.2, γ_i, ν_i and N depend on the location in

the fibre. The combination of these parameters is unique as it is based on the analysis of the spectrum shape, as it will appear in the following sections.

When the Brillouin spectrum is composed of multiple peaks, the present signal processing approach does not require to know the exact relationship between γ and $\delta l/w$ as shown in Figure V.14. Here we would implement a peak search routine and associate each detected maximum with a pair (γ_i,ν_i). Near the borderline as defined in Figure V.13, the distinction between single and double peak is not always unambiguous, particularly when the experimental data are contaminated with noise. To overcome that difficulty we use the Rayleigh Equivalent Criterion (REC) introduced in section III.C. It states that two peaks are resolved if the minimum between two apparent maxima is lower than 75% of the lowest of the two peaks. We will use this criterion to separate the single peak region from the double peak region without ambiguity.

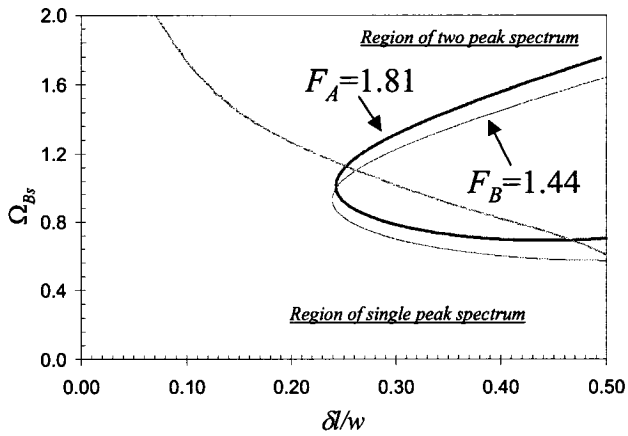

Figure V.15: Iso-form factor curves in Length-Stress diagram (LS) for non-uniform Brillouin frequency over pulse length; the continuous line is the border between single peak and two peak spectra. Simulation parameters are P_{pk0}= 10 mW, P_{cwL} = 8 mW, L=100m, w=1m, ER<20dB (Ravet 2006a).

In the two peaks region, the identification of the various components is easier and the pair (γ_i,ν_i), (i=1,2), are determined without ambiguity, being the height and the

frequency of the detected peak. When the spectrum only experiences one but distorted peak as shown in Figure V.13.(b), the estimation of (γ_i,ν_i), (i=1,2), is more complicated. It is clear that in that case, the spectrum appears broadened and asymmetric. We propose to take advantage of that spectrum distortion with the help of the two form factors, F_A and F_B, introduced in section V.B.4, because these parameters are a measure of the strain amplitude and the strained section length. They can be used to extract the useful information from the spectrum i.e. the strain amplitude and the strained section length. We generated curves of constant form factors on the LS diagram for various practical sensing cases. They are also named iso-form factor curves, and more specifically, these curves are of two types: iso-FA (IF_A) and iso-FB (IF_B). Each of these curves drawn in a LS diagram is composed of two branches as shown in Figure V.15. Curve fitting shows that the upper branch behaves as an arc of hyperbola while the lower branch is similar to an arc of ellipse. The intersection between one IF_A and one IF_B gives a couple ($\delta l/w$, Ω_{Bs}) from which the two Brillouin frequencies and the respective stressed section length can be extracted. In order to use the composite gain $g(\nu,z)$ with the reconstruction model, we need to convert $\delta l/w$ into γ. The relationship between $\delta l/w$ and γ is not known when the spectrum has a single peak as it appears in Figure V.14. Nevertheless, Figure V.14 can be used to extrapolate that relationship. We make three assumptions: 1) γ must increase monotonically with $\delta l/w$; 2) γ=0 when $\delta l/w$ =0; 3) the transition from one to two peaks is continuous so that γ varies continuously with $\delta l/w$. We simply suppose that γ is proportional to $\delta l/w$. After Figure V.12, the proportionality coefficient, a, varies with Ω_{Bs} and is not significantly affected by other sensor parameters. We computed γ as a function of $\delta l/w$ for $\Delta\nu_s = \Omega_{Bs}\Gamma$ varying from 10MHz

to 80 MHz. We obtain a large set of curves that are extrapolated linearly as shown in Figure V.14 (dotted lines) and according to assumptions 1) to 3). Applying curve fitting to the numerical values of a ($R^2 = 0.8577$), we derived the following expression

$$a = 1.9 + \frac{0.1}{1 + \exp\left[\frac{\Delta\nu_s - 33.8}{1.8}\right]} \tag{V.3}$$

where $\Delta\nu_s$ is expressed in MHz. Equation (V.3) is plotted in Figure V.16. For $\Omega_{Bs} \leq 1$, we have $a \approx 2$, which represent most of the practical cases we encountered.

Once ν_1 of the peak is determined by the extrema search routine, and, the couple ($\delta l/w$, Ω_{Bs}) found by searching the intersection of IF_A and IF_B, we can calculate $\nu_2=\nu_1+\Delta\nu_s$, $\gamma_1=a(1-\delta l/w)$ and $\gamma_2=a\delta l/w$. These values can then be used by equation (V.2) which in turn is used in the model to reconstruct the composite spectrum.

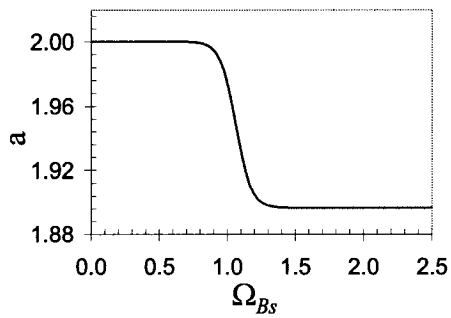

Figure V.16: Coefficient of proportionality between $\delta l/w$ and γ. Simulation parameters are P_{pk0} = 10 mW, P_{cwL} = 8 mW, L=100m, w=1m (Ravet 2006c).

Any practical implementation of the DBS require a calibration step. Strain being proportional to the variation of the Brillouin frequency, it is important to know its distribution all along the unstressed fibre. Moreover, the signal processing approach implies that Γ is known as a function of position. Once the fibre is laid on the structure, a measurement over the frequency range of interest is carried out to set a baseline of ν_B

and Γ. These values will then be used to detect any changes in the spectrum shape when the structure is stressed.

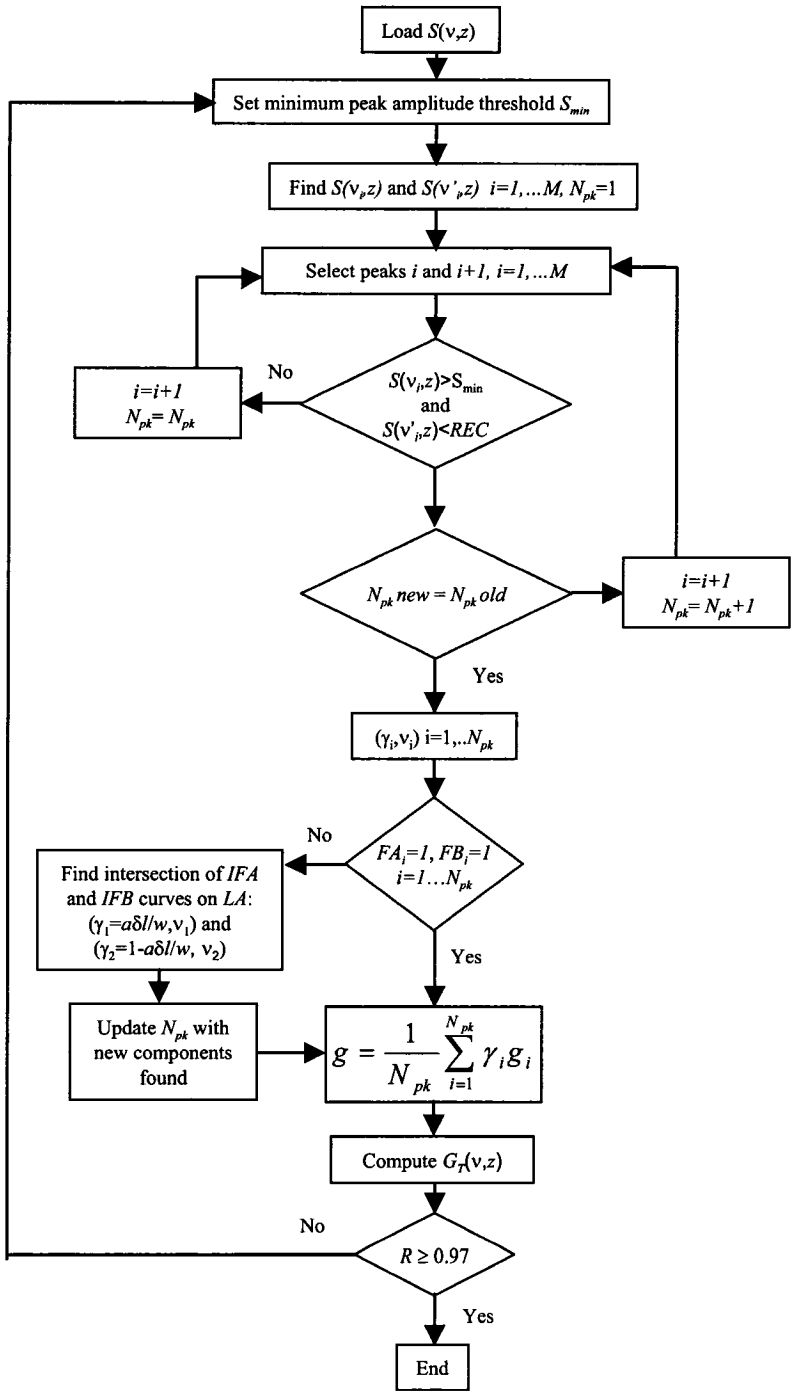

Figure V.17: Flowchart of the spectrum reconstruction procedure (Ravet 2006c).

Figure V.17 is a flowchart representing the various steps used to reconstruct the spectrum from experimental data. At a given position, we normalize the measured spectrum and then apply a filter to smooth the noise of the measured spectrum $S(\nu,z)$. We then set a threshold to the smallest peak detected that will be kept. An extrema search routine is applied to find all the peaks (γ_i,ν_i), $(i=1...M)$, and the minimum between two adjacent peaks (γ'_i,ν'_i). γ'_i and ν'_i are defined respectively as the amplitude and the frequency of the minimum between peaks i and $i+1$. The detected extrema are then subjected to a test: the amplitude of the maximum i must be larger than the peak threshold to be counted as a peak; the minimum must be lower than the *REC* criterion to have maxima i and $i+1$ counted as peaks. We then have a first set of (γ_i,ν_i), $(i=1...N_{pk})$. We now analyze the shape of each peak by estimating their *FA* and *FB*. Every time *FA* and *FB* are different from 1, the intersection of *IFA* and *IFB* must be calculated and the corresponding $(\gamma_1=a(1-\delta l/w),\ \nu_1)$ and $(\gamma_2=a\delta l/w,\ \nu_2)$ estimated increasing the total number of peaks (N_{pk} is updated). Equations (IV.16) and (V.2) are then used to build the composite spectrum that is fed into the model. The reconstructed Brillouin loss spectrum is compared to the measured spectrum by computing the correlation coefficient (Press 1999) defined as

$$R=\frac{\sum_{i=1}^{N_d}\{S(\nu_i,z)-\langle S(z)\rangle\}\{G_T(\nu_i,z)-\langle G_T(z)\rangle\}}{\sqrt{\sum_{i=1}^{N_d}\{S(\nu_i,z)-\langle S(z)\rangle\}^2}\sqrt{\sum_{i=1}^{N_d}\{G_T(\nu_i,z)-\langle G_T(z)\rangle\}^2}} \qquad \text{(V.4)}$$

where N_d is the number of measured data in the spectrum and the angular brackets refer to the average of the spectrum, measured or reconstructed, over the sample size. When $R = 1$, measured and reconstructed spectra match exactly and a diagram reporting $S(\nu,z)$

vs. and $G_T(\nu,z)$ would be aligned on a straight line whose coefficient is 1 and intercepting the origin. Pseudo-Voigt distribution curve fitting (DeMerchant 2000) on Brillouin spectra using the Levenberg-Marquhardt algorithm (Press 1999) normally requires that the correlation coefficient for the pseudo-Voigt distribution R_{pV} is larger than 0.97. We then expect that the reconstructed spectra using our signal processing approach should definitely give R values larger than 0.97. As a consequence, if $R \geq 0.97$, the routine ends the reconstruction of the spectrum at that location and starts to analyze the experimental profile of the next position. If $R<0.97$, the minimum peak amplitude threshold is decreased to account for peaks that were neglected in the previous reconstruction. The whole process is then repeated until $R \geq 0.97$.

Typically, the processing time for the reconstruction of spectra extending from 10750 to 11000MHz with a frequency step size of 4 MHz, and, acquired every 40 cm on a 2 km long single-mode fibre, is less than 5 minutes with a standard desktop computer (Intel Celeron processor, 847 MHz, 256 MB of RAM).

Because our approach uses a peak finding technique based on an extrema search routine, it can be argued that multiple distribution fitting can yield more accurate peak frequencies as suggested by Fig. V.8. Nevertheless such approach requires that the number of stress components building the spectrum is known in advance. Multiple trials are needed to obtain that information. That contributes to increase the processing time, which is not the case with our approach. In fact, distortions of the spectrum that are actually due to the sensor settings can wrongly be interpreted as additional stress components. With our approach, the spectrum shape is first determined by the sensor settings. Any difference between loose and stressed fibres spectra can then be attributed

to the occurrence of an event as the sensor parameters are accounted for. The peak finding method is then faster. Moreover, the use of the REC criterion guarantees that the errors are lower than 2% (Fig. V.9), which is acceptable for applications were fault detection is critical.

V.C.2. Application to experimental data

This signal processing approach was applied to the strain experiment presented in section V.B.3 (Figure V.7). Note that the same experiment has served to illustrate the implementation of the REC in a practical situation.

Figure V.18 shows three measured Brillouin profiles for distinct load conditions (Figure V.18 (a), (c), (e)) and their computed profiles (Figure V.18 (b), (d), (f)) reconstructed with the phenomenological model. Both measured and reconstructed profiles show a variation of the Brillouin frequency versus position. The reconstructed profiles match well with the measured data. As shown by Figure V.18 (a) and (b), the sensing fibre and the various patchcords have exactly the same Brillouin frequency (excepted for a short section at the beginning of the fibre). As it can be observed a 10 m long segment is subjected to a constant load inducing a permanent pre-strained condition equivalent to frequency shift of 20 MHz from the loose fibre Brillouin frequency at 23°C (12794 MHz). A section 1.5m long out of the pre-strained segment is gradually stressed. The effect of the load increase is evident in Figure V.18 (c) and (d) where a distortion of the profile at the beginning of the pre-strained section is visible. This distortion appears to be similar in both measured and reconstructed profiles. In this case the load applied is not large enough to isolate the stressed section from the pre-strained fibre. This is not

the case for Figure V.18 (e) and (f). The load is such that the profile transition from the pre-strained fibre to stressed section is abrupt.

Figures V.19 and 20 show four measured Brillouin spectra and their respective reconstructed profiles. These spectra are measured at the same location, for different ε, in the transition region between the stressed and the pre-strained sections. It is clear that the reconstructed profiles match well the measured data (note that the correlation coefficient R between measured and reconstructed profiles is larger than 0.97. Figure V.19(a) is the unstressed case and single peak reconstruction is successful (R = 0.9889). Note that the pseudo-Voigt has a lower correlation parameter (R_{pV} = 0.9814). Figure V.19(b) still lies in the single peak region and appears lightly distorted. We have to compute the *IFA* and *IFB* from the experimental spectrum and extract the relevant hidden strain information from LS diagram embedded in the Fig. V.19(b): $\Delta\nu \approx$ 19.75 MHz, $\delta l \approx$ 0.34 cm, R = 0.9916. Here too, R_{pV} = 0.9780 < R. The effect of the load increase becomes evident in Fig. V.20(a) where a distortion of the measured profile is obvious. Analysis of *IFA* and *IFB* suggests that the strain condition is such that the spectrum must be at the edge of the single peak region. That is what the reconstructed profile states as a very small peak on the right part of the distribution is visible. The Form Factor analysis give $\Delta\nu \approx$ 29.41 MHz and $\delta l \approx$ 0.34 cm, and R = 0.9922 (R_{pV} = 0.9796). Finally, two peaks are clearly distinguishable in Fig. V.20(b). We find that $\Delta\nu \approx$ 75.08 MHz, $\delta l \approx$ 0.34 cm, R = 0.9946 (R_{pV} = 0.9880).

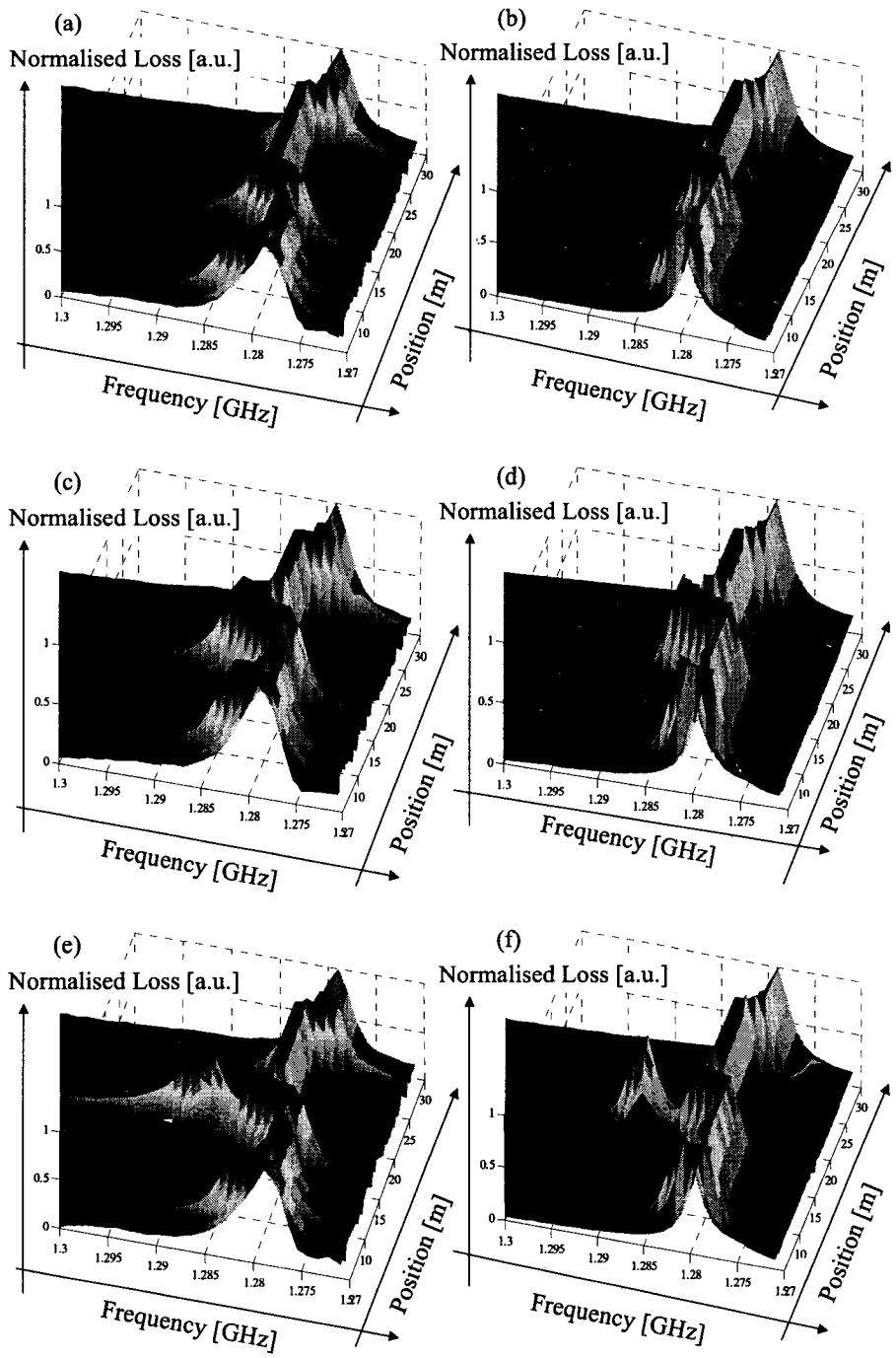

Figure V.18: Measured (a, c, e) and reconstructed (b, d, f) Brillouin loss profiles of a 40 m long optical fibre. A 10m section has been pre-strained. A load is gradually applied to 1.5m of pre-strained section. Measurement and computation parameters are P_{pk0} = 10 mW, P_{cwL} = 4 mW, L = 40 m, ER=25 dB, $\Delta\tau$ = 2 ns. Applied strain varies from $\varepsilon' = 0$ με (a,b) to $\varepsilon' = 458$ με (c,d) and then $\varepsilon' = 1138$ με (e,f). Normalised loss ranges from 0 to 1. Frequency ranges from 12700MHz to 13000MHz. Position (z) ranges from 5 to 30m.

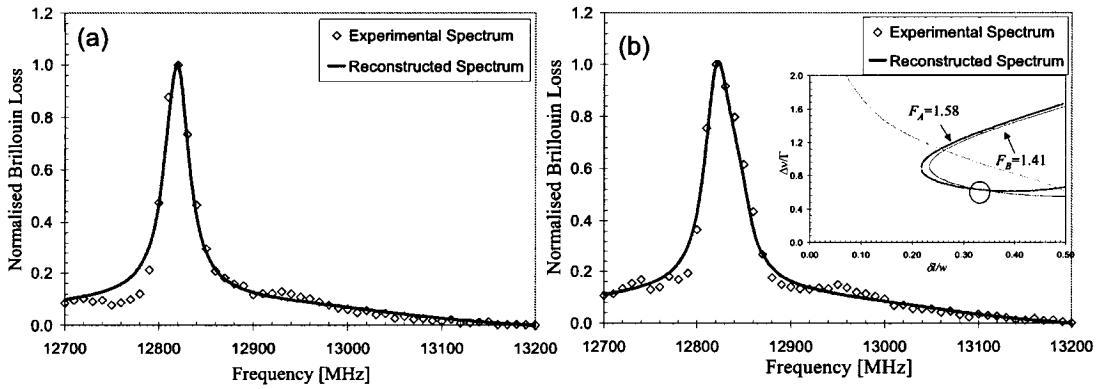

Figure V.19: Measured and reconstructed Brillouin loss spectrum for L = 40m and z = 16 m; measurement and computation parameters are P_{pk0} = 10 mW, P_{cwL} = 7.8 mW, ER =25dB, $\Delta\nu_B$ = 45 MHz, w = 20 cm; applied strain are 0 με (a) and 303 με (b) (Ravet 2006c).

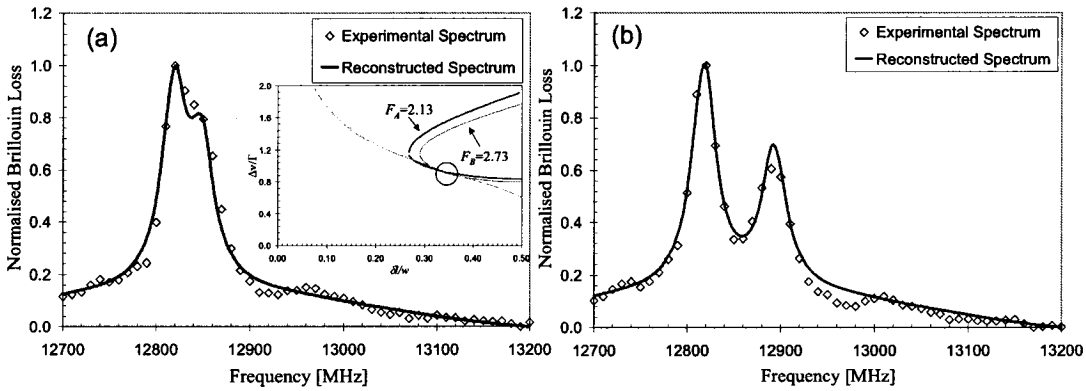

Figure V.20: Measured and reconstructed Brillouin loss spectrum for L = 40 m and z = 16 m; measurement and computation parameters are P_{pk0} = 10 mW, P_{cwL} = 7.8 mW, ER = 25 dB, $\Delta\nu_B$= 45 MHz, w = 20 cm; applied strain are 452 με (a) and 1138 με (b) (Ravet 2006c).

V.D. Summary

A signal processing method was discussed. The method combines a careful spectrum shape analysis to evaluate the best initial conditions, and, the phenomenological model that simulates the sensor operation. A set of tools has been developed to facilitate the spectrum shape analysis. These are the length-strength diagram, the Rayleigh Equivalent criterion and the form factor. The approach has been validated by comparing its results with experiments and exact solutions of the three wave equations for SBS. This model is implemented in a signal processing scheme that

has been applied to experimental data obtained under well-controlled laboratory conditions. The agreement is good and reflects the Brillouin frequency shifts induced by strain applied to the fibre. The approach is also successful to extract strain components hidden in distorted single peak spectrum. Another advantage lies in its analysis speed. Only a few minutes are required to analyse a whole fibre with a standard desktop computer.

Chapter VI: Application to the monitoring of structures subjected to heavy loads

VI.A. Introduction

Recent studies (Zeng 2002, Murayama 2003) have been conducted to monitor global strain of composite and concrete beams under limited load, i.e. the structure responds to the load linearly. Average strain was measured while global strain was tracked. The extraction of average strain used single peak fitting and/or centroid method (Horiguchi 1995, Zeng 2002, Murayama 2003, De Merchant 1999, Bao 2001). If the Brillouin peak has a symmetric shape, then average strain reflects the overall structure condition, which is the case when the structure is made of homogeneous material such as steel or plastic and is stressed under elastic conditions (De Merchant 1999, Bao 2001). Global and local strains are related to each other linearly, so that the structure does not suffer deformation or crack.

However, when civil engineering structures are subjected to substantial load, structures start to fail, so de-bonding of fibre reinforced polymer (FRP) from concrete, deformation, buckling and cracks are formed. Within such a non-uniform strain regime, Brillouin profile becomes strongly distorted, e..g. asymmetric and broadened with FWHM much bigger than the natural Brillouin linewidth. Brillouin peak frequency does not match mass-weight centre of the spectrum (in other words, average strain value). In this case, peak frequency measurement only gives global strain information, which does not reflect special and local defects such as cracks as well as FRP/concrete de-bonding or pipeline buckling. To identify the early signatures of these structural failures, we

need to know both local and global strain information. The average strain is not enough to provide the full picture of the structure condition for the purpose of structural health monitoring.

Based on this limitation, we propose to use two complementary data analysis approaches, applying to non-uniform strain distributions. The decision to apply one or the other is driven by the structure of the measured spectra. In the one hand, if the spectrum is composed of many but well resolved peaks, the phenomenological model in combination with multiple-peak fitting is used. In the other hand, when the peaks are not well resolved, or, when the spectrum is a broad and asymmetric distribution, the method based on form factors is preferred. The decision taking must be unambiguous and lead to repeatable results. In the previous chapter, we introduced the Rayleigh Equivalent Criterion (REC) achieving that objective by determining if the many peaks can be resolved (Ravet 2005). In this chapter, we present the implementation of these two approaches, each of them in distinct practical situations.

The first study cases are the monitoring of distribution (Ravet 2005b, Ravet 2006b) and transmission pipes (Zou 2006, Ravet 2007) under extreme load conditions. The transmission pipe was subjected to axial and bending loads in order to provoke the buckling. Such experiment simulates the stresses that a pipe suffers when soil motion and large pipe internal pressure act together (Einsfeld 2003, Palmer 2003). The locations of pipe-wall buckling are found by measuring the axial strain distributions along the outer surface of the pipe. In the distribution pipe study, vertical load only was applied to the structure. Buckling occurred in that case without exerting a bending load. Instead the inner wall was locally thinned to create a weakness that would trigger the buckling. In both cases, buckling leads to the apparition of distinct strain components

over the pulse length. Those components lead generally to multiple peaks Brillouin spectra at the buckling location. It is then convenient to take advantage of the REC to resolve the various peaks and apply the phenomenological approach.

We conducted another monitoring experiment on a concrete column strengthened with fibre reinforced polymer sheets (Ozbakkaloglu 2007, Ravet 2006, Ravet 2007). The column was subjected to an axial load while successively bended back- and forward with increasing loads, simulating seismic induced stress conditions. Here, material structure plays a key role in the signal processing approach selection. In steel pipes, the lack of uniformity or homogeneity are structural defects. For a concrete/FRP column, the structure is non uniform and inhomogeneous by construction. Even a light stress would induce quite a large Brillouin spectrum distortion. The spectra would appear asymmetric and broadened. The form factor approach is then the method of choice to analyse the structure behaviour. We see that our sensor system is not only capable of measuring deformation of the structure. It also gives enough informations so that engineers can correlate the readings with the applied stresses and deduce the possible de-bonding of the FRP and concrete as well as the crack conditions.

VI.B. Monitoring of distribution pipe buckling

VI.B.1. Experiment description

The tested specimen was a steel pipe of 1 m with a diameter of 18cm and square end caps (20cm side length). The location of buckling was controlled by thinning a small area of the specimen inner wall at the mid-length, which induced weakness in the structure for buckling to occur at this region when an axial load was applied. Moreover

the test bench was designed to only exert vertical forces. The sensor characteristics and set-up are presented in section IV.B. Typical data acquisition time is 10 minutes.

The specimen was instrumented with strain gauges and distributed Brillouin sensor. Figure VI.1.(a) shows the location of the fibres and strain gauges. The fibre was looped 8 times on the pipeline with 1m loose fibre separations. In order to avoid irregularities, the specimen surface was smoothed by using sandpaper. The fibres were attached to the prepared surface using a professional construction glue requiring three hours drying. The strain gauges are distributed symmetrically about the mid-length of the specimen.

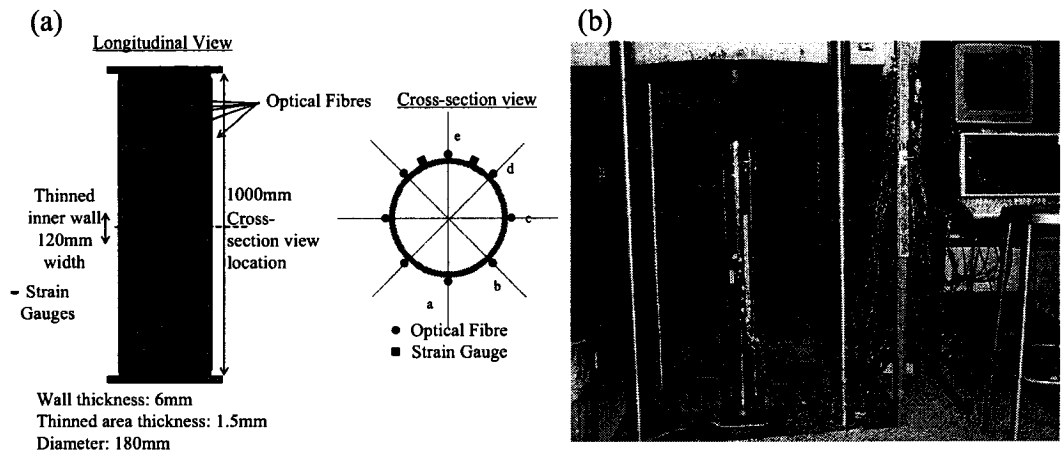

Figure VI.1: (a) Pipe specimen and sensors layout. (b) Instrumented pipe in the test bench (Ravet 2006b)

Once placed on the test bench (Figure VI.1.(b)), the pipeline was subjected to a gradual load increase from 0 to 730kN. The buckling happened after 730kN and the fibre was broken due to the small bending radius and rigid glue (Figure VI.2). At the same time as the pipe was compressed, the deformations were continuously monitored with the strain gauges and the DBS. The experiment was finished when the buckling

happened, which is a very fast phenomenon when the steel starts to yield. The buckling could be visually observed as illustrated by Figure VI.2.

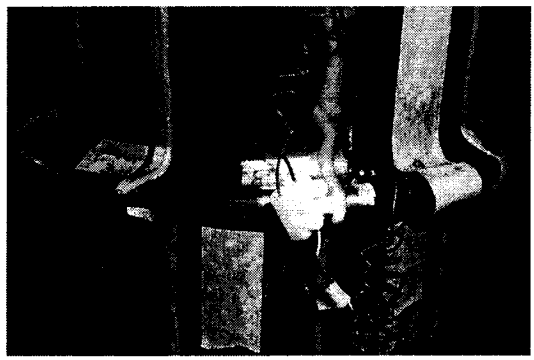

Figure VI.2: Buckling of the pipeline. The deformation was obviously identified after the load was increased over 700kN (Ravet 2006b).

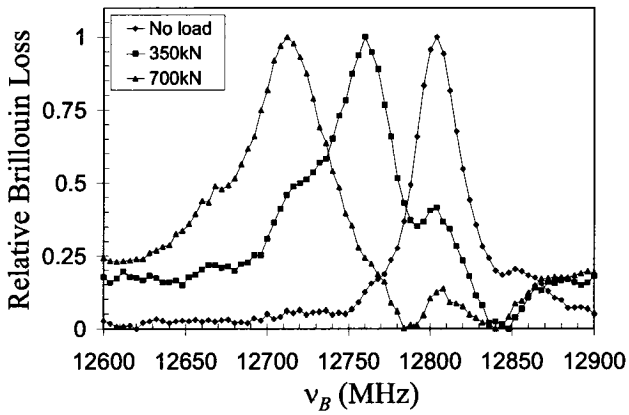

Figure VI.3: Brillouin Loss Spectra for three distinct loads measured at 350 mm from the beginning of glued section c. The main peak is downshifted in frequency indicating that the pipe is compressed (Ravet 2006b).

VI.B.2. Measurement results and analysis

Two load levels (350 and 700kN) were kept constant for less than 15 minutes in order to capture the Brillouin spectra distributions along the whole fibre and over a frequency range broad enough to capture all possible strain components. Figure VI.3 represents the Brillouin loss spectra measured in section c. The three curves show the

effect of the load increase: without load the Brillouin peak located at 12805MHz is higher than the loose fibre Brillouin frequency. That is induced by the combination of small stresses during the fibre installation and the drying of the glue. The peak frequency at 350kN configuration is downshifted from 12805MHz to 12760MHz corresponding to -548 με. The peak frequency is further reduced when 700kN is reached giving a compression of -1390 με. The axial load to the structure causes this compression.

Pipe compression is confirmed by strain gauge, and comparison between strain gauge and the Brillouin sensor measurements are shown in Figure VI.4.(a) and (b) for various strips along the pipeline at 350 kN and 700 kN. Strain gauge readings and Brillouin sensor measurements appear to lie in the same strain range for a given load. In addition, the results indicate a consistent behaviour when the load increases from 350 kN to 700 kN. Material non-uniformity along hoop and axial directions are other interesting features observed in Figure VI.4. More specifically, in the axial direction, it appears from Figure VI.4.(b) that curves e and d represent increased and decreased compression, respectively, while sections a, b, and c have a uniform compressive strain. The maximum compression is measured at 800 mm. Apparently this process is not due to wall thinning as the location is different. It is rather due to material non-uniformity enhanced by heavy loading. Material non-uniformity in the hoop direction is also evident when considering the DBS measurements and strain gauge readings at a fixed position. The largest strain variation happens in the region comprised between fibre section c and e. It is in the same region that the strain gauges are laid and show that their readings are comprised between DBS measurements on fibres d and e. The fact that

these values are not matching exactly is not unexpected. It accounts for two reasons. First, the material non-uniformity can be invoked because all the measured values, obtained with strain gauges and DBS, show a monotonic transition from section d to e. Second, Figure VI.3 reveals that the spectra measured on the stressed pipe are broadened and asymmetric. This is not a surprise as the spatial resolution is 15 cm. As the induced strain by a heavy load is rarely uniform, the DBS detects the average strain while the strain gauges measure localised strain.

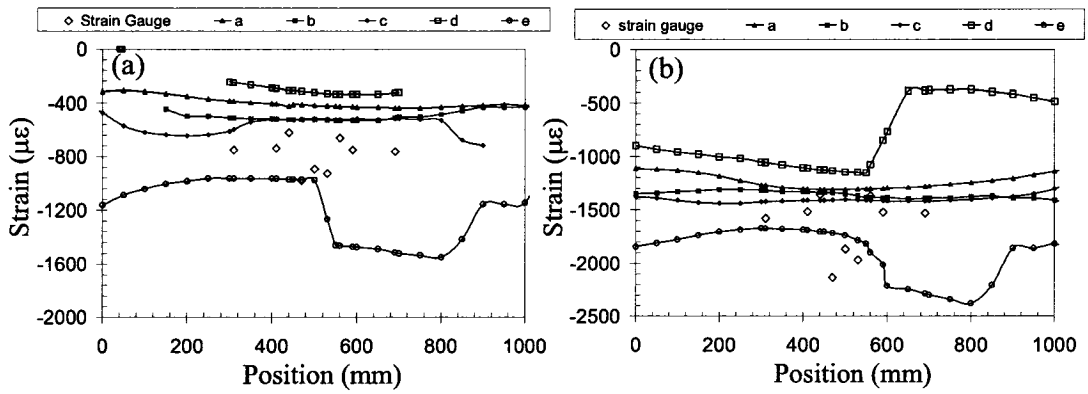

Figure VI.4: Pipeline Strain profiles obtained by Brillouin sensor and strain gauges measurement for (a) the 350 kN load applied and (b) the700kN load applied. Labels a, b, c, d and e report the measurements obtained with the Brillouin sensor on fibers a, b, c, d and e (Ravet 2006b).

Compression is not the only effect that we detected with the DBS. In fact, we noticed the presence of a second peak in the Brillouin spectrum, which has a lower relative peak power (30% and smaller) than the highest peak associated with compression. It means that this smaller peak comes from a strained section within the pulse width that is shorter than the major contribution, due to compression. Resulting compressive and tensile strain profiles in Figures VI.4 and 5, respectively, show the variations of these two strain components. Elongation increases as the applied load is raised as shown by the strain profiles in Figure VI.5. We interpret such behaviour as a

signature of the buckling formation. We have two confirmation of this intuition. First, the location of the highest strain value suggests that it lies in the thinned wall region. Second, the location also coincides with the buckling position estimated by visual inspection (Figure VI.2). The whole pipeline suffers compression but a tiny part, axially distributed, must be extruded to elongate locally. At that stage of the experiment, the deformation is still too small to be seen visually, but can be felt by pressing the hand on the surface.

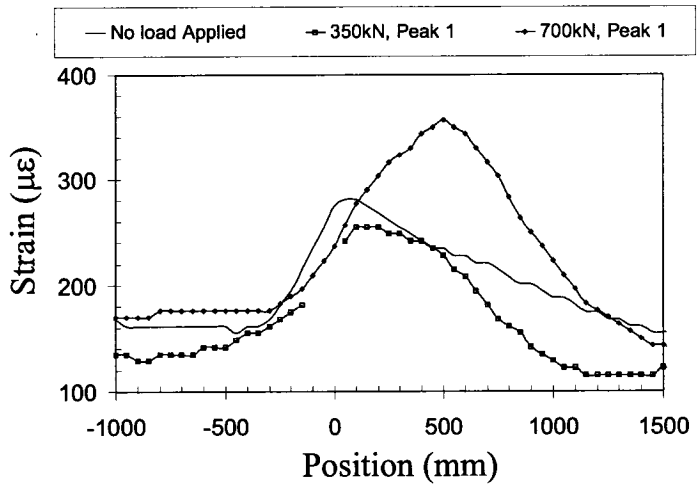

Figure VI.5: Strain profiles along fiber section c extracted from Brillouin sensor measurements. 700kN (diamond), 350kN (square) and unloaded (plain curve) cases are reported.

VI.C. Monitoring of transmission pipe buckling

VI.C.1. Experiment Description

The tested pipe is a section of a real natural gas transmission steel pipeline of the type shown in Figure VI.6.(a). The pipe was sealed on both ends. To simulate a real condition of operation of a natural gas pipe, the inner pressure was kept at 18.4 MPa during the whole buckling experiment. Longitudinal directions at 6 and 12 o'clock positives along the pipe were subjected to tension and compression, respectively, by

applying simultaneous vertical and lateral forces. The sensor characteristics and set-up are presented in section IV.B. Typical data acquisition time is 10 minutes.

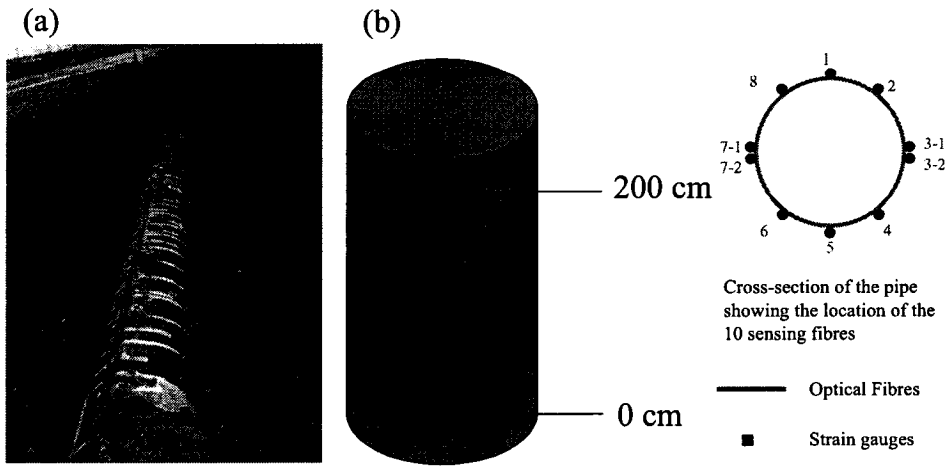

Figure VI.6: (a) Example of a transmission pipe in its trench (picture taken at TransCanada PipeLine plant of Spruce Groove, Alberta). (b) Axial layout of the sensing fibre; the 10 sections are glued and connected to each other by 1 metre long of loose fibre.

A 29 m acrylate buffered SMF-28 optical fibre was used to measure the strain along the pipe. 10 fibre sections located from 6 to 12 o'clock around the pipe were glued on the external surface to measure strain changes on the outer surface, as illustrated in Figure VI.6.(b). Each glued section is connected by 1 meter of loose fibre. Figure VI.6.(b) also shows the instrumentation of the pipe with strain gauges. These devices are glued in parallel with fibre sections 1 and 5.

VI.C.2. Results and analysis

Strain distributions along section 5 (tension side) under two vertical and bending loads conditions are presented in Figure VI.7. It appears that for both load conditions, the largest tensile strain occurs around 140 cm from the bottom of the specimen. The evolution from lower load (Figure VI.7.(a)) to higher load levels (Figure VI.7.(b))

emphasized the strain increase at that location. Assuming that the compressive strain coefficient is the same as that of the tensile strain, we drawn the strain profile of the compression side (section 1) in Figure VI.8. As in the tension case, the largest compressive strain (largest in absolute value) is observed at 140 cm. Again the compressive strain increases significantly when the load is stronger. The behaviours illustrated by Figures VI.7 and VI.8 indicates that the largest values of compressive and tensile strains observed at ~140 cm are the signature of the buckling formation, which is confirmed by visual inspection (Figure VI.9). When vertical and bending loads were further increased, the sensing fibre glued on the compression side of the pipe (section 1) ruptured terminating further measurements with the DBS.

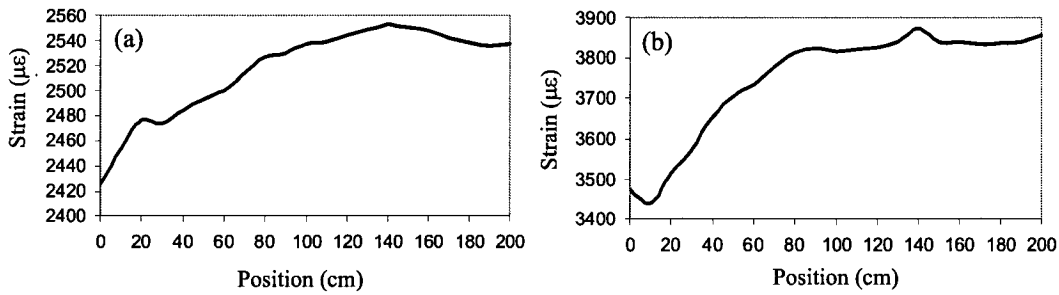

Figure VI.7: Strain distributions along section 5 of the pipe: (a) Vertical load of 8799 kN and horizontal load of 979 kN; (b) vertical Load of 8954 kN and bending load of 1334 kN (Zou 2006, Ravet 2007).

The strain-load relations at the buckling locations of Sections 5 and 1 are shown in Figure VI.10. In the tensile part, the strain increases linearly with bending load. In the compressive part, the strain increases linearly with bending load until the load reaches the value of 890 kN where the strain reaches the material yield point. The slope of the curves in the linear behaviour is the same for both tension and compression mechanisms.

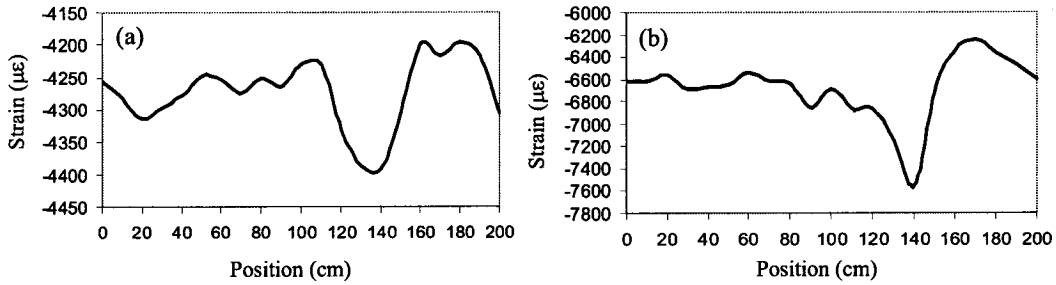

Figure VI.8: Strain distribution along section 1 of the pipe: (a) Vertical load of 8799 kN and horizontal load of 979 kN; (b) Load of 8954 kN and bending load of 1334 kN (Zou 2006, Ravet 2007).

Since the buckling locations on the pipe are not known a-priori, there were no strain gauges attached in the region of buckling. A strain gauge was attached to the pipe at the middle of its compression side. Compressive strains of – 4330 and – 6856 με measured by the DBS at the same location, when the horizontal load is 979 kN and 1334 kN, respectively, match the readings from the strain gauge.

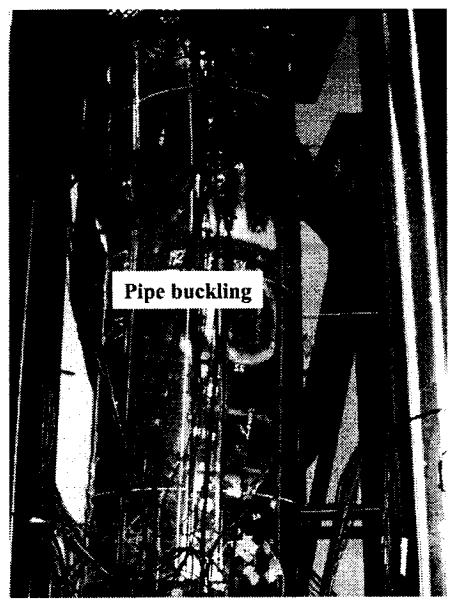

Figure VI.9: Buckled pipe with buckling located 140 cm above the base (picture taken at CFER structural laboratory in Edmonton, Alberta) (Zou 2006, Ravet 2007).

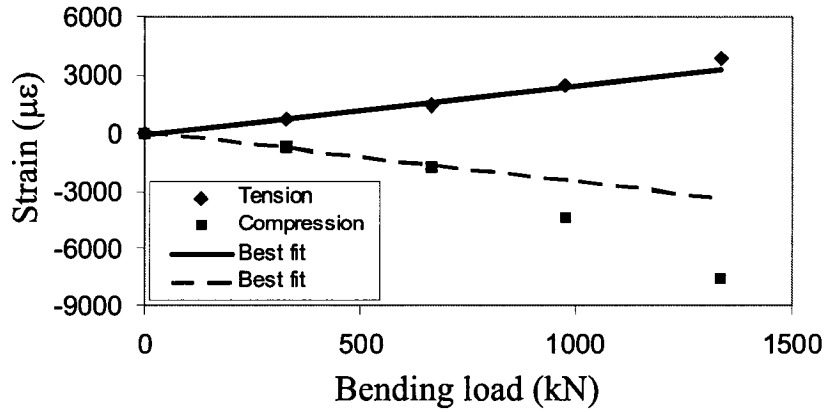

Figure VI.10: Strain- bending load relations measured at buckling locations of tension (section 5) and compression (section 1) sides (Zou 2006, Ravet 2007).

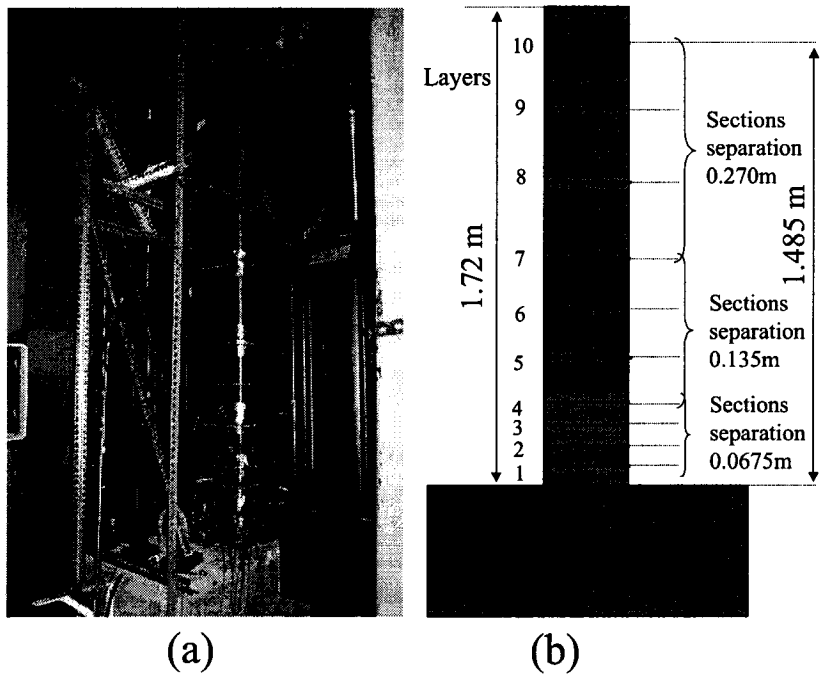

Figure VI.11: (a) Instrumented FRP/concrete column in test set-up; (b) Column dimensions and fibre optic layout kN (Ravet 2006, Ravet 2007)

VI.D. Monitoring of FRP-concrete column subjected to seismic load

VI.D.1. Experiment description

A large reinforced concrete building column, encased in FRP casing, was constructed and tested under simulated seismic loading (Figure VI.11). The column had

a 270 mm square cross-section and a 1.72 m height. The column contained eight 16 mm diameter longitudinal steel bars, which were anchored to the column footing with 90-degree hooks. The confinement was provided solely by the FRP tube, as the column contained no transverse steel reinforcement. The specimen represented a first storey column of a multi-storey building and it was tested under an axial load of 1880 kN. The specimen was subjected to lateral displacement excursions, consisting of incrementally increasing deformation reversals. The lateral displacement is measured by the drift parameter defined as the ratio of the lateral displacement to the height of the column. Three full cycles were applied at each deformation level, starting with drift value of 0.5%, then 1%, 2%, 3% etc, in the deformation control mode of the horizontal actuator. Lateral loading continued until the specimen was unable to maintain a significant fraction of its maximum lateral load resistance. In the rest of this section, the lateral displacement will be associated with push and pull configurations, push and pull referring to the relative location of the observatory. The sensor characteristics and set-up are presented in section IV.B. Typical data acquisition time is 10 minutes.

Acrylate buffered SMF-28 fibres are glued horizontally at 10 distinct cross-sections of the column (from bottom, layer 1, to the top, layer 10) shown in Figure VI.11.(b), which is separated by 1m of loose fibre. An optical pulse is launched at the end of the fibre located at the top of the column (layer 10). Measured strain data with strain gauges and distributed sensors were used to monitor the column's response to seismic loading at each drift step. Strain gauges were also placed on the surface of the FRP casing, oriented in the direction of the carbon fibres as illustrated in Figure VI.12.

These devices are symmetrically glued on both pull and push sides of the column close to each level determined by a glued fibre optic (Figure VI.12).

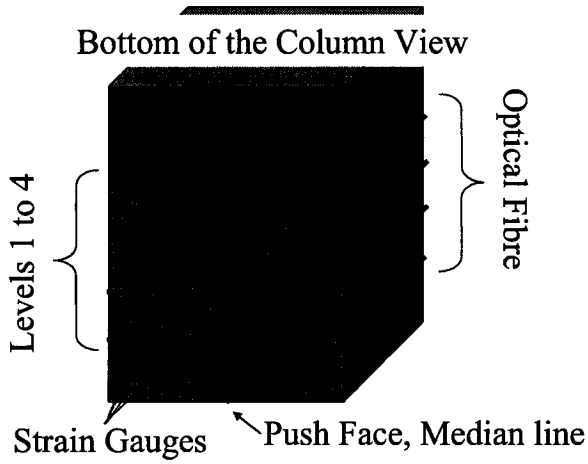

Figure VI.12: Detailed view of the bottom of the column kN (Ravet 2006, Ravet 2007)..

VI.D.2. Results analysis

Peak frequencies are extracted from the spectra in order to obtain hoop strain distributions. The peak strains for the push and pull conditions at drifts 4 and 8% are presented in Figure VI.13. Large strains are concentrated at the bottom of the column (levels 1 to 5) with a peak value at level 2. This was supported by the recorded strain gauge data, which were reported elsewhere (Ozbakkaloglu 2007). The most extensive damage occurred at approximately 100 mm to 160 mm above the column-footing interface, which coincided with the location of first fibre rupture in all columns. The shifting of the critical section from the interface was attributed to the confining effect of the footing as previously reported (Sheikh 1993; Ozbakkaloglu 2006, Ozbakkaloglu 2007). Note that strain that appears to be constant at 8% for levels 6 to 10 means that the actual strain is smaller than these reported values. In this case, Brillouin frequency span started at 12900MHz.

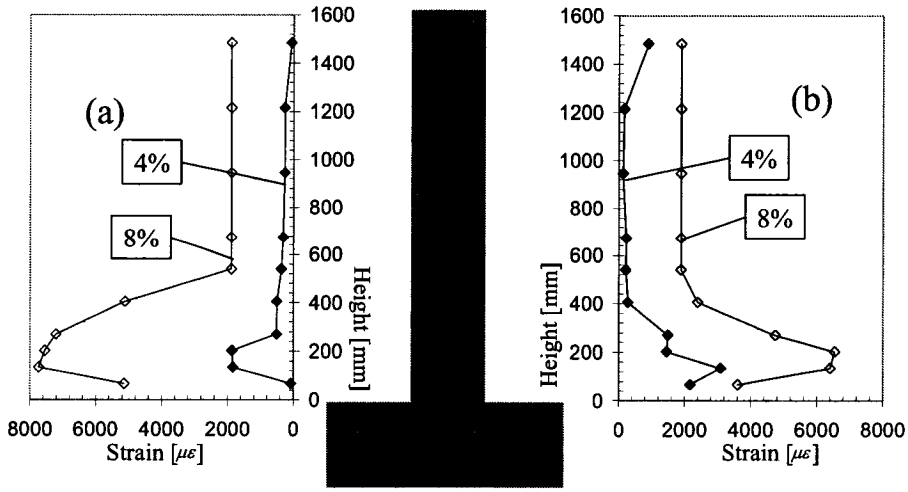

Figure VI.13: Axial profile of peak strain for (a) pull face and (b) push faces under respectively pull and push conditions. Open symbol curves correspond to a drift of 8% and full symbols are associated with a drift of 4%. Constant strain for 8% cases (Layers 6 to 10) means that actual strain is smaller than reported values. In this case, Brillouin frequency span started at 12900MHz (Ravet 2007)..

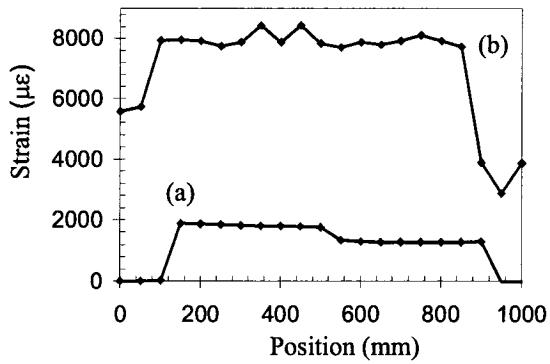

Figure VI.14: Hoop strain profiles for layer 2 under pull condition with drifts of 3% (a) and 8% (b) (Ravet 2007).

Figure VI.14 represents the hoop strain along layer 2, the layer of largest strain, for pull case with drifts of 3% (Figure VI.13.(a)) and 8% (Figure VI.13.(b)). ε'_{pk} is maximum at 3% drift on pull face. Highest strains are concentrated on pull side of the column with maximum non-uniform strains. The structure is capable to absorb stresses locally. On the contrary, it appears very different in 8% case: ε'_{pk} is high everywhere

around the column when large strains dominate. This suggests that concrete at critical section of column is significantly damaged and generating large amount of pressure on FRP casing.

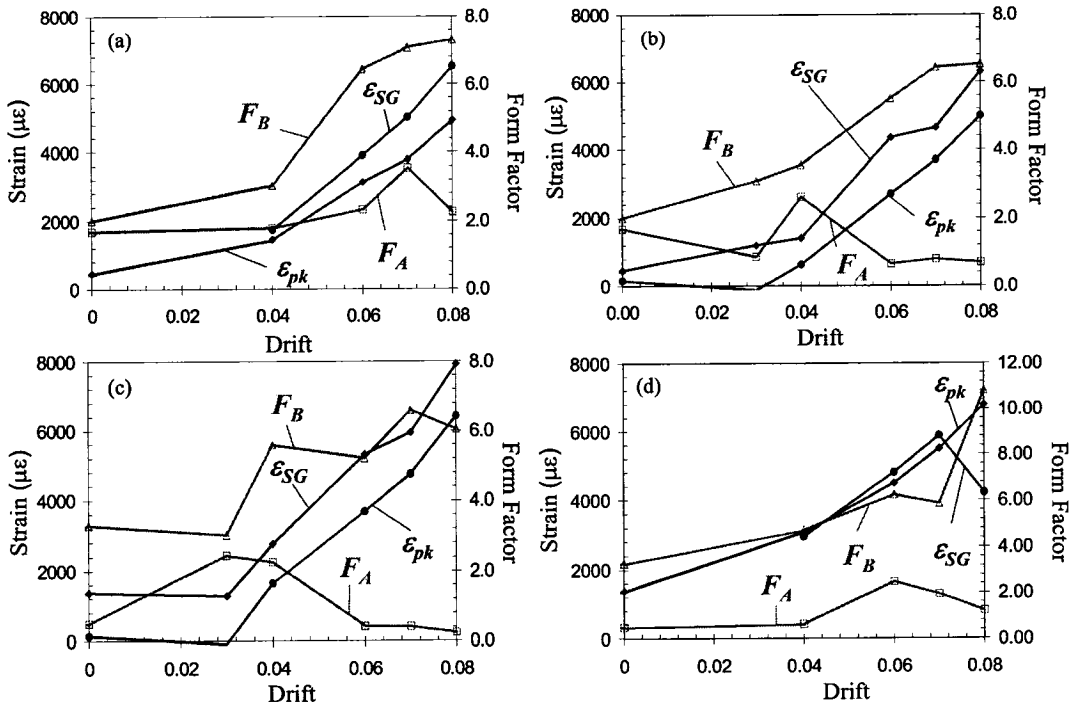

Figure VI.15: Peak frequency (left y axis) and form factors (right y axis) as a function of column drift: (a) push side, Layer 4, median point, push condition; (b) push side, Layer 4, median point, pull condition; (c) push side, Layer 2, median point, push condition; (d) push side, Layer 2, median point, pull condition (Ravet 2006, Ravet 2007).

From each Brillouin measurement, we also calculated F_A and F_B. We then drawn ε_{pk} and the two form factors as a function of the drift amplitude for both push and pull condition. We concentrated our analysis on two fibre sections located on the median of layers 2 and 4 of push side (Figure VI.12). We also analysed the median point of layer 4 of pull (i.e. symmetric of layer 4 push side).

The progressive column degradation can be viewed closely using ε'_{pk}, ε'_{SG} (readings from strain gauges shown in Figure VI.12) and the form factors. A detailed analysis of the median line of levels 4 and 2 of the push side is provided (Figure VI.15). Most of these graphs show that ε'_{pk}, ε'_{SG} and F_B experience a monotonic increase with a slope rise at larger drifts. The slope change happens when $F_A \approx 2$ and $F_B \approx 3$. At larger drifts, F_B tends to saturate or to fluctuate. F_A increases above 2 (it can reach a maximum of 4) and then drops below 1 and becomes steady. The behaviour of these four parameters can be associated with the column degradation. The region of smaller ε'_{pk} slope corresponds to the elastic condition. At that stage, the damage in the concrete is not significant and it is still capable of resisting the applied loads without a significant contribution from the FRP casing to maintain the column. Moreover the concrete and FRP are still holding together. The increase of F_A and F_B values are associated with the appearance of local stresses, contributing to the crushing and deformations of the concrete. The slope change of ε'_{pk} at $F_A \approx 2$ and $F_B \approx 3$ is associated with the appearance of local stresses indicating the start of local crushing of the concrete at the critical region of the column. Concrete crushing is visually evident as shown in Figure VI.16. The increase of ε'_{pk} slope is then a manifestation of extensive damage in the column concrete. At this point, FRP and concrete are fully de-bonded. The column requires high confinement pressures from the FRP tube to maintain its integrity, and transverse strains in the FRP tube increases rapidly with increasing drift. Finally, when F_B saturates (and/or fluctuates) and $F_A \leq 1$ at large drift, large strain is the dominant contribution. The column safety is then threatened. The FRP, being the only element

supporting the structure, starts to rupture locally. These ruptures release locally the tension inducing a local strain reduction (ε'_{SG} drops as shown in Figure VI.15.(d)), mitigating the spectrum broadening but ε'_{pk} increases, meaning that the structure continues to degrade.

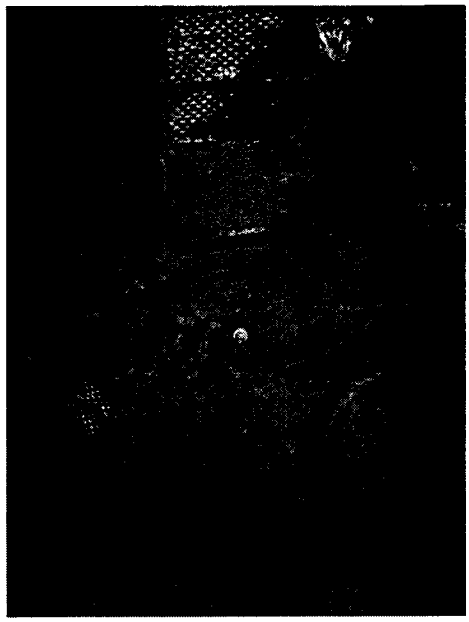

Figure VI.16: Post-mortem analysis of the column: concrete at the bottom part has been crushed; once FRP is removed, concrete dust flown on the column support (Ravet 2006).

Table VI.1 summarizes the relationship of the structure behaviour with the three parameters variation. Monitoring the changes of these values can predict the early sign of collapse. The conclusions drawn in Table I are valid for 1.7 ns pulses but should not be affected by pulse width of the same order of magnitude, which is the best spatial resolution that can be currently achieved.

The spectrum shape analysis is then a powerful approach when their static and dynamic variations are considered. First, global structure deformation is monitored through the Brillouin peak frequency. Second, form factors are the signature of local

defects induced by non-uniform strains, which cause the spectrum broadening and/or asymmetry. Third, the plot of their change as a function of stress to get the metric/load slope change indicates non-linearity of these parameters change. The relationship between load and strain is expected to be linear as long as localised defects are absent. The tracking of slope variation would give us an indication on local defects apparition, such as de-bonding and cracks (or crushed concrete).

Table VI.1: Signature of Structure failure with form factors (Ravet 2006, Ravet 2007).

Strain Observation	F_A	F_B	ε_{pk} Slope	Structure Status
Uniform	<2	<3 Small slope	Constant, small	Elastic regime, good shape
Non-uniform, low strain dominates	>2 Peak value	>3 Large slope	Increase	Deformation, local cracks, local de-bonding
Non-uniform, large strain dominates	<1 Stationary	>>3 Constant and large slope	Constant, Large	Full FRP/concrete de-bonding
Reduced non-uniformity, large strain dominates	<1 Stationary	>>3 Stationary	Constant, Large	FRP cracks

VI.E. Strategies for temperature compensation with the DBS

In the tests we carried out, the temperature of the environment was controlled and variations were smaller than 1°C. Such situation is rarely encountered on the field where temperature variations are part of the measurement conditions. In fact, field implementation requires that the temperature influence on strain measurement must be compensated. Various strategies can be used involving the simultaneous monitoring of strain and temperature with the DBS. The simplest consist in laying out an adjacent

stress free fibre (Bao 1994) or in gluing the jacket of a loose tube optical fibre cable. In that last case, all mechanical changes of the structure will only affect the cable while the fibre remains unstressed. This approach has led to the development of specialty cables which are specifically designed to measure temperature or strain (Inaudi 1997). It is also possible to measure simultaneously strain and temperature with a single fibre. Sensing can then be achieved by monitoring Brillouin frequency shift and Brillouin peak power (Smith 1999). Simultaneous temperature and strain can also be achieved by using fibres with multiple Brillouin peaks such as LEAF type (Lee 2001) and Photonics crystal fibres (PCF, Zou 2005a). Finally, the distinct Brillouin behaviour of the slow and fast axis of polarisation maintaining fibres (PMF) is another approach to measure strain and temperature at once (Bao 2004).

VI.F. Summary

Our work is an important step towards SHM, in particular of the early detection of problems structure. The sensor was applied to the monitoring of concrete/FRP beams and to pipe buckling detection which are distinct study cases by the nature of the structure material. From our results, it is clear that our approach can be used to provide design guideline of civil engineering structures using new materials. Our signal processing approaches, based on a spectrum pre-analysis with the help of the REC, also provide a significant improvement on the capability of the distributed sensor system, which was only used for average strain estimation. Now, we can access both global structure status and local defect detection at once. The DBS is then a valuable tool for civil engineers involved in health monitoring of old infrastructures or in the development of new materials.

Chapter VII: Conclusion

VII.A. Thesis outcomes

Although the study of Brillouin scattering was initiated in the early twenties, research in the field really gained momentum in the sixties with the introduction of lasers and improved spectrum analysis techniques. Since then, related research are very productive and the applications of Brillouin scattering are numerous. Among them, we are more particularly interested in the temperature and strain dependence of Brillouin interaction in single-mode optical fibres. Once these properties are combined with a pulsed probe lightwave, a distributed sensor can be developed. The sensor configuration, or DBS, we studied in the present work was first proposed in 1993 (Bao 1993a) and was improved until now to obtain smaller spatial resolution without affecting frequency resolution (Zou 2005, Kalosha 2006).

The DBS set-up, based on Brillouin loss, involves a *cw* pump and a counterpropagating Stokes pulse. The output pump power variation is monitored at the pulse input end of the fibre. In this thesis, we demonstrated that the performances of the sensor are strongly dependant on the pump power, the pulse characteristics and the fibre length. As the sensor relies on the pump loss to record changes in the fibre, its depletion is an inherent mechanism of the sensing operation. Nevertheless, we have seen that pump depletion must be carefully controlled to maintain optimum sensing performances (Ravet 2006a).

Within that context, we have investigated the definition of SBS threshold for a BFG configuration. We proposed an interpretation of one of the experimental definitions of the threshold (1% criterion), which is seen to be the input power for which the pump becomes depleted and the gain saturated. Pump depletion and gain saturation being affected by the fibre length and the Stokes power, we generalised the threshold definition to the BFA layout, which is the configuration of the DBS, and derived an original expression for the threshold. That formula is applicable to the BFA as it is a function of the fibre characteristics as well as the input Stokes power. It can be used to estimate the maximum Stokes power that can be fed into the fibre to avoid large pump depletion and hence degraded sensor performance. From our work, we also show that threshold determines the limit of applicability of the weakly depleted approximation model that gives analytical expressions for both pump and Stokes spectrum distributions.

We have shown that even under weak pump depletion, the spectrum shape is influenced by the sensor settings such as pump and Stokes power as well as fibre length. The Spectrum being also position dependent, we proposed a novel signal processing method based on the physics of SBS in weakly depleted regime. That signal processing method involves the modelling of the sensor operation by an analytical model as well as the use of original data analysis tools, that is to say the LS diagram, the REC and the form factors (Ravet 2005, Ravet 2005a, Ravet 2006, Ravet 2006c). The method has been successfully tested on experimental data. The advantages of this signal processing method are multiple. First, we gain a capability of decorrelating the effects of the sensor settings from the measured data. Second, the data analysis tools facilitate the extraction

of the sensed information from the measured spectra. Third, as the approach is iterative, the data analysis tools are used to give an educated guess of what the sensed information is speeding up the reconstruction process.

Eventually, the behaviour of real civil engineering structures subjected to heavy load was investigated with the help of the DBS. The sensor, with the help of the appropriate signal processing approach, was capable of locating defects at the same time as it was providing information about the global status of the structures. The events detected are pipe buckling, concrete crushing, concrete/FRP debonding and FRP rupturing (Ravet 2005b, Ravet 2006, Ravet 2006b, Ravet 2007).

Most of the results obtained within the context of the present thesis have been presented in international conferences and in articles published in letters and journals. A complete list of these publications can be found in Chapter XI.

VII.B. Tracks for the future

As seen in Chapter III, BFA configurations started to be studied at the end of eighties and continued in the nineties (Olsson 1986, Tkach 1989, Ferreira 1994). Those studies revealed that the BFA experiences poor noise behaviour. The generation of spontaneous noise from Brillouin scattering and its amplification significantly degrade the SNR of signals exiting the fibre. That should not be an issue in short sensing fibres but the effect must become critical in longer sensing configurations such as the ones encountered in the monitoring of river levees or pipelines. The impact of amplified Brillouin spontaneous emission (ABSE) should be investigated and, if needed, the effect could be added to the phenomenological model. That would also require study of the

effect of ABSE on the receivers, and, lead to the introduction of a new component in the signal processing method.

Simultaneous strain and temperature measurement is possible with the DBS using the various solutions discussed in Chapter VI. When it comes to long length and field implementations, techniques based on PMF or PCF risk to be rejected, at the current stage, due to their huge cost. An economic solution involving the use of a single sensing fibre is possible by considering telecommunication fibres such as LEAF type or equivalent (Lee 2004). Experimental evidence of the use of such fibres on long sensing length and on the field still needs to be demonstrated. If such development is possible, the signal processing method proposed in the current thesis should be adapted to account for the new capability.

Field demonstrations of the DBS ability must be pursued with a focus on long distance applications such as pipelines and river levees. Work should be carried out to show that the high spatial and frequency resolutions are still effective on real structures. Within that framework, the extension of the DBS measurement range with optical amplification is certainly of interest.

A practical issue that has not been discussed in the present thesis need to be addressed as civil engineers become more and more interested in the DBS. That issue is the relationship between Brillouin frequency and compressive strain, although a previous experimental study had shown that tensile and compressive strain coefficients are the same (De Merchant 1999). In our work, we have assumed that the coefficient was the same as the one measured for tensile strain. The qualitative match between our measurements and the electrical strain gauge readings suggests that our assumption was

reasonable *a posteriori*, and, confirmed the experimental results of De Merchant et al (De Merchant 1999). Nevertheless, we believe that the accurate relationship needs to be known. End users of the DBS are expecting precise measurements. Some research works could be carried out to develop an experimental set-up to induce compressive strain and to calibrate any fibre type before it is used in compression experiments. These researches could be extended to the study of the core/cladding/coating interfaces behaviour when the fibre is compressed. Change in these interfaces could influence the acoustic wave propagation and then the scattering properties of the medium. Gaining understanding of these effects would help to improve the design of sensing fibres.

Finally, the results presented in this thesis can be applied to other applications. As mentioned in the introduction, it has been demonstrated that a Stokes pulse can be slowed in a Brillouin medium (Okawachi 2005, Song 2005). This approach is seducing as it can be implemented in all optical buffers or routers. Unfortunately, it suffers a severe drawback, which is the linewidth of the Brillouin resonance. The linewidth is in the range of tens of MHz while the signal bandwidth in optical communications is in the range of GHz. We have seen in this work that external stresses, when they are non-uniform, broaden the Brillouin spectrum. It is possible to take advantage of this effect by creating, on purpose, non-uniform strain and temperature distributions. Also, designing specialty fibres with core size and doping concentration variables with position would help to broaden the spectrum of the interaction. The spectrum widening improvement would then be achieved by combining all these techniques. That application would certainly contribute to further theoretical and experimental developments in the field.

Chapter VIII: References

Abramowitz, M., and Stegun, I.A., 1964. Handbook of mathematical functions. Dover Publications

Afshar S.V., Ferrier, G.A., Bao, X., and Chen, L. 2003. Effect of the finite extinction ratio of an electro-optic modulator on the performance of distributed probe-pump Brillouin sensor systems. Optics Letters **28**: 1418-1420.

Agrawal, G.P., 1995. Nonlinear fibre optics, Second Edition. Academic Press.

Agrawal, G.P., 1997. Fiber-optic communication systems, second Edition. Wiley-Interscience.

Alahbabi, M.N., Cho, Y.T., and Newson, T.P., 2006. Long-range distributed temperature and strain optical fibre sensor based on the coherent detection of spontaneous Brillouin scattering with in-line Raman amplification. Measurement Science and Technology, 17: 1082-1090.

Bao, X., Webb, D. J., and Jackson, D. A., 1993. 22-km distributed temperature sensor using Brillouin gain in an optical fiber. Optics Letters, **18**: 552-554.

Bao, X., Webb, D. J., and Jackson, D. A., 1993a. 32-km distributed temperature sensor based on Brillouin loss in an optical fiber. Optics Letters, **18**: 1561-163.

Bao, X., Webb, D.J, and Jackson, D.A., 1994. Combined distributed temperature and strain sensor based on Brillouin loss in an optical fiber. Optics Letters, **19**: 141-143.

Bao, X., Dhliwayo, J., Heron, N., Webb, D.J., and Jackson, D.A. 1995. Experimental and theoretical studies on a distributed temperature sensor based on Brillouin scattering. Journal of Lightwave Technology, **13**: 1340-1348.

Bao, X., Brown, A., DeMerchant, M., and Smith, J. 1999. Characterization of the Brillouin-loss spectrum of single-mode fibers by use of very short (<10 ns) pulses. Optics Letters, **24**: 510-512.

Bao, X., DeMerchant, M.D., Brown, A., and Bremner, T.W. 2001. Tensile and compressive strain measurement in the lab and field with the distributed Brillouin scattering sensor. Journal of Lightwave Technology, **19**: 1698-1704.

Bao, X., Yu, Q., and Chen, L., 2004. Simultaneous strain and temperature measurements with polarization-maintaining fibers and their error analysis by use of a distributed Brillouin loss system. Optical Letters, **29**:1342-1344.

Bao, X., Yu, Q., Kalosha, V.P., and Chen, 2006. The influence of prolonged phonon relaxation on the Brillouin loss spectrum for the nanosecond pulses. Optics Letters, **31**: 888-890.

Bayvel, P., Giles, I.P., and Radmore, P.M., 1989. Transients and steady-state characteristics of a Brillouin amplifier based on an all-fibre single-mode ring resonator. Optical and Quantum Electronics, **21**: S113-S128.

Bayvel, P., and Radmore, P.M., 1990. Solutions of the SBS equations in single-mode optical fibres and implications for fibre transmission systems. Electronics Letters **26**: 434-436.

Brillouin, L., 1922. Diffusion de la lumière et des rayons X par un corps transparent homogène. Annales de Physique, **17**: 88-122.

Bernini, R., Minardo, A., and Zeni, L. 2002. Reconstruction technique for stimulated Brillouin scattering distributed fiber-optic sensors. Optical Engineering, **41**: 2186-2194.

Bertholds, A., and, Dandliker, R., 1988. Determination of the individual strain-optic coefficients in single-mode optical fibers. Journal of Lightwave Technology, **6**: 17-20.

Billington, R., 1999. Measurement methods for stimulated Raman and Brillouin Scattering in optical fibres. National Physical Laboratory Report COEM 31.

Bisby, L.A., 2004. ISIS educational module 5: an Introduction to structural health monitoring. ISIS Canada.

Born, M., Wolf, E. 1999. Principles of optics. London: Cambridge University.

Boyd, R.W., Rzazewski, K., and Narum, P. 1990. Noise initiation of stimulated Brillouin scattering. Physical Review A, **42**: 5514-5521

Boyd, R.W., 2003. Nonlinear optics, Second Edition. Academic Press.

Brown, A., DeMerchant, M.D., Bao, X., and Bremner, T.W. 1999. Spatial resolution enhancement of a □entimetr-distributed sensor using a novel signal processing method in Single-mode optical fibers. Journal of Lightwave Technology, **17**: 1179-1183.

Brown, A. 2000. PhD Thesis, University of New Brunswick

Bucaro, J.A., and Dardy, H.D., 1974. High temperature Brillouin scattering in fused quartz. Journal of Applied Physics **45**: 5324-5329.

Butter, C., and, Hocker, G., 1978. Fiber optics strain gauge. Applied Optics **17**: 2867-2869.

Chen, L., and Bao, X., 1998. Analytical and numerical solutions for steady state stimulated Brillouin scattering in a single-mode fiber. Optics Communications **152**: 65-70.

Chiao, R.Y., Townes, C.H., and Stoicheff, B.P., 1964. Stimulated Brillouin Scattering and Coherent Generation of Intense Hypersonic Waves. Physical Review Letters **12**: 592-595.

Chu, B., 1974. Laser light scattering. Academic Press.

Culverhouse, D., Frahi, F., Pannell, C.N., and, Jackson, D.A, 1989. Potential of stimulated Brillouin scattering as sensing mechanism for distributed temperature sensor. Electronics Letters **25**: 913-915.

Culshaw, B., 2004. Optical fiber sensor technologies: opportunities and-perhaps-pitfalls. Journal of Lightwave Technology **22**: 39-50.

Dakin, J.P., Pratt, D.J., Bibby, G.W., and Ross, J.N., 1985. Distributed optical Raman temperature sensor using a semiconductor light source and detector. Electronics Letters, **21**: 569-570.

Dämmig, M., Zinner, G., Mitschke, F., and, Welling, H., 1993. Stimulated Brillouin scattering in fibers with and without external feedback. Physical Review A, 48: 3301-3309.

Danielson, B.L., 1985. Optical time-domain reflectometer specifications and performance testing. Applied Optics **24**: 2313-2322.

Debut, A., Randoux, S., and Zemmouri, J., 2000. Linewidth narrowing in Brillouin lasers: Theoretical Analysis. Physical Review A, **62**: 02803.

Debut, A., Randoux, S., and Zemmouri, J., 2001. Experimental and theoretical study of linewidth narrowing in Brillouin fiber ring lasers. Journal of the Optical Society of America A, **18**: 556-567.

DeMerchant, M.D., Brown, A., Bao, X., and Bremner, T.W., 1999. Structural monitoring by use of a Brillouin distributed sensor. Applied Optics **38**: 2755-2759.

DeMerchant, M.D. 2000. PhD Thesis, University of New Brunswick

DeMerchant, M.D., Brown, A., Bao, X., and Bremner, T.W., 2000. Signal processing for a high-spatial-resolution distributed sensor. Optical Engineering **39**: 1632-1635.

Derickson, D., 1998. Fiber Optic Tests and Measurements. Prentice Hall.

Einsfeld, R.A., Murray, D.W., and Yoosef-Ghodsi, N., 2003. Buckling analysis of high-temperature pressurized pipelines with soil structure interaction. Journal of the Brazilian Society of Mechanical Scientists and Engineers, **25**: 164-169.

Esman, R.D., and Williams, K.J., 1996. Brillouin Scattering: beyond threshold. Optical Fiber Communications, Volume 2 of 1996 OSA Technical Digest Series: 227-228.

Fabelinskii, I.L., 1968. Molecular light scattering. Plenum Press, New York.

Farries, M. C., Fermann, M. E., Laming, R. I., Poole, S. B. and Payne, D. N., 1986. Distributed temperature sensor using Nd^{3+} doped fiber. Electronics Letters, **22**: 418-419.

Fellay, A., Thévenaz, L., Facchini, M., Niklès, M., and Robert, P. 1997. Distributed sensing using stimulated Brillouin scattering: towards ultimate resolution. Optical Fiber Sensors, Optical Society of America Technical Digest Series, **16**: 324-325

Ferreira, M.F., Rocha, J.F., and Pinto, J.L., 1994. Analysis of the gain and noise characteristics of fibre Brillouin amplifiers. Optical and Quantum Electronics, **26**: 35-44.

Feynman, R.P., Leighton, R.B., and Sands, M., 1964. The Feynman lectures on physics, Volumes I and II. Addison-Wesley Publishing Company.

Fotiadi, A.,A., and Kiyan, R.V., 1998. Cooperative stimulated Brillouin scattering and Rayleigh backscattering process in optical fibers. Optics Letters **23**: 1805-1807.

Fotiadi, A.A., Kiyan, R.V., Deparis O., Mégret, P., and Blondel, M., 2002. Statistical properties of stimulated Brillouin scattering in single-mode optical fibers above threshold. Optics Letters **27**: 83-85.

Gaeta, A.L., and Boyd, R.W. 1991. Stochastic dynamics of stimulated Brillouin scattering in an optical fiber. Physical Review A, **44**: 3205-3209.

Garus, D., Schliep, F., Krebber, K., and Golgolla, T., 1996. Distributed sensing technique based on Brillouin optical-fiber frequency-domain analysis. Optics Letters, **21**: 1402-1404.

Geinitz, E., Jetshke, S., Röpke, U., Schröter, S., Wilsch, R., and Bartelt, H. 1999. The influence of pulse amplification on distributed fibre-optic Brillouin sensing and a method to compensate for systematic errors. Measurement Science and Technology, **10**: 112-116.

Hartog, A.H., 1983. A distributed temperature sensor based on a liquid-core optical fibre. Journal of Lightwave Technology, **1**, 498.

Hartog, A.H., and Gold, M.P. 1984. On the theory of backscattering in single-mode optical fibers. Journal of Lightwave Technology, **2**: 76-84.

Heiman, D., Hamilton, D.S., and Hellwarth, R.W., 1979. Brillouin scattering measurements on optical glasses. Physical Review B **19**: 6583-6592.

Hotate, K., and Hasegawa, T., 2000, "Measurement of Brillouin gain spectrum distribution along an optical fiber with a high spatial resolution using a correlation-based technique – Proposal, experiment and simulation", IEICE Transaction in Electronics, **E83C**: 405-411.

Hotate, K., and Tanaka, M., 2002. Distributed fiber Brillouin strain sensing with 1-cm spatial resolution by correlation-based continuous-wave technique. IEEE Photonics Technology Letters, **14**: 179-181.

Horiguchi, T., Kurashima, T. and Tateda, M., 1989. Tensile strain of Brillouin frequency shift in silica optical fibers. IEEE Photonics Technology Letters, **1**: 107-108

Horiguchi, T., and T., Tateda, M. Y. 1989a. BOTDA-nondestructive measurement of single-mode optical fibers attenuation characteristics using Brillouin interaction: theory. Journal of Lightwave Technology, **7**: 1170-1176.

Horiguchi, T., Shimizu, K., Kurashima, T., Tateda, M., and Koyamada, Y. 1995. Development of a distributed sensing technique using Brillouin scattering. Journal of Lightwave Technology **13**: 1296-1302.

Inaudi, D., and Glisic, B., 2005. Development of distributed strain and temperature sensing cables. 17th International Conference on Opical Fibre Sensors, Proceedings of SPIE Vol. 5855 (SPIE, Bellingham, WA, 2005): 222-225.

Ippen, E.P., and Stolen, R.H., 1972. Stimulated Brillouin scattering in optical fibers. Applied Physics Letters **21**: 539-541.

ITU-T G.652, 2000. Series G: Transmission Systems and Media, Digital Systems and Networks. International Telecommunication Union.

Jen, C.K., 1985. Similarities and differences between fiber acoustics and fiber optics. Proceedings of the IEEE Ultasonics Symposium: 1128-1133.

Jen, C.K., Oliveira, J.E.B, Goto, N.,and, and Abe, K., 1988. Role of guided acoustic wave properties in single-mode optical fibre design. Electronics Letters, **24**: 1419-1420.

Kalosha, V. P., Ponomarev, E. Chen, L., and Bao X., 2006. How to obtain high spectral resolution of SBS-based distributed sensing by using nanosecond pulses. Optics Express **14**: 2071-2078.

Kersey, A. D., 1996 . A review of recent developments in fiber optic sensor technology. Optical Fiber Technology, **2**: 291-317.

Kociński, J., and Wojtczak, 1978. Critical scattering theory, phase transition phenomena 1. Elsevier.

Kovalev, K.I., and Harrison, R.G., 2000. Observation of inhomogeneous spectral broadening of stimulated Brillouin scattering in an optical fiber. Physical Review Letters, **85**:1879-1882

Koyamada, Y., Sato, S., Nakamura, S., Sotobayashi, H., and Chujo, W., 2005. Simulating and designing Brillouin gain spectrum in single-mode fibers. Journal of Lightwave Technology, **22**: 631-639.

Kurashima, T., Horiguchi, T., and, Tateda, M., 1990. Thermal effects on the Brillouin frequency shift in jacketed optical silica fibers. Applied Optics, **29**: 2219-2222.

Kurashima, T., Horiguchi, T., Izumita, H., Furukawa, S., and, Koyamada, Y., 1993. Brillouin optical-fiber time domain reflectometry. IEICE Transactions in communications, **E76-B**: 382-390.

Landau, L., and, Lifchitz, E. 1967. Physique statistique. Editions Mir, Moscou.

Landau, L., and, Lifchitz, E. 1967a. Théorie de l'élasticité. Editions Mir, Moscou.

Landau, L., and, Lifchitz, E. 1969. Electrodynamique des milieux continus. Editions Mir, Moscou.

Lecoeuche, V., Webb, D. J., Pannell, C. N., and Jackson, D. A. 2000. Transient response in high-resolution Brillouin-based distributed sensing using probe pulses shorter than the acoustic relaxation time. Optics Letters, **25**: 156-158.

Lee, C. C., Chiang, P. W., and Chi, S., 2001. Utilization of a dispersion-Shifted fiber for simultaneous measurement of distributed strain and temperature through Brillouin frequency shift. IEEE Photonics Technology Letters, **13**: 1094-1096.

Le Floch, S., and Cambon, P., 2003. Theoretical evaluation of the Brillouin threshold and the steady-state Brillouin equations in standard single-mode optical fibers. Journal of the Optical Society of America A, **20**: 1132-1137.

Lees, G. P., Wait, P. C., Cole, M. C., and Newson, T. P., 1998. Advances in optical fibre distributed temperature sensing using the Landau-Placzec ratio. IEEE Photonics Technology Letters, **10**: 126-128.

Levelut, C., Le Parc, R., and Pelous, J., 2006. Dynamic sound attenuation at hypersonic frequencies in silica glass. Physical Review B, **73**: 052202.

Li, H. H., 1980. Refractive index of silicon and germanium and its wavelength and temperature Derivatives. Journal of Physical Chemistry Reference Data, **9**: 561-601.

Li, G.L., and, Yu, P.K.L. 2003. Optical intensity modulators for digital and analog applications. Journal of Lightwave Technology, **21**: 2010-2030.

Maclean, A., Moran, C., Johnstone, W., Culshaw, B., Marsh, D., and Parker, P., 2003. Detection of hydrocarbon fuel spills using a distributed fibre optic sensor. Sensors&Actuators: A. Physical, **109**: 60-67.

McCurdy, A.H., 2005. Modeling of stimulated Brillouin scattering in optical fibers with arbitrary radial index profile. Journal of Lightwave Technology **23:** 3509-3516

Mallinder, F.P., and, Proctor, B.A., 1964. Elastic constants of fused silica as a function of large tensile strain. Physical Chemistry of Glasses **5**: 91-103.

Minardo, A., Bernini, R., Zeni, L., Thévenaz, L., and Briffod, F. 2005. A reconstruction technique for long-range stimulated Brillouin scattering distributed fiber-optic sensors: experimental results. Measurement Science and Technology **16**: 900-908.

Murayama, H., Kageyama, K., Naruse, H., Shimada, A., and Uzawa, K. 2003. Application of fibre-Optic distributed sensors to health monitoring for full-scale composite structures. Journal of Intelligent Material Systems and Structures **14**: 3-13.

Naruse H, and Tateda, 1999. Trade-off between the spatial and the frequency resolutions in measuring the power spectrum of the Brillouin backscattered light in an optical fiber. Applied Optics **38**: 6516-6521.

Naruse H, and Tateda, 2000. Launched pulse-shape dependence of the power spectrum of the spontaneous Brillouin backscattered light in an optical fiber. Applied Optics **39**: 6376-6384.

Naruse H, Tateda, M., Ohno, H. and Shimada, A. 2002, "Dependence of the Brillouin gain spectrum on linear strain distribution on optical time-domain reflectometer-type strain sensors", Applied Optics **41**: 7212-7217.

Naruse, H., Tateda, M., Ohno, H., and Shimada, A. 2003. Deformation of the Brillouin gain spectrum caused by parabolic strain distribution and resulting measurement error in BOTDR strain measurement system. IEICE Transactions in Electronics E86-C: 2111–2121.

Nazarathy, M., Sori, N.W., Baney, D.M., and Newton, S.A. 1989. Spectral Analysis of Optical Mixing Measurements. Journal of Lightwave Technology **7**: 1083-1095.

Niklès, M., Thévenaz L., and Robert, P.A., 1996. Simple distributed fiber sensor based on Brillouin gain spectrum analysis. Optics Letters **21**: 756-760.

Niklès, M., Thévenaz L., and Robert, P.A., 1997. Brillouin gain spectrum characterization in single-mode optical fibers. Journal of Lightwave Lightwave Technology **15**: 1842-1851.

Niklès, M., 1997a. La diffusion Brillouin dans les fibres optiques: étude et application aux capteurs distribués. Thèse de doctorat, Ecole Polytechnique Fédérale de Lausanne.

Niklès, M., Briffod, F., Burke, R., and Lyons, G., 2005. Greatly extended distance pipeline monitoring using fibre optics. 24th International Conference on Offshore Mechanics and Arctic Engineering, June 12-17, 2005, Halkidiki, Greee. Proceedings of OMAE06: 1-8.

Okawachi, Y., Bigelow, M.S., Sharping, J.E., Zhu, Z., Schweinberg, A., Gauthier, D.J., Boyd, R.W., and, Gaeta, A.L., 2005. Tunable all-optical delays via Brillouin Slow Light in an Optical Fiber. Physical Review Letters, **94**: 153902.

Olsson, N.A., and van der Ziel, J.P., 1986. Cancellation of fiber loss by semiconductor laser pumped Brillouin amplification at 1.5 μm. Applied Physic Letters, **48**: 1329-1330.

Ozbakkaloglu, T. and Saatcioglu, M. 2006. Seismic performance of high-strength concrete columns confined by fiber-reinforced polymer tubes. Journal of Composites for Construction, **10**: 538-549.

Ozbakkaloglu, T. and Saatcioglu, M., 2007. Seismic performance of square high-strength concrete columns in FRP stay-in-Place formwork. Journal of Structural Engineering, **133**: 44-56.

Press, W.H., Flannery, B.P., Teukolsky, S.A., and, Vetterling, W.T. 1999. Numerical recipes in C: the art of scientific computing. Cambridge, New York, New Rochelle, Melbourne, Sydney.

Parker, T. R., Farhadiroushan, M., Feced, R., Handerek, V. A., and Rogers, A. J., 1998. Simultaneous distributed measurement of strain and temperature from noise-initiated Brillouin scattering in optical fibers. Journal of Quantum Electronics, **34**: 645-659.

Palmer, A.C., and Williams, P.J., 2003. Frost heave and pipeline upheaval buckling. Canadian Geotechnical Journal, **40**: 1033-1038.

Ravet, F., Bao, X., Yu, Q., and, Chen L, 2005. Criterion for Sub-Pulse-Length Resolution and Minimum Frequency Shift in Distributed Brillouin Sensors. IEEE Photonics Technology. Letters, **17**: 1504-1506.

Ravet, F., Bao, X., Yu, Q., and, Chen L, 2005a. A simple approach to determine minimum measurable stress length and stress measurement accuracy in distributed Brillouin sensing", Applied Optics, **44**: 5204-5310.

Ravet, F., Zou, L., Bao, X., Chen, L., Huang, R.F., and Khoo, H.A., 2005b. Pipeline buckling detection by the distributed Brillouin sensor. Sensing Issues in Civil Structural Health Monitoring, Farhad Ansari Editor, Springer Verlag: 515-523.

Ravet, F., Bao, X., Ozbakaloglu, T., and Saatcioglu, M., 2006. Signature of structure failure using asymmetric and broadening factors of Brillouin Spectrum. IEEE Photonics Technology Letters, **18**: 394-396.

Ravet, F., Chen, L., Bao, X., Zou L., and Kalosha, V.P., 2006a. Theoretical study of the effect of slow light on BOTDA spatial resolution. Optics Express, **14**: 10351-10358.

Ravet, F., Zou, L., Bao, X., Chen, L., Huang, R.F., and Khoo, H.A., 2006b. Detection of buckling in steel pipeline and beam by the distributed Brillouin sensor. Optical Fiber Technology, **12**: 305-311.

Ravet F., Bao X., Li Y., Yu Q., Yale A., Kalosha V.P., and Chen L., 2006c. Signal processing technique for distributed Brillouin sensing at centimetre spatial resolution. Accepted for publication in the Journal of Lightwave Technology (submitted October 2006, accepted July 2007, to be published in November 2007 issue).

Ravet, F., Zou, L., Bao, X., Ozbakkaloglu, T., Saatcioglu, M., and Zhou, J., 2007. Distributed Brillouin sensor for structural health monitoring. Canadian Journal of Civil Engineering **34**: 291-297.

Rich, T.C., and, Pinnow, D.A., 1972. Total optical attenuation in bulk fused silica. Applied Physics Letters **20**: 264-266.

Rich, T.C., and, Pinnow, D.A., 1974. Evaluation of fiber optical waveguides using Brillouin spectroscopy. Applied Physics Letters **13**: 264-266.

Rowell, N.L., Thomas, P.J., van Driel, H.M., and, Stegeman, G.I., 1979. Brillouin spectrum of single-mode optical fibers. Applied Physics Letters **34**: 139-141.

Ruffin, A.B, Li, M.-J., Chen, X., Kobyakov, A., and Annunziata, F., 2005. Brillouin gain analysis for fibers with different refractive indices. Optics Letters **30**: 3123-3125.

Schroeder, J., 1977. Light scattering of glass. Treatise on material science and technology, Volume 12. Glass I: interaction with electromagnetic radiation. Academic Press: 157-222.

Sheikh, S.A., and Khoury, S.S., 1993. Confined concrete columns with stubs. ACI Structural Journal **90**: 414-431.

Shibata, N., Waarts, R.G., and, Braun R.P., 1987. Brillouin-gain spectra for single-mode fibers having pure-silica, GeO2-doped, and P2 05-doped cores. Optics Letters **12**: 269-271.

Shibata, N., Azuma, Y., Horiguchi, T., and, Tateda, M., 1988. Identification of longitudinal acoustic modes guided in the core region of a single-mode optical fiber by Brillouin gain spectra measurements. Optics Letters, **13**: 595-597.

Shibata N., Okamoto K., and, Azuma, Y., 1989. Longitudinal acoustic modes and Brillouin-gain spectra for GeO2-doped-core single-mode fibers. Journal of the Optical Society of America B, **6**: 1167-1174.

Shibata, N, Nakazono, A., Taguchi, N., and, Tanaka, S., 2006. Forward Brillouin scattering in holey fibers. IEEE Photonics Technology Letters, **18**: 412-414.

Siegman, A.E., 1986. Lasers. University Science Books.

Smith, R.G., 1972. Optical power handling capacity of low loss optical fibers as determined by stimulated Raman and Brillouin scattering. Applied Optics, **11**: 2489-2494.

Smith, J., Brown, A., DeMerchant, M., and Bao, X. 1999. Pulse width dependence of the Brillouin loss spectrum. Optics Communications, **168**: 393-398.

Smith, J., DeMerchant, M., Brown, A., and Bao, X., 1999. Simultaneous distributed strain and temperature measurement. Applied Optics, **38**: 5372-5377.

Song K.-Y., González-Herráez, M., and Thévenaz, L., 2005. Observation of pulse delaying and advancement in optical fibers using stimulated Brillouin scattering. Optics Express, **13**: 82-88.

Stépien, L., Randoux, S., and Zemmouri, J., 2002. Origin of spectral hole burning in Brillouin fiber amplifiers and generators. Physical Review A, **65**: 053812

Takushima, Y., and Kikuchi, K., 1995. Spectral gain hole burning and modulation Instability in a Brillouin fibre amplifier.

Tang, C.L., 1966. Saturation and spectral characteristics of the Stokes emission in the stimulated Brillouin process. Journal of Applied Physics, **37**: 2945-2955.

Tennyson, R.C., and Morison, W.D. 2006. Long gage-length fiber optic sensors for monitoring pipeline integrity. Proceedings of SPIE Smart Structures and Materials, San Diego, CA, USA, February 26 – March 2, 2006.

Tennyson, R.C., Coroy, T., Duck, G., Manuelpillai, G., Mulhivill, P., Cooper, D.J.F., Smith, P.W.E., Mufti, A.A., and, Jalali, J.J. 2000. Fibre optic sensors in civil engineering structures. Canadian Journal of Civil Engineering, **27**: 880-889.

Thévenaz, L., 1998. COST 241 Final Report, SG2.4, Limitations caused by non-linear effects: 97-100.

Thévenaz, L., Song, K.-Y., and González Herráez, M., 2006. Time biasing due to the slow-light effect in distributed fiber-optic Brillouin sensors. Optics Letters, **31**: 715-717.

Thévenaz, L., 2006a. Review and progress in distributed fiber sensing. 18th International Conference on Optical Fibre Sensors OFS 2007, Cancun (Mexico), October 23-27, 2006, Technical Digest of the Optical Society of America, Paper ThC6

Thomas, P.J., Rowell, N.L., van Driel, H.M., and, Stegeman, G.I., 1979. Normal acoustic modes and Brillouin scattering in single-mode optical fibers. Physical Review B, **19**: 4986-4998.

Tkach, R.W., and Chraplyvy, A.R., 1989. Fibre Brillouin amplifiers. Optical and Quantum Electronics, **1**: 111-113.

Tkach, R.W., Chraplyvy, A.R., and Derosier, R.M., 1989a. Performance of a WDM network based on stimulated Brillouin scattering. IEEE Photonics Technology Letters, **21**: S105-S112.

Vacher, R., and Pelous, J., 1976. Behavior of thermal phonons in amorphous media from 4 to 300 K. Physical Review B **14**: 823-828.

Vacher, R., Pelous, J., and Courtens, E., 1997. Mean free path of high-frequency acoustic excitations in glasses with application to vitreous silica. Physical Review B **56**: 482-484.

van Deventer, O., and Boot, A.J., 1994. Polarization Properties of Stimulated Brillouin Scattering in Single-Mode Fibers. Journal of Ligthwave Technology **12**: 585-590.

Villafranca, A., Lázaro, J.A., Salinas, I., and Garcés, 2005. Stimulated Brillouin scattering gain profile characterization by interaction between two narrow-linewidth optical sources. Optics Express **13**: 7336-7341.

Wait, P.C., and Newson, T.P., 1996. Landau Placzek ratio applied to distributed fibre sensing. Optics Communications, **122**: 141-146.

Yeniay, A., Delavaux, J.-M., and, Toulouse, J., 2002. Spontaneous and stimulated Brillouin scattering gain spectra in optical fibers. Journal of Lightwave Technology **20**: 1425-1431.

Yu, J., Kwon, I.-B., and Oh, K., 2003. Analysis of Brillouin frequency shift and longitudinal acoustic wave in a silica optical fiber with a triple-layered structure. Journal of Lightwave Technology **21**: 1779-1786.

Zel'dovich, B.Y., Pilipetsky, N.F., and Shkunov, V.V., 1985. Principle of Phase Conjugation. Springer-Verlag, Berlin.

Zeng, X., Bao, X., Chhoa, C.Y., Bremner, T.W., Brown, A.W., DeMerchant, M.D., Ferrier, G., Kalamkarov A.L., and, Georgiades, A.V. 2002. Strain measurement in a concrete beam by use of the Brillouin-scattering-based distributed fibre sensor with single-mode fibers embedded in glass fibre reinforced polymer rods and bonded to steel reinforcing bars. Applied Optics **41**: 5105-5114.

Zhang, C., Bao, X., Ozkan, I. F., Mohareb, M. and Ravet, F., 2007. Novel Signal Processing for Distributed Brillouin Fiber Sensors for the Prediction of Pipe Buckling. Accepted for publication in Optical Fiber Technology (submitted November 2006, accepted June 2006).

Zou L., Bao X., and, Chen L., 2003. Brillouin scattering spectrum in photonic crystal fiber with a partially germanium-doped core. Optics Letters, **28**: 2222-2224.

Zou, L., Bao, X., Wan, Y., and, Chen, L. 2005.Coherent probe-pump-based Brillouin sensor for centimetre-crack detection. Optics Letters **15**: 370-372.

Zou, L., Bao X., and Chen L., 2005a. Distributed Brillouin temperature sensing in photonic crystal fiber. Smart Materials and Structures, **14**: S8–S11.

Zou, L., Bao, X., Ravet, F., and Chen, L., 2006. Distributed Brillouin fiber sensor for detecting pipeline buckling in an energy pipe under internal pressure. Applied Optics, **45**: 372-375.

Chapter IX: Appendixes

IX.A. Appendix 1: Computation of steady state solutions

IX.A.1. Newton-Raphson method

As derived in Chapter II, the solutions of the steady state equations for SBS (equations II.46) obtained by Chen and Bao (1998) have an implicit form. These solutions can be calculated numerically by implementing the two dimensional Newton-Raphson Method (Press 1997). It consists in finding the roots of a set of two equations such as

$$\begin{aligned} f_1(x_1, x_2) &= 0, \\ f_2(x_1, x_2) &= 0, \end{aligned} \tag{IX.1}$$

where $f_{i=1,2}$ and $x_{i=1,2}$ are the functions and the variables respectively. The roots $f_{i=1,2}$ are derived iteratively by computing the approximate zero $\boldsymbol{x}_{new}$ from an initial value $\boldsymbol{x}_{old}$

$$J(\vec{x}_{new} - \vec{x}_{old}) = -\vec{f}. \tag{IX.2}$$

Here J is the jacobian matrix. As the root finding routine is iterative, the convergence criterion commonly used is

$$\left\|\vec{f}\right\| < \eta. \tag{IX.3}$$

We take $\eta < 10^{-4}$ in all our simulations.

IX.A.2. Steady state solutions for the whole fibre

Using Chapter I definitions for $\Sigma(L,\Delta\nu)=I_p(L,\Delta\nu)+I_s(L,\Delta\nu)$, $\Delta(L,\Delta\nu)=I_p(L,\Delta\nu)-I_s(L,\Delta\nu)$, $\Sigma_0=\Sigma(0,\Delta\nu)$, $\Delta_0=\Delta(0,\Delta\nu)$ and renaming $x_1 \equiv I_p(L)$ and $x_2 \equiv I_s(0)$, we can express the two functions $f_1(x_1,x_2)$ and $f_2(x_1,x_2)$ as

$$f_1(x_1,x_2)=-x_1-I_s(L)+A(x_1,x_2)^{1/2}, \tag{IX.4.a}$$

$$f_2(x_1,x_2)=\int_{I_p(0)-x_2}^{x_1-I_s(L)} B(u,x_2)^{-1/2}\,du+\alpha L, \tag{IX.4.b}$$

where $I_p(0)$ is the input pump intensity, and, $I_s(L)$ is the input Stokes intensity. A and B functions are given by

$$A(x_1,x_2)=\{4I_p(0)x_2\exp[(g/\alpha)(x_1+x_2-I_p(0)-I_s(L))]+[x_1-I_s(L)]^2\}, \tag{IX.5.a}$$

$$B(u,x_2)=\{4I_p(0)x_2\exp[(g/\alpha)(u-I_p(0)+x_2)]+u^2\}. \tag{IX.5.b}$$

The roots of these equations are the output pump and Stokes power. To apply the Newton-Raphson method, we need an expression for the jacobian matrix. We then by differentiate $f_1(x_1,x_2)$ and $f_2(x_1,x_2)$ respectively to x_1 and x_2. This derivation is explicitly done by using Leibniz theorem for differentiation of an integral (Abramowitz, 1964). The various jacobian matrix elements are then

$$\begin{aligned} J_{11} &= \frac{\partial}{\partial x_1} f_1(x_1,x_2) \\ &= -1+\frac{1}{2}A(x_1,x_2)^{-1/2}\{4I_p(0)x_2(g/\alpha)\exp[(g/\alpha)(x_1+x_2-I_p(0)-I_s(L))]+[x_1-I_s(L)]\} \end{aligned} \tag{IX.6.a}$$

$$\begin{aligned} J_{12} &= \frac{\partial}{\partial x_2} f_1(x_1,x_2) \\ &= -1+A(x_1,x_2)^{-1/2}2I_p(0)\exp[(g/\alpha)(x_1+x_2-I_p(0)-I_s(L))]\left(1+\frac{x_2 g}{\alpha}\right) \end{aligned} \tag{IX.6.b}$$

$$J_{21} = \frac{\partial}{\partial x_1} f_2(x_1, x_2) = A(x_1, x_2)^{-1/2}, \tag{IX.6.c}$$

$$J_{22} = \frac{\partial}{\partial x_2} f_2(x_1, x_2) = \frac{1}{I_p(0) + x_2} - 2I_p(0)\left(1 + \frac{x_2 g}{\alpha}\right) \int_{I_p(0)-x_2}^{x_1 - I_s(L)} \exp\left[(g/\alpha)(u + x_2 - I_p(0))\right] B(u, x_2)^{-3/2}\, du, \tag{IX.6.d}$$

From Equation (IX.2), we express $\boldsymbol{x}_{new}$ as a function of $\boldsymbol{x}_{old}$, J and $\boldsymbol{f}$ which leads to

$$x_{1,new} = x_{1,old} + \frac{1}{J_{11}}\left(f_1 + J_{12}\frac{f_1 J_{21} - J_{11} f_2}{J_{11} J_{22} - J_{21} J_{12}}\right), \tag{IX.7.a}$$

$$x_{2,new} = x_{2,old} + \frac{f_1 J_{21} - J_{11} f_2}{J_{11} J_{22} - J_{21} J_{12}}. \tag{IX.7.b}$$

The condition $(J_{11}J_{22}\text{-}J_{21}J_{12}) \neq 0$ must be verified at any time. Equations IX.6 are applied iteratively until criterion 3 is verified. We then have found the output pump $I_p(L)$ and Stokes $I_s(0)$ intensities. Once fibre input and output intensities are known, we can numerically find the intensities distribution along the fibre.

IX.A.3. Steady state solutions for the distributed intensities

For each z, we solve Equations II.46 in their compact form e.g. by using Δ and Σ notations. With Σ_0 and Δ_0 for initial conditions, the root finding reduces to a one dimensional problem. Only Equation II.46.(a) needs to be numerically calculated. Once $\Delta(z)$ is found, we can then compute Σ by replacing Δ by the found value. Once all $\Delta(z)$ and $\Sigma(z)$ are found, we estimate pump and Stokes power at $z = L$ and we compare the obtained value to the input Stokes power $I_s(L)$. If the calculated Stokes power and $I_s(L)$ disagree, the new value of $I_p(L)$ is introduced in Equations II.46 and $I_s(0)$ is calculated by the one dimensional Newton-Raphson method. Using the new $I_s(0)$, we then start the

procedure again to compute $I_s(z)$ and $I_p(z)$ until $z = L$ is reached. This iteration is repeated as long as the relative difference between calculated input intensity and $I_s(L)$ is smaller than 10^{-4}.

IX.B. Appendix 2: Brillouin optical spectrum analyser

The Brillouin Optical Spectrum Analyser (BOSA) is an equipment available on the scientific/technical instruments market and developed by Aragon Photonics, a Spanish company. The description of the working principle is based on Villafranca (2005) and our understanding of Stimulated Brillouin Scattering.

IX.B.1. Principle

As shown in Figure 1, a *cw* narrow band pump (<100 kHz), emitted from the TLS (Tunable Laser Source), is launched into a fibre whose Brillouin gain properties are well known. That last condition requires a careful calibration of the fibre SBS characteristics. The signal to analyse is launched from the opposite end of the fibre. The fibre, pumped by the TLS, acts as a narrowband filter whose bandwidth is equal to the SBS linewidth. The filtered signal is detected by the photodetector and recorded in the computer. By tuning the pump wavelength over the whole spectrum of the signal, its spectral properties can be detected.

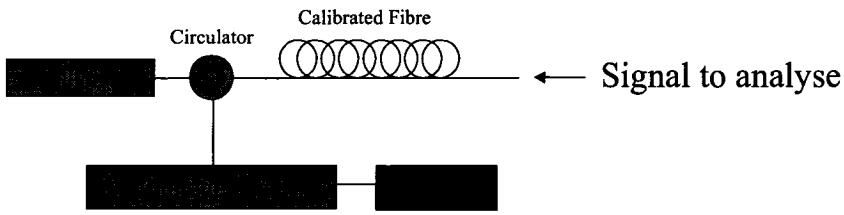

Figure IX.1: Schematic of the BOSA (TLS: Tunable Laser Source).

The performances of the BOSA are determined by the characteristics of the fibre and the pump TLS. Parameters depending on the TLS are the wavelength range, typically 100 nm, and the frequency accuracy, typically 0.01 GHz. The resolution

bandwidth depends on the fibre SBS linewidth which is approximately 10 MHz. The sensitivity is mostly determined by the photodetector performance. As the pump is a *cw* signal, lower speed photodetector are used and hence higher sensitivity are achieved. Power as small –70 dBm can be measured. Power accuracy depends on the photodetector accuracy and on the Brillouin gain, which is affected by depolarisation power stability of the pump. An accuracy of 1.5 dB can be obtained. Specifications can be obtained at http://www.aragonphotonics.com/bosa.php

IX.C. Postface: A path to the field (a tribute to multidisciplinarity and networking)

IX.C.1. Introduction

Usually in a conversation, when the word physicist pops up, people comments range from "handler of complicated stuff" to dreamer, and that can sometimes be accompanied by facial expressions, either respectful or ironical. Although, nothing is said, the body language says it all... To many, physicist work seems incomprehensible, unpractical, and it takes eternity to see the outcome of their research. When did Newton findings really make an impact to our lives? As physicists play with photons, phonons, electrons and many other "elementary particles", they have a hard time to seduce people's mind. People think: "How can they deal with those invisible objects, use them daily and improve the quality of our life?" It is possible with the virtue of networking, but not restricted to. Let us imagine that a group of scientists has found an interesting association of photons, phonons and electrons, which has been proven to be scientifically viable, that has gained recognition by peers. Furthermore it has shown potential application thanks to "in house" preliminary experiments. After such hard and relentless work of these researchers, would the outcome of their efforts reach the real world? That remains to be seen, for the journey is neither obvious nor guaranteed. This is where networking plays a key role, in bringing together physicists, people working on "abstract little things", and civil engineers[19], people working on *real* big things. Here and then comes a possibility of a success story because all ingredients are in place... This is what this essay is all about!

[19] We mention here specifically civil engineers because they are our privileged partners in this research; our appropriate association of photons, phonons and electrons being of interest for them.

IX.C.2. From physics to technology

The appropriate combination of photons, phonons and electrons that we would like to talk about is called the distributed Brillouin sensor (DBS). It is based on a physical phenomenon, the Brillouin effect, which was discussed in the early twenties by Brillouin and Mandel'shtam, scientists of the quantum revolution. In this mechanism, a laser beam, a collection of identical photons, interacts with the acoustic phonons of the material in which the lightwave propagates. These phonons are vibration modes of the medium. The light is backscattered and shifted in frequency. The frequency shift is known as the Brillouin frequency and is a characteristic of the material. The Brillouin frequency has an interesting property: if the temperature changes or if the medium is mechanically stressed, the Brillouin frequency varies proportionally. It is then clear that this concept can be transformed into temperature and strain sensors. One "only" needs to detect variations of the Brillouin frequency. If the medium is not arbitrarily chosen but it is intended to use optical fibres, the universal panacea of the telecom boom, the sensing length can reach tens of kilometres. Pulsing the lightwave allows the sensor to fulfil its intrinsic distributed nature. That is a unique feature because temperature and strain can be measured everywhere along the fibre. Photon generation and detection are achieved thanks to electron based devices: from lasers, where electronic transitions emit photons, to receiver, where photons are absorbed creating an electric current. The loop is buckled; we hope that the reader has now a clear idea of the combination of phonons, photons and electrons.

Having a brilliant idea, even when light is involved, is certainly not enough to achieve research excellence. Turning a concept into a concrete realisation takes more than a sheer hard work. First of all, scientists have to fight against the temptation of

"know it all" attitude. Permanent learning is a key point of scientific value and success. Researchers have to constantly be alert of what is happening around the globe in their related field. Beyond scientific curiosity, open mind and willingness to embrace any potential applications can be the greatest asset for researchers. And these can lead to tremendous breakthrough. Second, researchers have also to fight against the "good enough attitude". It is important to simplify all complex notions in order to bring light to some area of shadows. Revision, constant check of experiments and attentiveness, are elements that strengthen the outcomes of a research.

Then comes the time of being evaluated and recognised, if the work deserves the effort. In the specific case of the DBS project, articles have been published in high-ranking journals in the field of optics[20]. The results have been presented in peer reviewed international conferences. It is not false to claim that the DBS success has travelled around the globe, not in eighty days, but certainly more than once. The capabilities that have been displayed are so important that they have attracted the interest of potential users such as civil engineers, both from academia and industry. Besides, the good reputation has spread to the point that international students and invited researchers want to join the research team. One more proof of recognition is that industrial partners are knocking on the lab door to make the product out of this appropriate combination of photons, phonons and electrons[21].

The DBS has many potential applications. It can have an impact in civil engineering research laboratories where it can be used as a tool to monitor the behaviour of new structures and new materials. The DBS can then be a tool to improve the

[20] Among the most important, there is Optics Express, Journal of Lightwave Technology, Photonics Technology Letters, Applied Optics, Optics Letters, Optical Fiber Technology...

[21] OZ Optics, an Ottawa based company, is currently developing a sensor based on the Fiber Optic Group design. We also want to mention the know-how agreement with Neubrex in Japan and the University of Ottawa.

research in innovative construction techniques. The sensor can be implemented on critical structures such as bridges or pipelines to control their integrity in realtime. Optical fibres are everywhere, some are laid in the deep sea or crossing remote areas. Many are sleeping, waiting for bit streams. In cities, in the countryside or in logging forests, its temperature sensitivity makes it a fire detection device of choice. We can also think of geophysical prospecting or seismic sensing, to name but a few!

IX.C.3. We never know enough...

Playing with photons, phonons and electrons, then turning this play into a general public game requires highly qualified personnel. Of course, the expertise of the researchers should cover optics and electronics but not limited. A more general background is required to understand potential applications or the needs of future users. Hence, the knowledge must be broad enough to include elements of mechanics and material science, for example. In such collaborative project, the researcher must be much more than an expert. He must be open minded, stepping out of the scientist ivory tower, ready to learn subjects out of his fields. He must learn to listen, to explain and to communicate with end-users. At the same time as he needs to understand practical terms and problems, he has to be able to associate them with complicated concepts in Physics.

IX.C.4. Open your mind... You will open minds!

Being capable of thinking differently is certainly not a skill that one can acquire by hiding in a dusty library or a dark optical laboratory - in an ivory tower. That can happen only through networking and collaboration. Networking is a mind opener for scientist, the engineers of the invisible things. Here they have the opportunity to display their perspective to the real world. In the real world, world of the visible, engineers are

not necessarily inclined to "high tech", pragmatic happening of the science of invisible. Why would they use new technologies if the old techniques work well, though they contain some limitations, but at least these limitations are mastered? Through networking, they can get a closer look at some appropriate combination of photons, phonons and electrons, get a better acquaintance of it, and then build a strong confidence in its capabilities.

Even if a scientist is willing to embrace the real world with one's achievements, it can be tough without the help of networking. How would it be possible to carry out practical goals such as demonstrating that this technology is useful and valuable without being tested in civil engineering laboratories? It would be impossible to improve the sensors without the field experiment outcomes and without the ideas of the civil engineers partners. What a difficulty it would be to turn the DBS into a tool usable by non-specialists. A multidisciplinary approach is needed and cannot be imagined without networking. Without networking, a scientist would not be able to proceed to a practical implementation. Failing to demonstrate on large-scale structures that the DBS is a tool of choice for civil engineers would leave little chance to make an impact to the society.

Let us illustrate the importance of networking and the value of the Network of Centres of Excellences (NCE) programme by describing our own experience. We see the NCE as a collaborative work facilitator. On the one hand, the DBS is an extraordinary technology. It is based on beautiful science and has strong potential for applications in civil and structural engineering. On the other hand, traditional industries are investigating new building materials and methods; they feel the need for monitoring techniques that can inform them on the behaviour of new structures. Without a specific place to meet, a place where interactions between the engineering of visible and

invisible things are encouraged, the happening of a successful collaboration would be a time and energy consuming process: who to contact? What are the real applications? All these are questions we could not answer if the scientists remain in their laboratory. With NCE, partners from academia and industry come together and talk. More specifically, within the framework of ISIS Network[22], scientists can expose their ideas, work and understanding on the needs of civil engineers. Scientists and civil engineers, from academia, can exchange ideas on how and where to implement the sensor. They can run trials together to demonstrate the capabilities of the DBS. For example, we were involved in experiments where concrete columns reinforced with polymer fibres were subjected to seismic loads. We joined pipe buckling and pipe corrosion tests in Labs; in field we conducted strain tests on the first Fibre Reinforcement Polymer (FRP) based bridge in US (New Hampshire), and FRP repairs for nuclear reactor protection in Hydro Quebec. In all these trials, we were able to show that the DBS give much more information than regular techniques. The analysis of these data allowed the detection of the weakness in the structures. It was possible to monitor its expansion until it becomes fatal. Being part of the network, the industry can gain confidence on the ability of the DBS technology. Industry can bring its expertise to tailor the sensor to their needs. Once the bridge between civil engineers and scientists is solidly established, field trials can be started, with the involvement of industry. The evaluation of the sensor is not limited to part of structures anymore but it moves to the testing of bridges or pipelines. Now, the door to real world is open and the making of a product is no longer a dream. All these reasons explain how networking traces a path to the field.

[22] Intelligent Sensing for Innovative Structures, member of the NCE programme.

IX.C.5. Are we really two distinct pieces of the same puzzle?

Networking is the art of bringing people together in order to facilitate the initiation of partnerships. A partnership is not the duplication of the research but it is a vessel through which people with complementary needs exchange ideas and build a project. It must be a win/win process where partners offer the best of their competences to each other: "I have a sensor to evaluate", says the physicist; "I have a structure to test", says the civil engineer; "Let us put everything together" say both! Naturally, it is not that simple! How long will the journey on the path described by this dialog take us to finally land on the field? First, it takes time to have both parties to get a common understanding of the problem, from concepts to practical aspects associated with the trials. Dealing with light in a project does not mean that we all are on the same wavelength! Second, partners need to respect schedules; not much delay is allowed because people who are involved in this might have other projects and commitments. Third, we always want that all information, results, outcomes and success be fairly shared. All merits must be recognised at their true value.

The best way of working with partners is to make sure that goals are complementary. Partners must be committed to their engagements. A polite interest is not enough it can only be a wasting time factor. Scientists need to publish the results of their work while industry, sometimes, wants to keep the outcomes confidential. That must be clear at the beginning. Never guess what your partner goals are! That could lead to conflict and disappointment.

IX.C.6. Science, technology and beyond...

Working with partners in a research programme has a huge effect on individual's education. People learn the values of working together. Though challenging, people

from very distinct backgrounds put aside their particularism to learn something different from others. I am not thinking only about the differences between physicist and civil engineers. I also have in mind the fact that we live in a globalised world, of which Canada is a microcosm. Meeting scientists and engineers from all over the world is inevitable. Dealing with other cultures and sometimes language barriers can be challenging but always interesting and enriching. Therefore, this research programme generates value at the human level. Participating researchers enhance their technical expertise, develop human qualities such as generosity, tolerance, discover the advantage of being open minded, and, learn skills as communication, organisation or management.

At a scientific level, the understanding of the physics behind the sensor has improved. Confrontation to the real world often reveals effects that could not be generated in a laboratory environment. In field tests, no failure is allowed because experiments cannot be repeated as it would possible in the lab.

Practically, the science of this research has proven to be worthy. Civil engineers are willing to implement the DBS on structures such as bridges or pipelines. Moreover collaboration with a local company has started to develop a product, opening the door to job creation.

The DBS technology has gained the recognition of industries that contribute to the well being of our society. Its implementation on bridges or critical building will improve the safety because the structural health can be monitored and disasters prevented. Industries dealing with energy supply can rely on technique that monitors the integrity of pipelines, oil extraction and energy plants. In conjunction with the intelligence of human experts, these industries have a tool to be environment friendly.

The value of the research is hidden but as a whole, it contributes to improve the quality of life of our fellow citizens.

IX.C.7. Conclusion

The path from science to the field is a tortuous rugged track. Without any doubt, networking has made this travel smoother. Networking facilitated the collaboration of scientists and engineers, and, contributed to the happening of successful applications. We could have told this happening in a story style by starting with "Once upon a time in the east, physicists..." and ending the tale by "The physicists and the engineers get together, were happy, and they discovered and implemented many useful applications".

IX.D. Related publications

IX.D.1. Journal, Transaction or Letters

"Distributed Brillouin Sensor System Based on Offset Locking of Two DFB Lasers", Yun Li, Xiaoyi Bao, Fabien Ravet, and Evgueni Ponomarev, submitted to *Applied Optics* (August 2007).

"Power Thresholds and Pump Depletion in Brillouin Fiber Amplifiers", Fabien Ravet, Jeff Snoddy, Xiaoyi Bao, Liang Chen, submitted to Optics Letters (August 2007).

"Optimizing pulse fidelity and delay by tailoring the Brillouin frequency profile of optical fibers", Fabien Ravet, Xiaoyi Bao, and Liang Chen, submitted to *Optics Communications* (April 2007).

"Novel Signal Processing for Distributed Brillouin Fiber Sensors for the Prediction of Pipe Buckling", Chunshu Zhang, Xiaoyi Bao, Istemi F. Ozkan, Magdi Mohareb, Fabien Ravet, accepted for publication in *Optical Fiber Technology* (submitted November 2006, accepted July 2007).

"Signal processing technique for distributed Brillouin sensing at centimeter spatial resolution", Fabien Ravet, Xiaoyi Bao, Yun Li, Qinrong Yu, Alexandre Yale, V.P. Kalosha, Liang Chen, accepted for publication in the *Journal of Lightwave Technology* (submitted October 2006, accepted July 2007, to be published in November 2007 issue).

"Distributed Brillouin Sensor for Structural Health Monitoring", Fabien Ravet, Lufan Zou, Xiaoyi Bao, Togay Ozbakkaloglu, Murat Saatcioglu, Joe Zhou, *Canadian Journal of Civil Engineering* , Vol. 34, No. 3, pp. 291-297 (2007).

"Stabilization of EOM bias voltage drift using lock-in amplifier and PID controller in distributed Brillouin sensor system", Jeff Snoddy, Yun Li, Fabien Ravet, Xiaoyi Bao, *Applied Optics*, Vol. 46, No. 9, pp. 1482-1485 (2007).

"Distributed Brillouin Sensor Monitoring of an FRP-Concrete Column Subjected to Heavy Load", Fabien Ravet, Lufan Zou, Xiaoyi Bao, Togay Ozbakkaloglu, Murat Saatcioglu, *FRP International*, Vol. 3, No.4, pp. 3-7 (2006)

"Theoretical study of the effect of slow light on BOTDA spatial resolution", Fabien Ravet, Liang Chen, Xiaoyi Bao, Lufan Zou, V.P. Kalosha, *Optics Express*, Vol. 14, No. 22, pp.10351-10358 (2006).

"Detection of buckling in steel pipeline and beam by the distributed Brillouin sensor", Fabien Ravet, Lufan Zou, Xiaoyi Bao, Liang Chen, Rong Feng Huang, Heng Aik Khoo, *Optical Fiber Technology*, Vol. 12, No. 4, pp.305-311 (2006).

"Effect of Brillouin slow light on distributed Brillouin fiber sensors", Lufan Zou, Xiaoyi Bao, Shiquan Yang, Liang Chen, Fabien Ravet, *Optics Letters*, Vol. 31, No. 18, pp. 2698-2700 (2006)

"Distributed Brillouin fiber sensor for detecting pipeline buckling in an energy pipe under internal pressure", Lufan Zou, Xiaoyi Bao, Fabien Ravet, Liang Chen, *Applied Optics*, Vol. 45, No. 14, 3723375 (2006).

"Signature of structure failure using asymmetric and broadening factors of Brillouin Spectrum", Fabien Ravet, Xiaoyi Bao, Togay Ozbakaloglu, Murat Saatcioglu, *IEEE Photonics Technology Letters*, Vol.18, No.2, pp.394-396 (2006).

"Pipeline buckling detection by the distributed Brillouin sensor", Fabien Ravet, Lufan Zou, Xiaoyi Bao, Liang Chen, Rong Feng Huang, Heng Aik Khoo, in *Sensing Issues in Civil Structural Health Monitoring*, Farhad Ansari Editor, Springer Verlag, pp.515-523 (2005)

"A simple method to identify the spatial location better than pulse length with high strain accuracy", Qinrong Yu, Xiaoyi Bao, Fabien Ravet, Liang Chen, *Optics Letters*, Vol. 30, No. 17, pp. 2215-2217 (2005).

"A Simple Approach to Determine Minimum Measurable Stress Length and Stress Measurement Accuracy in Distributed Brillouin Sensing", Fabien Ravet, Xiaoyi Bao, Liang Chen, *Applied Optics*, 44, No.25, pp.5304-5310 (2005).

"Criterion for Sub-Pulse-Length Resolution and Minimum Frequency Shift in Distributed Brillouin Sensors", Fabien Ravet, Xiaoyi Bao, Qinrong Yu, Liang Chen, *IEEE Photonics Technology Letters*, Vol. 17, No.7, pp.1504-1506 (2005).

IX.D.2. Publication List - Conferences

"Identification of Damage on Optical Ground Wire Cable Using Distributed Brillouin Fiber Sensor", Lufan Zou, Xiaoyi Bao, Fabien Ravet, and Liang Chen, *18th International Conference on Optical Fibre Sensors OFS 2006*, Cancun (Mexico), October 23-27, 2006, Technical Digest of the Optical Society of America, Paper ThE88

"A Simple Model For BOTDA Spectral Deconvolution Under Short Spatial Resolution (<50cm) And Non-uniform Strain Conditions", Fabien Ravet, Xiaoyi Bao, Qinrong Yu, Lufan Zou, Liang Chen, *18th International Conference on Optical Fibre Sensors OFS 2006*, Cancun (Mexico), October 23-27, 2006, Technical Digest of the Optical Society of America, Paper ThE41

"BOTDA Location Accuracy In Depleted Pump Regime In The Presence of Brillouin Slow Light", Fabien Ravet, Liang Chen, Xiaoyi Bao, Lufan Zou, *18th International Conference on Optical Fibre Sensors OFS 2006*, Cancun (Mexico), October 23-27, 2006, Technical Digest of the Optical Society of America, Paper ThE39

"Influence of Brillouin Slow Light on Distributed Brillouin Fiber Sensor due to Depletion of Pump Beam", Lufan Zou, Xiaoyi Bao, Shiquan Yang, Liang Chen, and Fabien Ravet, *18th International Conference on Optical Fibre Sensors OFS 2006*, Cancun (Mexico), October 23-27, 2006, Technical Digest of the Optical Society of America, Paper ThC6

"Application of the Distributed Brillouin Sensor to Structural Health Monitoring", Xiaoyi Bao, Fabien Ravet, Lufan Zou, presented as an invited paper at the *Optical Fiber Communication/National Fiber optic Engineering Conference 2006*, paper OTuL7, Anaheim, California, March 5-10, 2006.

"Accurate strain detection and localisation with the Distributed Brillouin Sensor based on a phenomenological signal processing approach", Fabien Ravet, Xiaoyi Bao, Lufan Zou, Qinrong, Yu, Yun Li, Vladimir Kalosha, Liang Chen, presented at the *SPIE Symposium on Smart Structures & Materials/NDE 2006*, San Diego, California, February 27-March 2, 2006, , Proceedings of SPIE vol.61761c1-8.

"A simple method to identify the spatial location complication due to the transient phonon relaxation on the Brillouin loss specrum", Xiaoyi Bao, Qinrong Yu, Fabien Ravet, Liang Chen, presented as an invited paper at the *SPIE Symposium on Smart Structures & Materials/NDE 2006*, San Diego, California, February 27-March 2, 2006, Proceedings of SPIE vol.6167151-8.

"Nonlinear strain response of the concrete column to detect the de-bonding and cracks using distributed Brillouin sensor", Xiaoyi Bao, Fabien Ravet, Lufan Zou, to be presented as an invited paper at the *2nd Interntional Conference on Structural Health Monitoring of Intelligent Infrastructure*, Shenzhen (China), November, 16-18, 2005.

"Prediction of pipeline buckling using distributed fiber Brillouin strain sensor", Lufan Zou, Xiaoyi Bao, Fabien Ravet, Joe Zhou, Tom Zimmerman, to be presented at the *2nd Interntional Conference on Structural Health Monitoring of Intelligent Infrastructure*, Shenzhen (China), November, 16-18, 2005.

"Investigation of Brillouin effects in carbon coating single-mode fiber using for inspection of pipeline buckling", Lufan Zou, Xiaoyi Bao, Fabien Ravet, Yun Li, Liang Chen, M. Du, D. J. DiGiovanni, *Optics East 2005*, Boston, Proceedings of SPIE 6004.

"Criterion for Sub-Pulse-Length Resolution and Minimum Frequency Shift in Distributed Brillouin Sensors", Fabien Ravet, Xiaoyi Bao, Liang Chen, *17th International Conference on Optical Fibre Sensors OFS 2005*, Bruges (Belgium), May 23-27, 2005, Proceedings of SPIE 5855, pp.527-530, 2005.

"Column Structure Deformation Monitoring with the Distributed Brillouin Sensors", Fabien Ravet, Xiaoyi Bao, Togay Ozbakkaloglu, Muslim Majeed, Murat Saatcioglu, Graham Ferrier, Lufan Zou, Liang Chen, *17th International Conference on Optical Fibre Sensors OFS 2005*, Bruges (Belgium), May 23-27, 2005, Proceedings of SPIE 5855, pp.531-534, 2005.

"Distributed fiber Brillouin Strain and temperature sensor with centimetre spatial resolution by coherent probe-pump technique", Lufan Zou, Xiaoyi Bao, Fabien Ravet, Liang Chen, Joe Zhou, Tom E. Zimmerman, *17th International Conference on Optical Fibre Sensors OFS 2005*, Bruges (Belgium), May 23-27, 2005, Proceedings of SPIE 5855, pp.68-53, 2005.

"Distributed fiber strain sensor based on Brillouin scattering for inspection of pipeline buckling", Lufan Zou, Xiaoyi Bao, Yidun Wan, Fabien Ravet, Liang Chen, *17th International Conference on Optical Fibre Sensors OFS 2005*, Bruges (Belgium), May 23-27, 2005, Proceedings of SPIE 5855, pp.571-574, 2005.

"Distributed strain and temperature sensors and their application in structural health monitoring with cm spatial resolution", Xiaoyi Bao, Lufan Zou., Qinrong Yu, Graham Ferrier, Fabien Ravet, Liang Chen, *International Symposium on Advances and Trends in Fiber Optics and Applications*, invited talk, Proceedings pp. 157-166, 2004.

"Pipeline buckling detection by the distributed Brillouin sensor", Xiaoyi Bao., Fabien Ravet, Lufan Zou, Liang Chen, Rong Feng Huang, Heng Aik Khoo, *North American Euro Pacific Workshop for Sensing Issues in Civil Structural Health Monitoring*, Hawaii, USA, Invited Talk, November 11-13, 2004

"In-line inspection of pipeline buckling by distributed Brillouin scattering sensor", Lufan Zou, Fabien Ravet, Xiaoyi Bao, Liang Chen, *Structural Health Monitoring ISIS Workshop*, Winnipeg, Proceedings pp. 183-192, September 2004.

"Effect of pulsewidth on strain measurement accuracy in Brillouin scattering based fibre optic sensors", Fabien Ravet, Xiaoyi Bao, Liang Chen, *Photonics North 2004*, Ottawa, September 27-30, 2004, Proceedings of SPIE vol.5579, pp.187-194.

"Demonstration of the detection of buckling effects in steel pipelines and beams by the Brillouin sensor", Fabien Ravet, Lufan Zou, Xiaoyi Bao, Liang Chen, *Photonics North 2004*, Ottawa, September 27-30, 2004, Proceedings of SPIE vol.5579, pp.58-65.

"Centimeter spatial resolution of distributed optical fiber sensor for structural health monitoring", Lufan Zou, Xiaoyi Bao, Yidun Wan, Fabien Ravet, Liang Chen, *Photonics North 2004*, Ottawa, September 27-30, 2004, Proceedings of SPIE vol.5579, pp.1-10.

"High precise distributed Brillouin scattering sensor for structural health monitoring of optical ground wire cable"; Lufan Zou, Fabien Ravet, Xaoyi Bao and Liang Chen, *Smart Structures and Materials 2004*, San Diego, California, March 14-18, 2004, Proceedings of SPIE Vol.5391 pp.293-300.